

This item was submitted to [Loughborough's Research Repository](#) by the author.
Items in Figshare are protected by copyright, with all rights reserved, unless otherwise indicated.

Synthesis and characterisation of nickel-bearing hydrous silicates

PLEASE CITE THE PUBLISHED VERSION

PUBLISHER

© Joseph Jackson

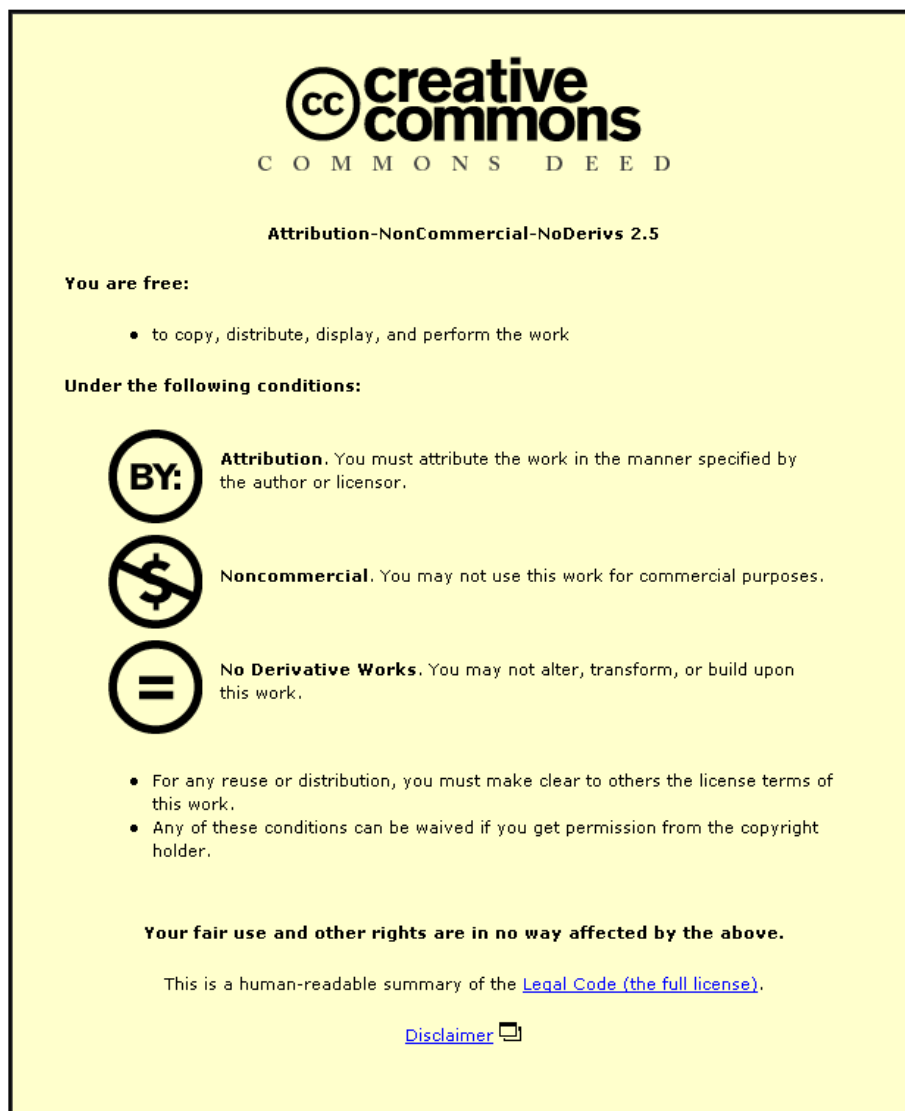
LICENCE

CC BY-NC-ND 4.0

REPOSITORY RECORD

Jackson, Joseph. 2019. "Synthesis and Characterisation of Nickel-bearing Hydrous Silicates". figshare.
<https://hdl.handle.net/2134/15412>.

This item was submitted to Loughborough University as an MPhil thesis by the author and is made available in the Institutional Repository (<https://dspace.lboro.ac.uk/>) under the following Creative Commons Licence conditions.



For the full text of this licence, please go to:
<http://creativecommons.org/licenses/by-nc-nd/2.5/>

Synthesis and Characterisation of Nickel-Bearing Hydrous Silicates

By

Joseph Jackson

**Thesis submitted in partial fulfilment of the
requirements for the award of
Master of Philosophy of Loughborough University**

2014

© by Joseph Jackson (2014)

Abstract

This study of nickel-bearing hydrous silicates has been funded by European Nickel Plc. and Loughborough University, with support from the Natural History Museum, London.

European Nickel Plc., the industrial sponsors of the project, is a nickel mining company based in the UK with mine sites around the globe including Turkey, Albania and the Philippines.

European Nickel developed a process of nickel extraction for lateritic ore deposits known as “atmospheric heap-leach” (AHL). This new technique is not only economically favourable to more traditional nickel extraction methods, with relatively low plant and process costs, but it is also more environmentally responsible with lower CO₂ emissions. These factors make AHL an attractive choice for new nickel extraction ventures. However, speed, efficiency and percentage recovery of nickel have proven to be variable across mined ore bodies using this technique. This is largely due to the fact that lateritic ores, particularly nickel-bearing hydrous silicate ores, are poorly understood. To develop the extraction process and understand the variability inherent to the AHL process thus requires a greater understanding of the ore types, more specifically of their chemistry.

This project has been undertaken to develop the understanding of these materials and has done so by focusing on two main themes.

The first focus was on the characterisation of a suite of natural mineral samples, to broaden the understanding of the types of phases present in lateritic material. Samples were sourced from nickel-laterite mine sites across the globe and historical collections at the Natural History Museum, London.

Characterisation of the materials was initiated with powder x-ray diffraction (PXRD) studies, using both standard laboratory and synchrotron-based instruments. PXRD studies allowed a database of mineral phases to be compiled and common groups and themes to be identified. This found that serpentine ($\text{Mg}_3\text{Si}_2\text{O}_5(\text{OH})_4$), talc ($\text{Mg}_3\text{Si}_4\text{O}_{10}(\text{OH})_2$) and quartz (SiO_2) were the most significant phases in these types of material. Following the PXRD studies, a selection of specimens samples were then investigated further using electron probe micro-analysis (EPMA). EPMA data allowed compositional information to be incorporated in

context. This complementary information further emphasised the importance of talc and serpentine phases to the study, with nickel substitution most common and at the highest levels in these phases. Nickel-bearing talc was observed with up to 39.89wt.% NiO (implying over 70% octahedral cation substitution) and nickel-bearing serpentine was observed with up to 48.67wt.% NiO (implying over 85% octahedral cation substitution). As well as this, EPMA elemental mapping also found evidence of Mg-Ni substitution within mineral phases on a fine scale, observed as an, in-situ, solid solution.

The second focus of this project was a parallel program of synthesis of mineral phases, which was used to allow relevant phases to be studied in isolation, away from the complex matrices inherent within the natural materials. Synthesis of the relevant mineral phases also allowed elemental compositions to be controlled, and allowed systematic studies of these materials in greater detail. This also allowed the synthetic materials to be used as standards for comparison to their natural analogues. The program of synthesis used various synthetic methods to produce the materials of interest. These included high temperature methods, low temperature hydrothermal methods and high temperature and pressure methods using specialist equipment.

Early synthesis of hydrous materials was performed using Teflon-lined autoclave type apparatus but the achievable temperatures and pressures were too low to synthesise products that were crystalline enough for detailed characterisation.

Synthesis using these low temperature and pressure methods found poor crystallinity of the products to be a problem for detailed characterisation. This led to the use of specialist high-temperature and pressure, Tuttle-type, cold-seal apparatus, which was able to achieve harsher reaction conditions, enabling the synthesis of single phase ordered hydrous mineral phases which permitted more detailed characterisation.

Synthetic methods were gathered from the literature and adapted and optimised for the synthesis of materials of interest to the project. The most significant development in the synthetic materials project was the synthesis of a full Mg-Ni talc series $((\text{Mg,Ni})_3\text{Si}_4\text{O}_{10}(\text{OH})_2)$. The full series was then characterised using PXRD, infrared spectroscopy, Raman spectroscopy and thermal analysis. PXRD allowed confirmation of the synthetic products as well as structural refinements to be performed. The refined unit cell parameters match closely with reported unit cell parameters and indicate there are no miscibility gaps in the series. The similarities in the cation sizes of Ni^{2+} and Mg^{2+} produce

only subtle changes in the lattice parameters between the end members and no systematic trends are observed. Infrared spectroscopy has not only showed agreement with previously published literature on the series, but also offered a more systematic approach to the compositional series and increased the amount of data on the materials. Raman spectroscopy, which has not been previously reported on these materials, has also been used to show the same shifts in the OH-stretching region as observed in the infrared studies. Thermal analysis, shows increasing thermal stability of Ni-substituted talc, increasing by c. 60°C from the Mg to Ni end-member.

Carrying out these two programs of work in parallel meant characterisation of the natural materials helped to focus the direction of the synthesis program, whilst information from the synthetic studies was fed back to improve the understanding of the natural materials. This synergistic approach allowed greater benefits to be gained from each side as the project progressed and, combining the two focuses of the project, it was then possible to compare aspects of the synthetic materials with the natural materials and increase the understanding of the links between them. This has been exhibited here specifically by comparison of infrared spectra of the natural nickel-bearing talc specimens to the spectra of the synthetic talc series, which has allowed nickel substitution in the natural materials to be identified by this technique.

Acknowledgements

Firstly I would like to thank European Nickel and Loughborough University for funding this research project and the Natural History Museum, London, for their support and use of their facilities.

Special thanks must go to my supervisors Caroline Kirk, Sandie Dann and Richard Herrington for their continued patience, support and guidance throughout the course of this project. I would also like to thank all the other academic and technical staff that helped along the way, both at the University and at the Museum.

Next of course I need to thank all the friends that have been there along the journey. There are too many to list but every one of you helped in some way. Just know that I'm forever grateful for all the entertainment and laughter that kept me going and (pretty much) sane. Cheers to you all!

Then to the people I owe the most, my family, most of all my Mum and Dad. I could never thank you enough for all the love and support you have given me. You have backed me at every turn, with more belief in me than I ever had in myself, and you have always been there whenever I have needed you. So this is a thank you, not just for all you have done for me over this degree but for everything you have done that got me here.

Last, but by no means least, Kerry, you have been wonderful. Without your love, patience, support and encouragement (even when I called it "nagging") I would never have gotten here. At times I'm not sure how you put up with me, but I'm so glad you did! It might have felt like an age getting here but now we have an eternity to look back on it together. I wouldn't have done this without you and I love you with all my heart.

Index

1. Introduction	1
1.1. Nickel.	1
1.2. Use of Nickel.	1
1.3. Nickel Occurrence	3
1.3.1. Sulphide Ores	3
1.3.2. Laterite Ores	3
1.4. Nickel Production	4
1.5. Nickel Extraction Processes	5
1.6. Saprolite Ores	6
1.7. Phyllosilicates	9
1.8. Lateritic Nickel Ore Hydrous Silicate Minerals	11
1.8.1. Garnierite	13
1.9. Serpentine and Talc group minerals	14
1.9.1 Serpentine Group	14
1.9.1.1 Lizardite	15
1.9.1.2 Chrysotile	16
1.9.1.3 Antigorite	16
1.9.1.4 Ni-bearing serpentines	17
1.9.1.4.1 Nepouite	17
1.9.1.4.2 Pecoraite	17
1.9.2. Talc Group	19

1.9.2.1 Talc	20
1.9.2.2 Willemseite	21
1.9.2.3 Synthetic talc/willemseite	21
1.10 Distribution of Ni ²⁺	24
2. Experimental Methods	25
2.1. Solid-state Synthesis Introduction	25
2.2. High-temperature methods	25
2.2.1. The basic ceramic method	26
2.2.2. Controlled Atmosphere Method	27
2.2.3. Sealed Tube Method	27
2.3. Hydrothermal Methods	28
2.3.1. Parr [®] PTFE Lined Hydrothermal Bombs	29
2.3.2. Tuttle Apparatus	29
3. Characterisation Techniques	34
3.1. Powder X-ray Diffraction (PXRD)	34
3.1.1. Theory of PXRD	34
3.1.2. X-ray generation	35
3.1.3. XRD Instrumentation	37
3.1.4. Synchrotron Source PXRD	38
3.1.5. Application of PXRD to Saprolitic Minerals	39
3.1.6. X-ray Diffraction Experiments	40
3.2. Electron Probe Microanalysis (EPMA)	42
3.2.1. Secondary Electrons	43

3.2.2. Back-scattered Electrons	44
3.2.3. Characteristic X-rays	44
3.2.4. Application of EPMA to Saprolitic Minerals	46
3.2.5. EPMA Experiments	47
3.3. Vibrational Spectroscopy	51
3.3.1. Infrared (IR) Spectroscopy	51
3.3.2. Raman Spectroscopy	52
3.3.3. Application of Vibrational Spectroscopy to Saprolitic Minerals	52
3.3.4. IR Experiments	53
3.3.5. Raman Experiments	54
3.4. Thermal Analysis	54
3.4.1. Application of Thermal Analysis to Saprolitic Minerals	55
3.4.2. Thermal Analysis Experiments	55
4. Characterisation of Natural Materials	56
4.1 PXRD Studies	56
4.1.1 Samples from Turkey	61
4.1.2. Samples from Cerro Matoso (Columbia)	62
4.1.3. Serpentine	63
4.1.4. Talcs	64
4.1.5. Chlorites	66
4.1.6. Smectites	67
4.1.7. PXRD Conclusions	68
4.2. Synchrotron based High-Resolution PXRD	69

4.3. EPMA Studies	70
4.3.1. M14707 (worked example)	70
4.3.2. CMO48B.97	84
4.3.3. CM053.97	86
4.3.4. OR.467	89
4.3.5. B105.9.0	93
4.3.6. B122.21.2	99
4.3.7. 09NIC050501	101
4.3.8. Pimelite Bohemia.860	104
4.3.9. Conclusions from EPMA of Natural Materials	107
5. Synthesis of Relevant Minerals	109
5.1. Hydrous Silicate Synthesis	109
5.2. Low T and P hydrothermal synthesis	109
5.2.1 Ni 1:1 Phyllosilicate	111
5.2.2. Ni and Mg 1:1 and 2:1 Phyllosilicates	112
5.2.3. Ni-Saponite	113
5.2.4. Interstratified Lizardite/Saponite	115
5.3. High T and P hydrothermal synthesis	117
5.3.1. Ni-Mg talc $((\text{Ni,Mg})_3\text{Si}_4\text{O}_{10}(\text{OH})_2)$	120
5.3.2. Ni-serpentine $(\text{Ni}_3\text{Si}_2\text{O}_5(\text{OH})_4)$	134
5.4. Non-Hydrous Silicate Synthesis	136
5.4.1. Ni/Mg Olivines	138
5.4.2. Fayalite $(\text{Fe}_2\text{SiO}_4)$	140

5.5. Synthetic Materials Conclusions	142
6. Synthetic vs. Natural Talc Materials	144
6.1. OR467	144
6.2. CM053	147
6.3. Lipovka	148
6.4. 09NIC060503A	150
6.5. Conclusions	152
7. Appendices	153
8. References	157

1. Introduction

1.1. Nickel

The element nickel (Ni), atomic number 28, is a lustrous, Ferro-magnetic, silvery-white metal belonging to the transition metal group. It was used as an alloying metal in China as early as 200 BC, almost 2000 years before it was isolated and recognised as a new element in 1751 by Axel Fredrik Cronstedt¹. Its name originates from the Saxony “Kupfernickenl” (meaning “Old Nick’s copper”) that was given to the reddish-coloured ore, NiAs, which resembled Cu₂O but when processed yielded only a useless slag material and no copper, which they believed to be the work of the devil (Old Nick)¹.

The trend in production and demand for nickel has followed world events and economic cycles, since 1950 nickel production has risen at an average rate of around 4% p.a. (Fig. 1).

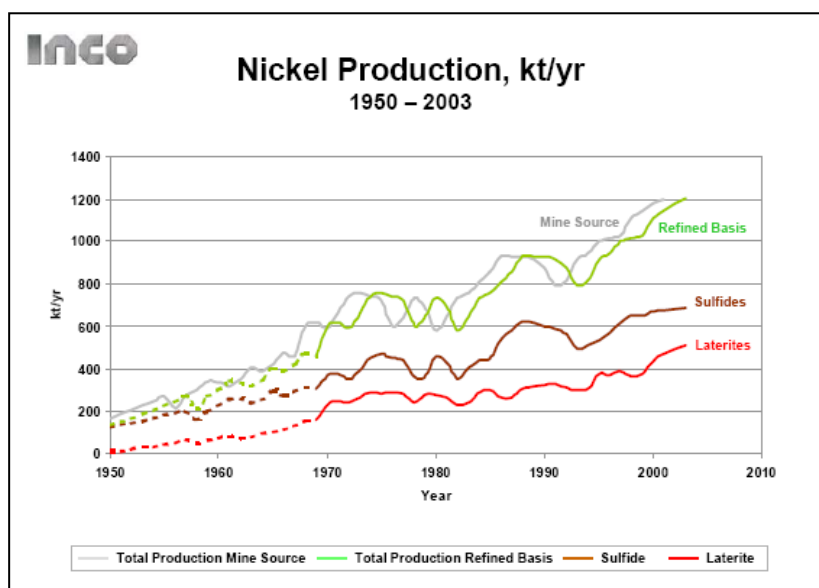


Figure 1: Graph of Nickel production History².

1.2. Use of Nickel

Nickel has become a valuable commodity owing to its wide commercial and industrial applications. Nickel is used in plating, catalysts, coins, magnets, batteries, and jewellery as well as in a variety of other applications. The main commercial nickel chemicals are the

carbonate (NiCO_3), divalent oxide (NiO), sulphate (NiSO_4) and chloride (NiCl_2). The greatest use of nickel is in alloys; about 65% of nickel is used in the manufacture of austenitic stainless steels³ and another 20% in other steel and non-ferrous alloys (e.g. cupronickel) and super alloys (e.g. Inconel 600), often for highly specialized purposes (e.g. in aeronautical gas turbines)⁴. All of these applications owe their use to the specific chemical and physical properties imbibed by nickel. Nickel metal crystallises with a face centred cubic unit cell and has a high melting point of 1453°C , high resistance to corrosion and oxidation, high strength and toughness at elevated temperatures, and is capable of being magnetized. For example, in its major application in austenitic stainless steel alloys, nickel is responsible for many improvements to the properties of stainless steel. The addition of nickel to ferritic stainless steel (that is an alloy of carbon steel with $>10.5\%$ Cr), in the correct ratio (for example grade 304 which contains Cr 18-20% and Ni 8-10.5%), changes the unit cell of the alloy from body centred cubic (bcc, ferrite) to face centred cubic (fcc, austenite) (see Fig. 2). This alteration of the (lattice) structure in austenitic stainless steel improves its formability and toughness (particularly at low temperatures). Nickel also improves the corrosion resistance (reducing the rate of corrosion propagation and increasing resistance to reducing environments) and high temperature properties of the alloy.

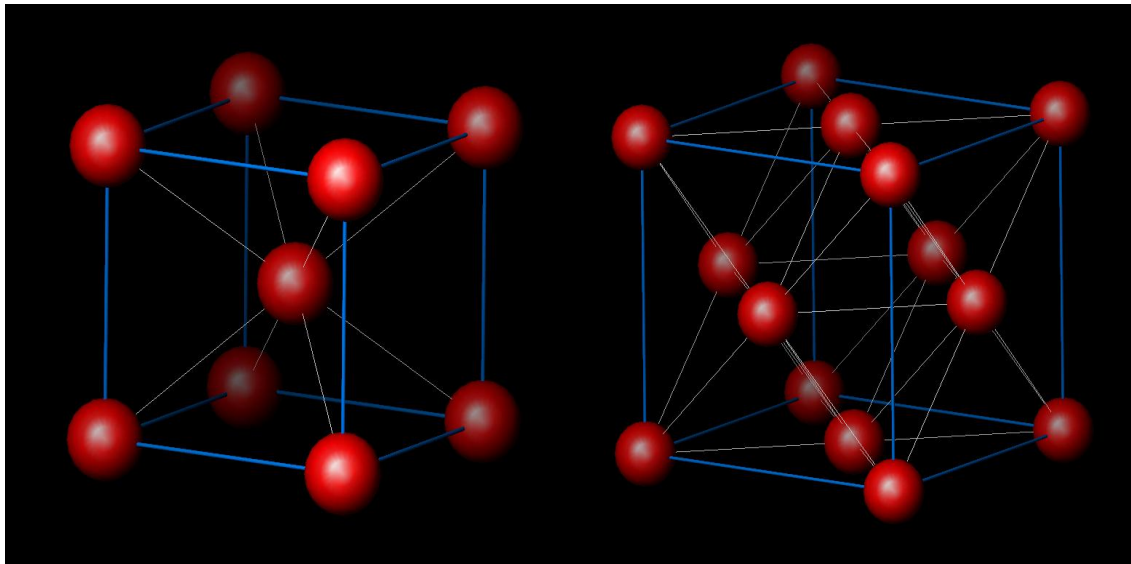


Figure 2: Ferrite BCC (left) and Austenite FCC (right) crystal structures.

1.3. Nickel Occurrence

Nickel is the 5th most abundant element in the earth but the average content of Ni in the Earth's crust is just 72ppm⁵. Nickel is not distributed uniformly through the crust though and can be found in ore deposits at much higher concentrations. There are two principle types of nickel ore deposit; sulphide ores and laterite ores.

1.3.1. Sulphide Ores

Nickel sulphide ore deposits predominantly consist of pentlandite ((Fe, Ni)₉S₈) which typically has a Ni:Fe ratio close to 1:1. Sulphur based nickel ores normally develop by a magmatic concentration process; as sulphur-rich magma cools, an immiscible sulphide liquid phase forms with the silicate liquid and, since nickel is a chalcophile, the heavier sulphide phase sinks to the bottom of the magma chamber and the nickel is concentrated in the sulphide crystals as it cools.

1.3.2. Laterite Ores

Laterite ore deposits form in hot, wet, tropical areas where the weathering of parent rock (commonly peridotite type; high in olivine, (Mg,Fe)₂SiO₄), is caused by percolating rain and ground water^{5,6}. Dissolution of the parent rock causes the leaching of elements through the rock profile, with rates and extents of laterization dependent on the historical environment and conditions⁷. Increased nickel concentration in laterite deposits is caused by substitution of Ni for other elements such as Mg, Al and Fe as they are leached at different rates through the rock profile^{5,6}.

Lateritic ore deposits can be divided into two main zones or types dependent on their dominant ore bodies, these are; limonite (or oxide) and saprolite (or silicate). Limonite type deposits are virtually free of silicate minerals because silica is rapidly leached down through the rock profile leaving a concentration of aluminium and iron rich oxide minerals such as goethite, FeO(OH). Conversely, saprolite type deposits are dominated by Mg/Al-rich silicates such as the serpentine group minerals (Mg,Al,Fe,Mn,Ni,Zn)₂₋₃(Si,Al,Fe)₂O₅(OH)₄. Nickel content is generally higher in the silicate ores than the oxide ores.

In an ideal lateritic profile (Fig. 3) the saprolite zone can be roughly divided into 4 zones or layers descending through the rock profile; the upper saprolite, the lower saprolite, saprock and the unaltered parent rock: The upper saprolite zone is typified by a high concentration of clay type minerals, such as those from the smectite group, $(\text{Na,Ca})_{0.3}(\text{Al,Mg,Fe})_2(\text{Si,Al})_4\text{O}_{10}(\text{OH})_2.n\text{H}_2\text{O}$ and no remaining parent rock. The lower saprolite is distinguished by a lesser degree of oxidation. This is where the “oxidation front” (between chemically oxidised minerals and chemicals above, and, chemically reduced minerals and chemicals existing below) lies. The saprock zone is only altered from the parent rock in failure systems such as faults. Often a lateritic profile will only display certain geological and mineralogical aspects of this idealised profile depending on its historical formation. The upper saprolite, lower saprolite and saprock regions are frequently referred to as a whole simply as saprolite because it is often difficult to discriminate between them.

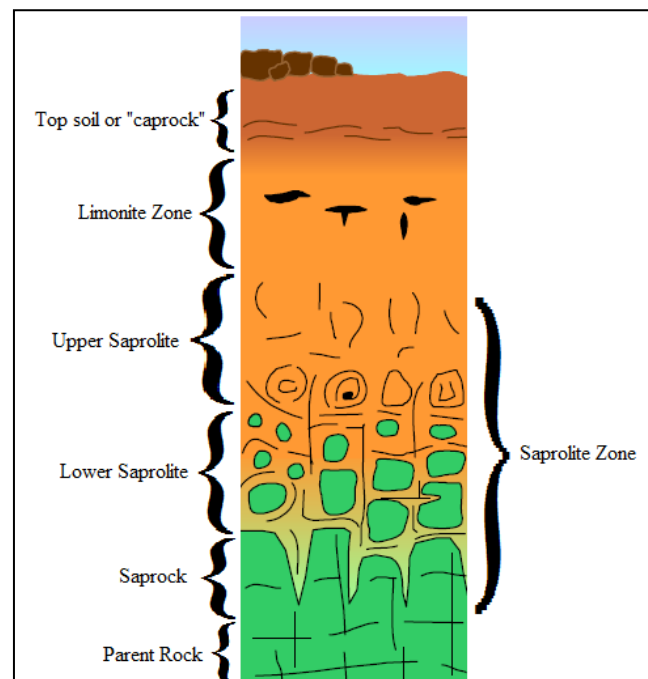


Figure 3: Schematic diagram of a nickeliferous laterite profile.

1.4. Nickel Production

Identified land-based resources averaging 1% nickel or greater contain at least 130 million tons of nickel, over two thirds of this is in laterite ores and the remainder in sulphide ores⁸. Despite this, laterites currently account for less than half of global nickel production⁸.

However, it is predicted that the continual global growth of demand for nickel is expected to see the future production of nickel from sulphide ores remaining more or less constant⁹. This is due to the depletion of known sulphide deposits and an abundance of known, unexploited laterite resources¹⁰. This will result in increasing the share of nickel that will need to be sourced from laterite deposits. As a result, the economics of laterite projects will have a significant impact on the future of nickel prices^{9,10}. The key factors to the economics of a laterite project are the ore grade and the choice of extraction process.

1.5. Nickel Extraction Processes

Both pyrometallurgical and hydrometallurgical types of extraction processes are used for extraction of nickel from laterite ores (Fig. 4). The process choice depends on the ore mineral type and grade as well as the capital and economic plan of the project.

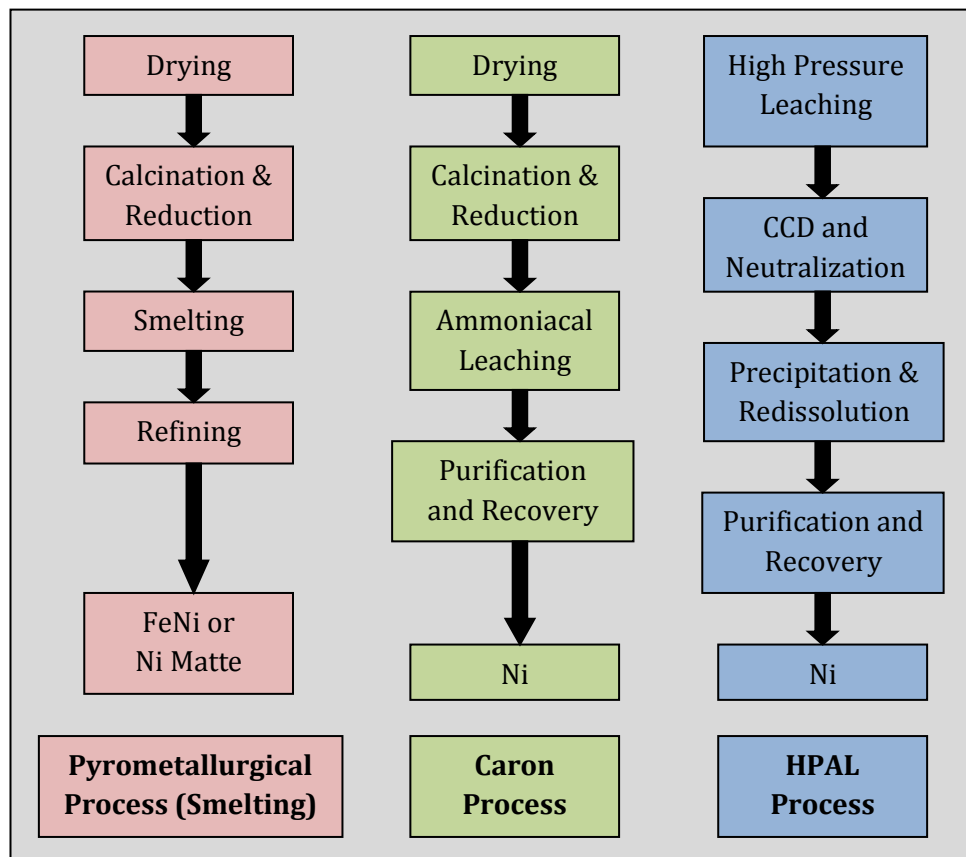


Figure 4: Generalised flow diagrams of lateritic nickel extraction processes.

*CCD - counter current decantation.

All of these traditional processes are energy intensive and require expensive specialist equipment^{7,10}. Pyrometallurgical processing, commonly called smelting, is very energy intensive so is predominantly applied to saprolite ore as it is generally richer in Ni¹¹. Conversely, hydrometallurgical processes such as the Caron process and HPAL (high pressure acid leaching) are more applicable to the limonite type ores, because the high magnesium content in saprolite ore results in higher acid consumption^{12,13}.

An understanding of these limitations has pushed forward the development of newer methods to improve where the previously mentioned processes fall down^{14,15,16}. As well as these economic drivers there has also been an increased effort for greener, more responsible, processes with lower CO₂ emissions, strongly encouraged by current international politics.

An example of these newer processes is the atmospheric heap leach (AHL)⁷ method, currently in use by European Nickel Plc. AHL is primarily applicable to clay-poor oxide-rich ore types, where clay contents are low enough to allow percolation of acid through the heap. This process and its plant are relatively cheap (up to 25% of the cost of an HPAL plant), due to the lack of requirement to heat and pressurise the ore and acid, which also has the added benefit of lower CO₂ emissions. Sulphuric acid for the process is generated on-site, in an acid plant, which releases energy (as steam) that can be used to generate electricity in excess of that required by the project which can be sold to the local grid. However, for the moment at least, AHL is currently limited in the types of ore that can be processed.

1.6. Saprolite Ores

Saprolite ores are dominated by silicate minerals which have varied composition and stability. Silicate minerals comprise around 90% of the Earth's crust and account for approximately ¼ of all known minerals. As of May 2007 more than 1,243 natural silicates had been approved by the International Mineralogical Association (IMA)¹⁷. The major structural unit of almost all silicate minerals is the tetrahedral (SiO₄)⁴⁻ anion (Fig. 5).

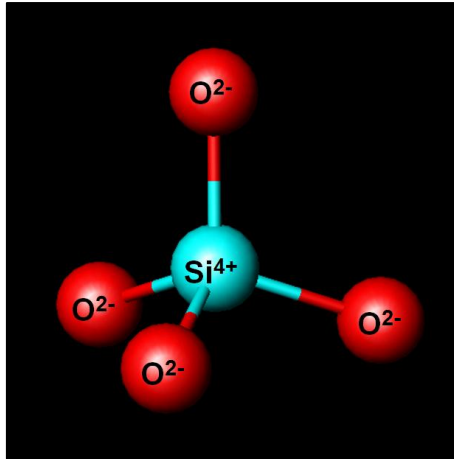


Figure 5: $(\text{SiO}_4)^{4-}$ anion.

The Si-O bond is approximately 50% covalent and 50% ionic, that is, although the bond arises in part from the attraction of oppositely charged ions, it also involves sharing of the electrons and inter-penetration of the electronic structure. The total bonding energy of each Si^{4+} ion is distributed equally among four O^{2-} ions; hence, the strength of any Si-O bond is equal to half the total bonding energy in the O^{2-} ion. Therefore, each O^{2-} has the potential of bonding to another Si^{4+} ion and entering into another tetrahedral grouping and so on, leading to sharing or bridging O^{2-} ions; polymerization. There is never more than one O^{2-} shared between two silica tetrahedra. The degree to which this polymerization occurs can be used to divide silicates into 6 types; nesosilicates, sorosilicates, cyclosilicates, inosilicates, phyllosilicates and tectosilicates (Fig. 6).

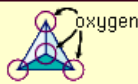
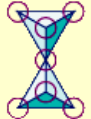
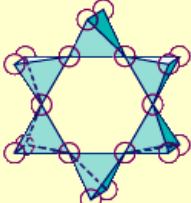
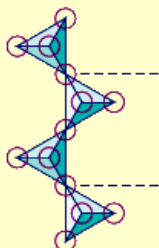
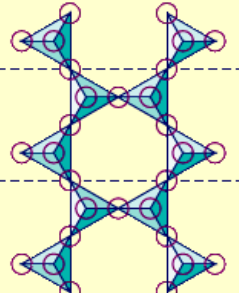
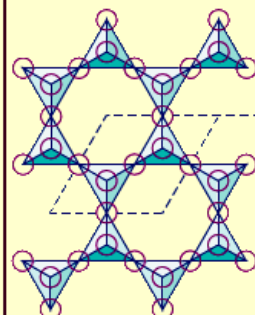
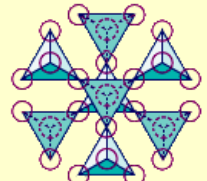
class	arrangement of SiO ₄ tetrahedrons (central Si ⁴⁺ not shown)	unit composition	mineral example
Nesosilicates		(SiO ₄) ⁴⁻	Olivine, (Mg, Fe) ₂ SiO ₄
Sorosilicates		(Si ₂ O ₇) ⁶⁻	Hemimorphite, Zn ₄ Si ₂ O ₇ (OH) ₂ ·H ₂ O
Cyclosilicates		(Si ₆ O ₁₈) ¹²⁻	Beryl, Be ₃ Al ₂ Si ₆ O ₁₈
Inosilicates (single chain)		(Si ₂ O ₆) ⁴⁻	Pyroxene e.g., enstatite, MgSiO ₃
Inosilicates (double chain)		(Si ₄ O ₁₁) ⁶⁻	Amphibole e.g., anthophyllite, Mg ₇ Si ₈ O ₂₂ (OH) ₂
Phyllosilicates		(Si ₂ O ₅) ²⁻	Mica e.g., phlogopite, KMg ₃ (AlSi ₃ O ₁₀)(OH) ₂
Tectosilicates		(SiO ₂) ⁰	High cristobalite, SiO ₂

Figure 6: Polymerisation classes of the silicates.¹⁸

1.7. Phyllosilicates

Phyllosilicates or sheet or layer silicates (as they are also known, the prefix phyllo- coming from the Greek word phylum, meaning leaf), are the predominant silicate class found in lateritic ore deposits as a result of the weathering process¹⁹. In the simplest form phyllosilicates can be described as infinite flat sheets of SiO_4 tetrahedra, in which, each tetrahedral unit is bonded to 3 planar neighbours by sharing an oxygen atom, with a maximum of two silicon atoms bonded to each oxygen atom. This gives the structure an overall Si:O ratio of 2:5.

However, phyllosilicate minerals are much more complex. There are two basic building blocks that make up the mineral structures; the tetrahedral sheet (T) and the octahedral sheet (O)² (Fig. 7).

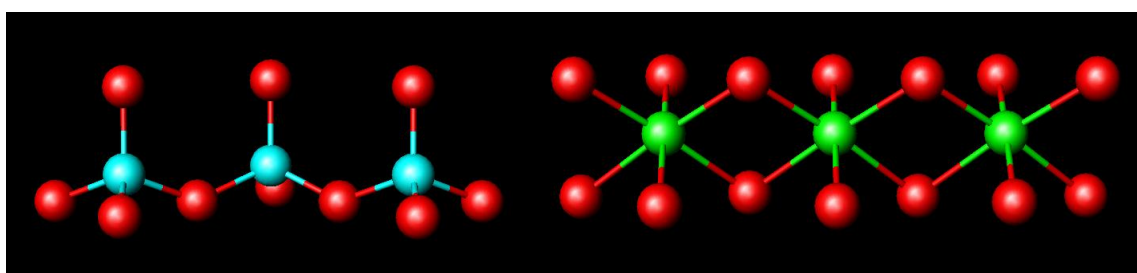


Figure 7: Tetrahedral (left) and Octahedral (right) sheet diagrams

Si (blue), O (red), Mg (green)

Substitution of different ions can occur in either sheet (Table 1). The tetrahedral sheet is predominantly constructed of SiO_4 tetrahedra but can also contain some substituted tetrahedral AlO_4 (the Al^{3+} ion yielding a net negative charge in the layer). The octahedral sheet contains cations in 6-fold (octahedral) coordination to either oxygen atoms or hydroxyl groups. The cations in the octahedral sheet can be of several different elements and are often mixtures of more than one. The valency of the modal cation defines the type of this octahedral layer; if the octahedral layer contains mainly trivalent ions (e.g. Al^{3+}) it is known as dioctahedral (as with a trivalent cation, only 2/3 of the octahedral sites are occupied); conversely, if the layer contains mainly divalent ions (e.g. Mg^{2+}) it is known as trioctahedral (as 3/3 of the octahedral sites are occupied).

Cation	Co-ordination number	Ionic Radius (pm)
Si ⁴⁺	4	41
Al ³⁺	4	54
Al ³⁺	6	54
Fe ³⁺	6	55
Mg ²⁺	6	72
Ni ²⁺	6	69
Fe ²⁺	6	61
Mn ²⁺	6	67
Na ⁺	8	102
K ⁺	8	138
Ca ²⁺	8	100

Table 1: Coordination of common elements in phyllosilicates.

The layering of these sheets can occur in four basic patterns (Fig. 8): Alternating tetrahedral and octahedral sheets in a 1:1 structure (TO), as in lizardite ($\text{Mg}_3\text{Si}_2\text{O}_5(\text{OH})_4$); a sandwich of one octahedral sheet between two tetrahedral sheets in a 2:1 structure (TOT), as in talc ($\text{Mg}_3\text{Si}_4\text{O}_{10}(\text{OH})_2$); incorporating an hydroxide layer (also known as a brucite $\text{Mg}_3(\text{OH})_6$ or gibbsite $\text{Al}_3(\text{OH})_6$ type layer) (H) to give a 2:1:1 type structure (TOTH) as found in clinocllore ($\text{Mg}_6\text{Si}_4\text{O}_{10}(\text{OH})_8$); A final possible structure arrangement can form with the inclusion of a fixed or exchangeable cation interlayer (TOTC) as in montmorillonite ($(\text{Na},\text{Ca})_{0.3}(\text{Al},\text{Mg})_2\text{Si}_4\text{O}_{10}(\text{OH})_2 \cdot n\text{H}_2\text{O}$).

These layering characteristics of phyllosilicates are largely responsible for their common properties; relative softness, platy morphologies, a single pronounced cleavage, low specific gravity and possible flexibility and elasticity of layers²¹.

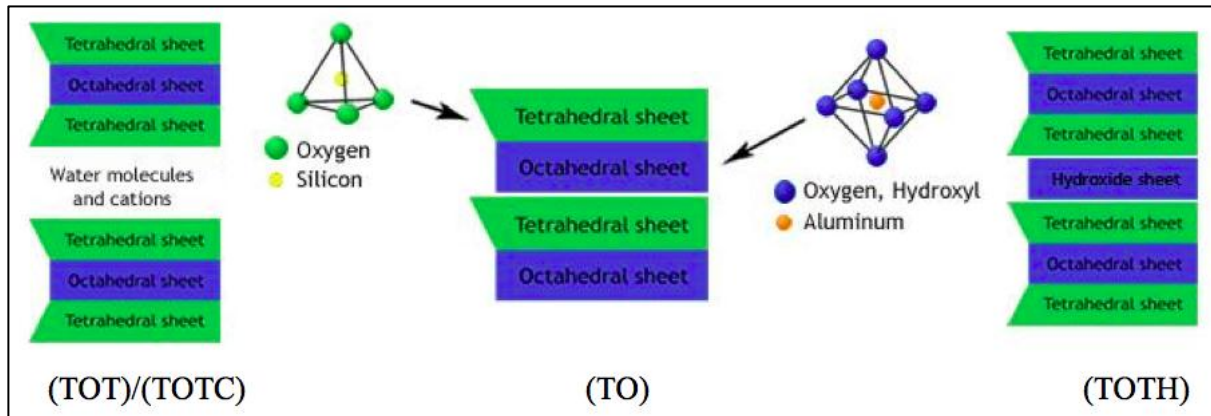


Figure 8: Phyllosilicate structural unit schematic diagrams.

1.8. Lateritic Nickel Ore Hydrated Silicate Minerals

There are many known phyllosilicate minerals, however, the variety of known phyllosilicates of significance in nickel-bearing hydrated silicate ore deposits is relatively limited (Table 2).

Mineral name:	Approved CMNMC formula:	Group:	Notes:
Serpentine (Group)	$(\text{Mg,Al,Fe,Mn,Ni,Zn})_{2-3}(\text{Si,Al,Fe})_2\text{O}_5(\text{OH})_4$		
Lizardite	$\text{Mg}_3\text{Si}_2\text{O}_5(\text{OH})_4$	Serpentine	
Nepouite	$\text{Ni}_3\text{Si}_2\text{O}_5(\text{OH})_4$	Serpentine	Ni analogue of Lizardite
Chrysotile	$\text{Mg}_3\text{Si}_2\text{O}_5(\text{OH})_4$	Serpentine	
Pecoraite	$\text{Ni}_3\text{Si}_2\text{O}_5(\text{OH})_4$	Serpentine	Ni analogue of Chrysotile
Antigorite	$\text{Mg}_3\text{Si}_2\text{O}_5(\text{OH})_4$	Serpentine	
Talc	$\text{Mg}_3\text{Si}_4\text{O}_{10}(\text{OH})_2$	Talc	
Willemseite	$\text{Ni}_3\text{Si}_4\text{O}_{10}(\text{OH})_2$	Talc	Ni analogue of Talc
Amesite	$\text{Mg}_2\text{Al}(\text{Si,Al})\text{O}_5(\text{OH})_4$	<i>Amesite/Serpentine</i>	
Berthierine	$(\text{Fe}^{2+}, \text{Fe}^{3+}, \text{Al})_3(\text{Si,Al})_2\text{O}_5(\text{OH})_4$	<i>Amesite/Serpentine</i>	
Brindleyite	$(\text{Ni,Al})_3(\text{Si,Al})_2\text{O}_5(\text{OH})_4$	<i>Amesite/Serpentine</i>	Ni analogue of Amesite
Chlorite (group)	$(\text{Mg,Al,Fe,Li,Mn,Ni})_{4-6}(\text{Si,Al,B,Fe})_4\text{O}_{10}(\text{OH},\text{O})_8$	Chlorite	
Clinochlore	$\text{Mg}_6\text{Si}_4\text{O}_{10}(\text{OH})_8$	Chlorite	
Nimite	$(\text{Ni,Mg,Al})_6(\text{Si,Al})_4\text{O}_{10}(\text{OH})_8$	Chlorite	Ni-bearing chlorite
Smectite (group)		Smectite	
Beidellite	$(\text{Na,Ca})_{0.3}\text{Al}_2(\text{Si,Al})_4\text{O}_{10}(\text{OH})_2 \cdot n\text{H}_2\text{O}$	Smectite	Diocahedral
Montmorillonite	$(\text{Na,Ca})_{0.3}(\text{Al,Mg})_2\text{Si}_4\text{O}_{10}(\text{OH})_2 \cdot n\text{H}_2\text{O}$	Smectite	Diocahedral
Nontronite	$\text{Na}_{0.3}(\text{Fe}^{3+})_2(\text{Si,Al})_4\text{O}_{10}(\text{OH})_2 \cdot n\text{H}_2\text{O}$	Smectite	Diocahedral
Saponite	$(\text{Ca,Na})_{0.3}(\text{Mg,Fe})_3(\text{Si,Al})_4\text{O}_{10}(\text{OH})_2 \cdot 4\text{H}_2\text{O}$	Smectite	Triocahedral

Table 2: Summary of hydrous silicate minerals of significance in lateritic nickel ore deposits. (Mineral names in **bold** are recognised by IMA/CNMNC^{**} Information in *italics* is less well defined)

^{**}CNMNC: Commission on New Minerals, Nomenclature and Classification. Previously known as the Commission on New Minerals and Mineral Names (CNMMN) was established in 1959 for the purpose of controlling the introduction of new minerals and mineral names, and of rationalising mineral nomenclature.^{18**}

As mentioned previously, nickel enrichment in laterite deposits is caused by substitution of Ni for other elements such as Mg, Al and Fe as they are leached through the rock profile during the weathering process²⁰⁻²². However, little systematic work has been carried out to determine the controls of this nickel substitution. However, this theory has since been discarded²⁴ and it is now accepted that Ni^{2+} substitutes into the octahedral layer only, predominantly in place of Mg^{2+} .

All known Ni-bearing hydrous silicates have an equivalent Mg-hydrous silicate related to them (see Table 2). It has been shown in several studies that these analogous phases form solid solutions, displaying varying degrees of substitution between the Mg and Ni end-members^{25,26}.

1.8.1 Garnierite

“Garnierite” is a term frequently used in mineralogical publications for intimate mixtures of two or more nickel-bearing hydrous silicates²⁷⁻³¹, it does not however include mixtures dominated by smectite type minerals (these are commonly referred to as smectite nickel silicates or, more confusingly, as clay-silicate laterites). Garnierite is not, as the name may suggest, a separate mineral species and is now (with the availability of determinative methods that can discriminate the separate mineral phases) only really appropriate as a field term. As such, this work will try to avoid use of this term where possible.

1.9. Serpentine and Talc group minerals

Much of the work in this thesis focuses on the serpentine and talc group minerals so these are discussed here in greater detail.

1.9.1 Serpentine Group

The common serpentine group minerals are summarised in Table 3.

Mineral name:	Approved CMNMC formula:
Serpentine (Group)	$(\text{Mg,Al,Fe,Mn,Ni,Zn})_{2-3}(\text{Si,Al,Fe})_2\text{O}_5(\text{OH})_4$
Lizardite	$\text{Mg}_3\text{Si}_2\text{O}_5(\text{OH})_4$
Nepouite	$\text{Ni}_3\text{Si}_2\text{O}_5(\text{OH})_4$
Chrysotile	$\text{Mg}_3\text{Si}_2\text{O}_5(\text{OH})_4$
Pecoraite	$\text{Ni}_3\text{Si}_2\text{O}_5(\text{OH})_4$
Antigorite	$\text{Mg}_3\text{Si}_2\text{O}_5(\text{OH})_4$

Table 3: Serpentine group (from Table 2)

The serpentine group^{32,33} are all of a 1:1 layer type similar to that of the kaolinite group³⁴ (of which they are a tri-octahedral analogue). Of the silicates relevant to nickel ores the serpentine group are the best characterised. All the serpentine minerals have the same basic chemical formula $\text{A}_3\text{B}_2\text{O}_5(\text{OH})_4$ (where A is the octahedral cation and B is the tetrahedral cation), the difference between each is in its crystal structure. The “TO” layer structure of the serpentine group comprises a tetrahedral layer of SiO_4^{4-} anions and an octahedral layer of metal hydroxide ions. The repeat distances of the tetrahedral sheet are smaller than that of the octahedral sheet and this mismatch causes departure from the simple structure. The mismatch effect can be reduced in three ways; distortion of the octahedral and/or tetrahedral networks; substitution of different sized ions into the networks (i.e. larger ions into the tetrahedral layer or smaller ions into the octahedral layer); or curvature of the sheet with the octahedral layer on the outside. Curvature of the network gives rise to the three most common types of serpentine: lizardite, chrysotile and antigorite (Fig. 9).

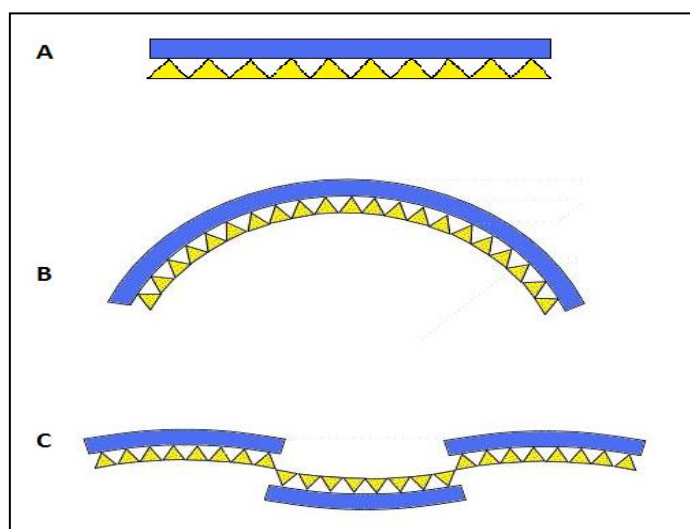


Figure 9: Schematic representation of tetrahedral (yellow) and octahedral (blue) layers in the serpentine mineral structures: A) Lizardite B) Chrysotile C) Antigorite.

1.9.1.1 Lizardite

Lizardite (the name coming from its type locality; the Lizard complex, Cornwall, England)³⁵ shows the least departure from the simple structure of the three main serpentine types (Figs. 9 & 10). It forms hexagonal planar sheets with a perfect basal (001) cleavage and has been shown using electron microscopy^{19,36,36} to exhibit the platy morphology expected from this structure. Lizardite exists as many different polytypes with varying degrees of structural disorder; these include lizardite-1M, -1T, -2H₁, -2H₂ and -6T₁. The ideal lizardite structure is that of lizardite-1M³⁶. Lizardite-1M crystallises in the Cm space group³⁸ with lattice parameters of; $a = 5.3 \text{ \AA}$ $b = 9.2 \text{ \AA}$ $c = 7.3 \text{ \AA}$ $\beta = 120^\circ$. However, due to the number of different polymorphs and the tendency of lizardite to form as fine grains it is often very difficult to discriminate between them using techniques such as XRD^{19,36}.

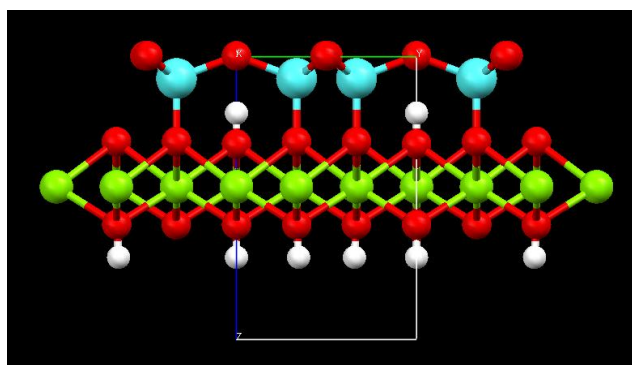


Figure 10: Lizardite crystal structure³⁹

1.9.1.2 Chrysotile

Chrysotile (the name coming from the Greek for golden and fibre) has a very different sheet structure to lizardite; it curves (Figs. 9 & 11) to reduce the layer mismatching and forms hollow cylinders or rolls; resulting in a fibrous cleavage of the crystal. Viewed under an electron microscope chrysotile may be identified by its asbestiform fibres. Like lizardite, chrysotile occurs as several polymorphs; clino-, para- and orthochrysotile. Clinochrysotile is the most common form of chrysotile and it crystallises in the C2/m space group with the cell parameters; $a=5.34 \text{ \AA}$, $b=9.25 \text{ \AA}$, $c=14.65 \text{ \AA}$, $\beta=93^\circ$.

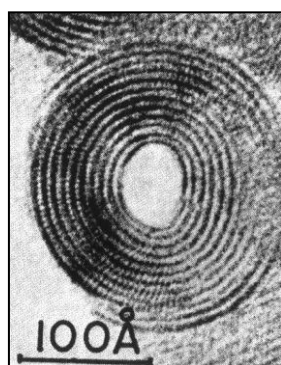


Figure 11: TEM image of end-on chrysotile fibril from Yada⁴⁰: showing cylindrical serpentine sheet structure caused by layer mismatch.

1.9.1.3 Antigorite

Antigorite (the name coming from its occurrence at Val Antigorio, Italy) is the final main type of serpentine and has another distinct type of sheet structure. The sheet structure of antigorite has a wavy or corrugated form viewed along its y-axis⁴¹ (Figs. 9 & 12) with the tetrahedral layer occupying the concaves of the sheet. It can appear similar to the platy morphology of lizardite but is characterized by a large a parameter (commonly about 43 \AA ⁴²) forming approximately rectangular fragments. Like lizardite, antigorite crystallises in the Cm space group with the cell parameters; $a=43.53 \text{ \AA}$, $b=9.259 \text{ \AA}$, $c=7.263 \text{ \AA}$, $\beta=91.3^\circ$.

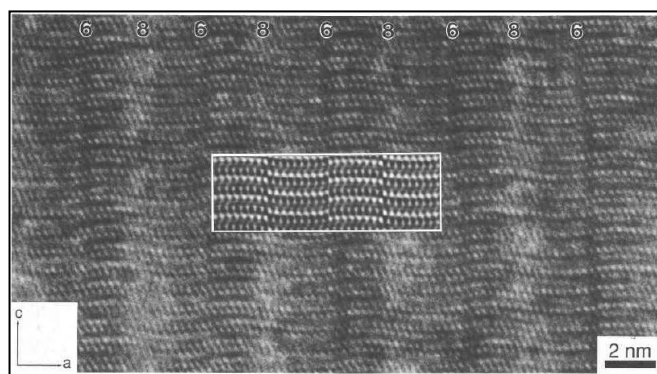


Figure 12: HRTEM image of antigorite from Otten⁴³: showing typical wavy distortion of the serpentine sheet (with simulated pattern insert to show match).

1.9.1.4 Ni-bearing serpentines.

Of the serpentine group there are two known nickel bearing species; nepouite and pecoraite. Nepouite is the Ni analogue of lizardite²⁵ and pecoraite is the nickel analogue of chrysotile⁴⁴. There is no known nickel analogue of antigorite.

1.9.1.4.1 Nepouite

Nepouite (the name coming from its type locality; Nepoui, New Caledonia) is the nickel analogue of lizardite^{45,46}. Like lizardite, nepouite exhibits a platy morphology²⁵ and has cell parameters very close to that of lizardite; $a=5.31 \text{ \AA}$, $b=9.2 \text{ \AA}$, $c=7.27 \text{ \AA}$. However, nepouite crystallises in the space group $Cmc2_1$, not Cm as is lizardite. This difference was first noted by Brindley and Wan (1978)²⁵ in their investigation of the lizardite-nepouite series. They analysed 14 natural samples in the series using XRD, thermogravimetric and chemical analysis and electron microscopy. Although the samples analysed were of reasonably poor quality their results showed that as the concentration of nickel increased through the series the crystal structure changed from monoclinic to orthorhombic. They also noted that at higher nickel concentrations crystallinity was reduced. This change is because the Ni^{2+} ion (69pm) is smaller than the Mg^{2+} ion (72pm) that it substitutes for and this reduces the octahedral sheet parameters changing the mismatch effect in the sheet⁴⁷.

1.9.1.4.2 Pecoraite

Pecoraite (named after Dr William T. Pecora) is the nickel analogue of chrysotile. Pecoraite was first identified as a new mineral phase in 1969⁴⁶. Pecoraite crystallises in the space group $C2/m$ with cell parameters; $a=5.26 \text{ \AA}$, $b=9.16 \text{ \AA}$, $c=14.7 \text{ \AA}$, $\beta=92^\circ$. The first identified

pecoraite mineral was found in the Wolf Creek meteorite where it is suggested that weathering and hydrothermal conditions caused the formation of the mineral from the reaction of nickel and silica. The powder XRD data of the mineral phase was found to be analogous with that of Whittaker and Zussman's data for chrysotile³⁶, except for some line broadening due to the fine grained nature of the material. The electron microscopy study showed some particles to be curved plates, typical of serpentine type minerals. Since the identification of pecoraite a few studies have synthesized this mineral phase. In 2005, Korytkova et al.^{48,49} reported the synthesis of pecoraite nanotubes by heating a mixture of NiSiO_3 and Ni(OH)_2 at high temperature and pressures (400 °C and 70MPa for over 8h). Later in 2009, McDonald et al.⁵⁰ reported success at synthesizing nanotubular pecoraite at significantly lower temperatures and pressures (Fig. 13), 250°C and around 10MPa. This was achieved by reacting nickel (II) chloride, silicic acid and sodium hydroxide using an autoclave charged with 500psi argon.

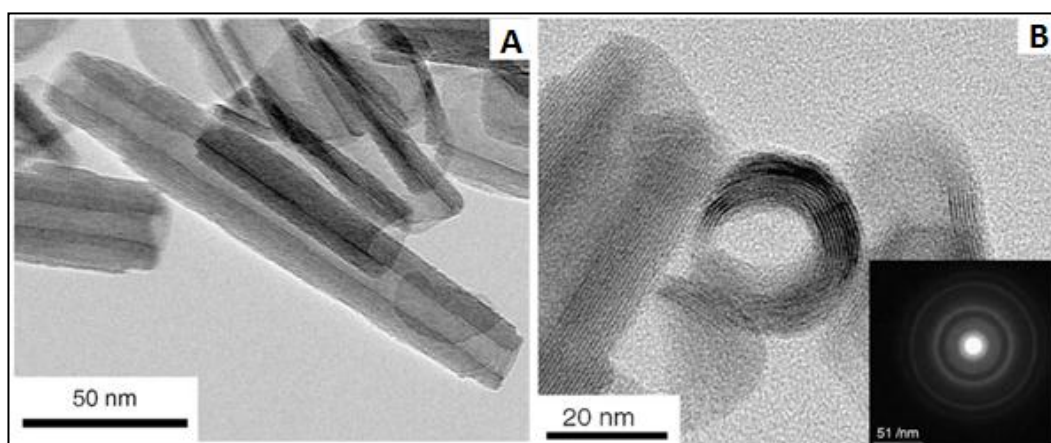


Figure 13: TEM images of synthetic pecoraite from McDonald et al.⁵⁰. A) Side view of tubular particle. B) End on view of tubular particle (with XRD pattern insert)

Nepouite and pecoraite often occur together in lateritic ore deposits, both as fine-grained green minerals. They can be told apart relatively easily using XRD as demonstrated by Milton et al.⁵¹. However, Bilbao et al.²⁶ explained that XRD can prove inconclusive when other minerals in a sample obscure the patterns, in this case electron probe techniques which are effective for identifying morphological characteristics, can be used to discriminate between the different species. Lizardite-nepouite minerals typically exhibit platy morphology with flat layering, which, under an electron microscope is in strong contrast to the typical fibrous nature and cylindrical form of the chrysotile-pecoraite species³⁴. Frost et al.⁵² also

showed that Raman and infrared spectroscopy can be utilised for the distinction between these two phases.

1.9.2. Talc Group

Mineral name:	Approved CMNMC formula:	Strunz Class.	DANA Class.
Talc	$\text{Mg}_3\text{Si}_4\text{O}_{10}(\text{OH})_2$	9.EC.05	71.02.01.03
Willemseite	$\text{Ni}_3\text{Si}_4\text{O}_{10}(\text{OH})_2$	9.EC.05	71.02.01.04

Table 4: Talc group (from Table 2)

1.9.2.1 Talc

Talc $\text{Mg}_3\text{Si}_4\text{O}_{10}(\text{OH})_2$ is a 2:1 trioctahedral layer silicate of the simplest form, where the octahedral layer is sandwiched between two tetrahedral SiO_4^{4-} networks (Fig. 14). As there is no overall layer charge or interlayer cation, the repeating sheets are held together only by weak van der Waals forces; this results in a perfect basal (001) cleavage and makes them characteristically soft. Talc minerals are non-swelling as there are no interlayer species between the TOT repeating sheets.

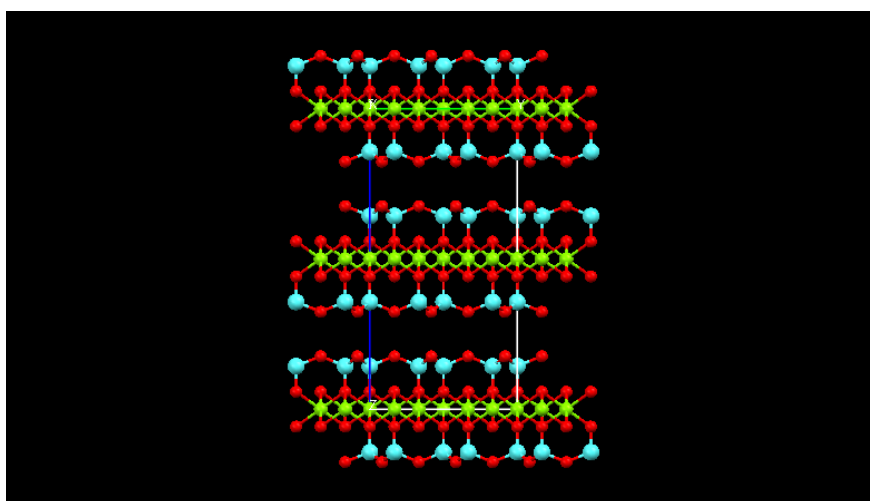


Figure 14: Talc crystal structure⁵³

Talc minerals occur naturally as a metamorphic mineral species, usually from the surface weathering of magnesian minerals such as olivines (e.g. forsterite Mg_2SiO_4) and pyroxenes (e.g. enstatite $\text{Mg}_2\text{Si}_2\text{O}_6$). Talc has wide industrial uses including in paints, cosmetics and lubricant and is well known in the form of talcum powder.

“Talc” refers to the magnesium rich member of the group ($\text{Mg}_3\text{Si}_4\text{O}_{10}(\text{OH})_2$) that crystallises in the C2/c space group with the cell parameters; $a=5.27 \text{ \AA}$, $b=9.12 \text{ \AA}$, $c=18.85 \text{ \AA}$, $\beta=99.3^\circ$ but cation substitution within the talc structure has been reported with cations including Fe^{2+} , Fe^{3+} , Al^{3+} , Ni^{2+} , Mn^{2+} and Zn^{2+} (dependent on its origin and locality)⁵⁵. However, the cation substitutions in these talc structures show relatively limited deviation from the ideal talc composition ($\text{Mg}_3\text{Si}_4\text{O}_{10}(\text{OH})_2$), except in the case of Ni^{2+} substitution.

1.9.2.2 Willemseite

Willemseite ($(\text{Ni,Mg})_3\text{Si}_4\text{O}_{10}(\text{OH})_2$), its name honouring Johannes Willemse, was first identified in 1969⁵⁶. Willemseite is the natural Ni analogue of talc, where Ni occupies over half the octahedral cation sites. Whilst the Ni end-member ($\text{Ni}_3\text{Si}_4\text{O}_{10}(\text{OH})_2$) is not known to occur naturally, the full Ni-Mg solid solution can be achieved synthetically and was reported as early as 1955⁵⁶. Like talc, willemseite crystallises in C2/c space group and has similar cell parameters; $a=5.316 \text{ \AA}$, $b=9.149 \text{ \AA}$, $c=18.994 \text{ \AA}$, $\beta=99.96^\circ$.

The IMA have also suggested that the discredited mineral species pimelite ($(\text{Ni,Mg})_3\text{Si}_4\text{O}_{10}(\text{OH})_2 \cdot n\text{H}_2\text{O}$) is probably willemseite with adsorbed water⁵⁸. ‘Pimelite’ was described as early as 1844⁵⁹ but its definition was never resolved, with controversy over whether it was a non-swelling talc type mineral or a swelling smectite type mineral⁶⁰.

1.9.2.3 Synthetic talc/willemseite

The syntheses conditions for talc-type minerals have been reported a number of times and span a large range of hydrothermal pressures, temperatures and timescales, as well as different starting materials. Synthetic studies of the Ni/Mg talc-willemseite series minerals have generally concentrated on either high pressure and high temperature hydrothermal methods to achieve well-crystalline phases^{56,61} for structural characterisation, or, as in more recent publications, on rapid formation of novel layered-type materials via low temperature

and pressure methods, for applications such as catalysis^{62,63}. Other synthetic studies on isomorphous substitution in talcs include: tetrahedral Ge-Si substitution⁶⁴; F-OH substitution⁶⁵; H-D substitution⁶⁶ and other octahedral substitutions including Co, Mn, Cu, Zn and Fe^{67,68}.

Although several studies have reported the synthesis of octahedrally substituted talc series, very little has been presented on the effect of these substitutions on the unit cell. An exception to this is found in the work of Forbes et al (1969)⁶⁹ who studied the effect of Fe substitution on the unit cell of high pressure and temperature synthetic talcs (utilizing buffer methods to control oxygen fugacity). This study found that whilst a tentative increase in unit cell parameters (c , b and γ) was observed with increased Fe substitution, trends were not linear nor consistent across varying synthesis conditions; the method of substitution of Fe was also much more complex than simple Fe^{2+} octahedral substitution, with tetrahedral substitution of Fe^{3+} and additional H^+ for Si^{4+} also discussed. Ni substitution is not however feasible for Si in the talc structure. Forbes⁶⁹ also indicated that octahedral substitution of Fe^{2+} alone, affects the unit cell dimensions of talc very little.

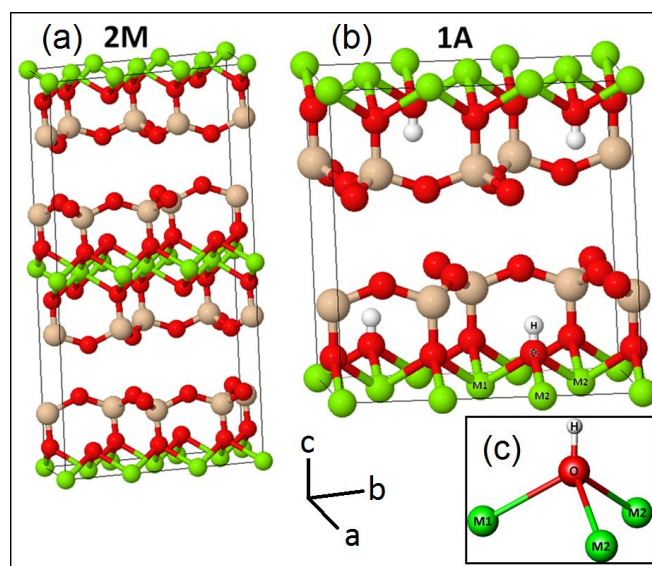


Figure 15: Crystal structures of two talc polytypes: (a) 2M⁵³ and (b) 1A⁵⁴ (c) expanded M₃OH unit from talc structure showing the different octahedral sites M1 and M2. Si (beige), O (red), H (white), Mg (green).

The crystal structure of talc was first described by Gruner (1934)⁷⁰ as the two-layered monoclinic polytype 2M in the space group C2/c. Although Hendricks (1938)⁷¹ also reported

talc in this crystal system, the existence of the 2M polytype has been considered unlikely by several researchers with the suggestion that the reports of two-layered polytypes are due to twinning⁷². The single layer polytype 1A, described by Rayner (1973)⁷³ and later by Perdikatsis (1981)⁵⁴ in the space group C-1 (Fig. 15) is now widely accepted as the most reliable model for talc. This structure of talc allows better incorporation of the stacking disorder, which is inherent in talcs. Stacking disorder arises from either: interlayer displacement, where repulsive forces across the interlayer region are minimized by lateral displacement between the tetrahedral sheets⁷⁴ (Fig. 16.B), or, intralayer shift whereby there is lateral displacement of the lower tetrahedral sheet to the upper tetrahedral sheet in the 2:1 layer (Fig. 16.C). Viani (2002)⁷⁵ described a model for disordered stacking, concerning interlayer displacement, but Kogure (2006)⁷⁶ suggests this model is not persuasive, showing it gives only limited correlation between the experimental and simulated XRD patterns, also pointing out grinding of the sample could have changed the stacking (as described by Perez-Rodriguez, 1988)⁷⁷. Kogure⁷⁶ however, used HRTEM, PXRD and PXRD simulation from cell data (data from Perdikatsis⁵⁴ simulation using DIFFaX software Treacy,) and found a better correlation with intralayer shift.

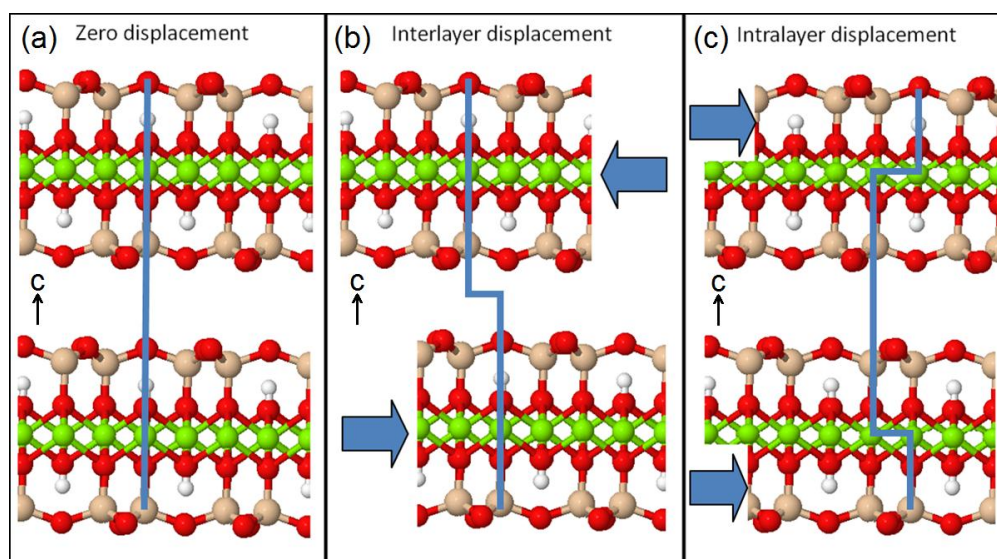


Figure 16: Illustration of layer disorder types in the talc structure. a) Zero displacement,
b) Interlayer displacement (shift of the 2:1 layers relative to each other)
c) Intralayer displacement (shift of the tetrahedral Si sheets within the 2:1 layer)

Si (beige), O (red), H (white), Mg (green).

As X-ray data for layer silicates can be difficult to interpret and information such as the amount of cation substitution is not easily determined using this technique, many studies have used vibrational spectroscopy, particularly infra-red spectroscopy (IR)^{78,79} in characterisation of these materials. In talc, the hydroxyl ions are located below the centre of each hexagonal hole in the silicate sheet, adjacent to 3 Mg cations, two of which are symmetry related (M2) and the third is situated on a centre of symmetry (M1) (Fig. 15).

The vibrational spectrum of talc in the OH-stretch region is particularly simple as the highly ordered OH position, perpendicular to the layer, results in the dipole change giving a sharp weak characteristic band, which is easily identified. OH vibrations can also be used to determine the amount of cation substitution in doped talcs. This method of compositional determination has been reported for the Ni-Mg talc series^{61,68,80}. Ishida (1990)⁶¹ studied the OH-libration region of the IR spectrum, showing systematic changes in relative intensity of the two OH-libration bands at 710cm^{-1} and 668cm^{-1} with increasing Ni substitution, enabling some indication of the amount of Ni-substitution. Wilkins (1967)⁶⁸ studied the OH-stretching frequencies of several synthetic isomorphically substituted talcs (including Ni, Fe, Co, Zn, Mn and Cu) with emphasis on the Ni/Mg-talc series. Samples were synthesized from high-pressure hydrothermal reaction (2-3Kbar, 500-700°C, 15-72h) of mixed hydrated silica and metal hydroxide/carbonate starting materials. The study shows isomorphic substitution in the octahedral layer results in up to 4 separate bands in the OH-stretching region, with good separation observed for the Ni-Mg series. The number and relative intensities of these bands changes systematically with Ni substitution, shifting to lower frequency, which can then be used to determine the Ni/Mg composition. Scholtzova (2003)⁸⁰ later reported a theoretical study of the OH-vibrational spectra of Ni/Mg-talcs, using a quantum mechanical simulation method on a cluster model. Comparison with the experimental data reported by Wilkins⁶⁸ showed good correlation. Both of these studies interpret this in terms of a random distribution of the substituting Ni. However, the difference between the octahedral sites (M1 and M2) is not mentioned and the studied compositions do not fulfil substitution of integral numbers of cations to these sites, i.e. 3 octahedral sites (M1, M2, M2) so substitution of $(\text{Ni}_x, \text{Mg}_{3-x})\text{Si}_4\text{O}_{10}(\text{OH})_2$, where x is 0, 1, 2 or 3 would fill integral sites.

The thermal decomposition of talc has been studied extensively^{81,82}, pure talc shows a relatively simple thermal analysis profile, whereby adsorbed water is gradually removed upon heating and a single weight-loss step is observed around 800-850°C, corresponding to loss of constituent water from the talc formula. This step is a single endothermic transition due to

dehydroxylation, followed by an exothermic transition, as the materials recrystallize to enstatite (MgSiO_3) and quartz (SiO_2)⁶⁵.

1.10. Distribution of Ni^{2+}

The actual distribution of the substituted Ni^{2+} within the octahedral layers was completely unknown until relatively recently due to determinative method limitations. However, since the development of EXAFS as a structural tool⁸³, a few studies have been able to address this⁸⁴⁻⁸⁸. Most of these studies have concentrated on the lizardite-nepouite and/or kerolite-pimelite** series, so do not encapsulate the whole range of Ni-bearing hydrous silicate minerals, nor do they represent a large sample by any means. Nevertheless, there have still been some notable observations made. There are several schemes of distribution that could occur⁸⁵: 1) Distribution of cations in separate layers, either a) in separate particles, or, b) mixed with each other. 2) Distribution within each layer, either a) randomly distributed, b) distributed in clusters, or, c) of ordered distribution. Although it has been observed that all of these theoretical distribution schemes can occur⁸⁵, it has been suggested that the cation distribution displayed by a mineral may give an insight to its formation conditions (such as temperature) and vice versa. Although the sample representation is very small, the lizardite-nepouite series has been shown to display small scale Ni^{2+} clustering within its layer structure^{84,86,88}, indicative of transformation, i.e. the enrichment of Ni with subsequent Mg loss. Conversely, the kerolite-pimelite series has displayed larger scale clustering of Ni within the layer structure, indicative of formation from solution precipitation^{84,88}. Also, the study of synthetic Ni-Mg hydrous silicate series⁸⁵ displayed an increase in cation clustering as crystallization temperatures decreased (250-150°C). With random distribution achieved at a crystallization temperature around 250°C. Although the reasons for these trends are still not understood larger sampling sizes should lead to better comprehension.

** Kerolite ($\text{Mg}_3\text{Si}_4\text{O}_{10}(\text{OH})_2 \cdot n\text{H}_2\text{O}$) and pimelite ($\text{Ni}_3\text{Si}_4\text{O}_{10}(\text{OH})_2 \cdot n\text{H}_2\text{O}$). Although these two mineral phases are no longer recognised by the IMA/CNMNC⁸⁹, there have been a substantial number of works published that refer to them^{90,91}. They have been described as intermediates of talc-smectite type with additional water associated to a non-exchangeable interlayer Ni or Mg cation⁹². The IMA however, suggest that kerolite is likely a disordered talc⁹³ and pimelite is probably willemseite with additional adsorbed water⁵⁸. As such, these assumptions can be made to all references to these minerals in this work.**

2. Experimental Methods

2.1. Solid-state Synthesis Introduction

In comparison to the preparation of discrete molecules, synthesis of materials in the solid state is significantly different⁹⁴. Molecular systems may be altered by reaction in solution to add or remove specific groups and products may also be purified by recrystallization. However, the preparation of solid-state materials requires treatment of the whole lattice and the low solubility of the products often prevents post-synthesis purification. As such, every effort must be made to avoid incomplete reaction (caused by incorrect stoichiometry or unsuitable reaction conditions), which will result in the formation of impurities in the final materials.

Solid-state materials may be prepared via a number of routes, these include: high-temperature (ceramic) reaction and hydrothermal reaction.

2.2. High-temperature methods

High-temperature methods, also known as ceramic methods, involve the “reaction of solid components in the correct molar proportions at elevated temperature over a long period”⁹⁴. This requires accurately and precisely determined masses of starting materials to be combined in a homogenous mixture and hence hygroscopic and non-stoichiometric starting materials are generally avoided.

High-temperature methods are typically quite slow because, as the reaction occurs in the solid state (i.e. not a melt), it relies on diffusion of ions across the points of contact in the material. As the reaction progresses, the diffusion path becomes longer and the reaction rate reduces. In order to ameliorate this situation, various steps can be taken to effectively decrease the path length and increase the points of contact in the mixture as the reaction progresses; increasing the temperature of the reaction, reducing the particle size, forcing the materials into closer contact by pressing the starting materials into a pellet and periodically regrinding and reheating the materials. It is common for these methods to be used in combination and all have been practised in the high-temperature syntheses reported in this thesis.

2.2.1. The basic ceramic method

Once suitable starting reagents are determined, the reaction stoichiometry is used to determine the masses required and these amounts are weighed precisely (for this work this was normally to within 0.001g). The starting reagents are then combined into a homogenous mixture. This may be achieved by solvation or, as more commonly here, by using an agate pestle and mortar or ball mill. The powdered mixture is normally pelletized to improve the contact between the reactants and to minimize contact with the reaction vessel. The pellet is then transferred to a suitable reaction vessel such as a crucible. Selection of the material for the crucible is dependent on several factors including inertness, strength, cost and the working temperature required. Alumina and platinum crucibles have been used in this work as the reaction temperatures are typically very high (up to 1400°C in this work, Fig. 17). The crucible is then heated using apparatus such as a box or tube furnace, which uses resistance heating to attain constant, controlled, high temperatures for long periods of time (here up to 1400°C was sustainable for several days). The heating cycle may be controlled to achieve a desired heating or cooling rate or may include steps for annealing at different temperatures within the range. Multiple heating cycles are frequently used, regrounding the sample after each cycle to enhance homogeneity and promote complete reaction. Determining the optimum annealing conditions and times is often a matter of trial and error and achieving a single-phase product can be very difficult.



Figure 17: Photograph of assorted alumina and platinum crucibles.

2.2.2. Controlled Atmosphere Method

The basic ceramic synthesis method, as described in section 2.2.2.1, is performed in air. However, with modified apparatus, reactions may also be carried out in oxidizing (in oxygen) or reducing (in nitrogen or hydrogen) conditions which can allow different oxidation states to be achieved. This can be done most simply by attaching a bottle of the desired gaseous atmosphere to one end of a silica tube, which is inserted in a tube furnace, with the sample in a crucible/boat in the silica tube so it is located the center of the furnace (i.e. the heated portion of the furnace). The other end of the silica tube is attached to a bubbler so as to monitor the flow of the gas and to ensure no backflow of air into the tube (Fig. 18). The gas flow through the tube should be maintained throughout the reaction, as well as for a period before applying heat (preferably at a higher initial rate, to purge the system) and until the sample has cooled after the heating cycle is complete. Therefore, care should be taken to ensure that the flow is significantly low as to ensure the bottled gas does not run out.

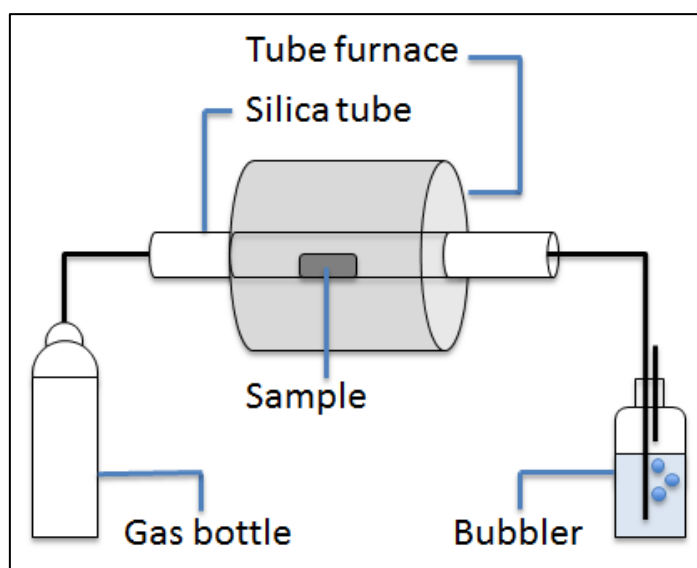


Figure 18: Diagram of a controlled atmosphere reaction setup.

2.2.3. Sealed Tube Method

The sealed tube method is a variation of the ceramic method which enables volatile reactants to be used and unusual oxidation states to be accessed. If the starting materials are air sensitive, as in the case of FeO used in some of the experiments described in this thesis, the

homogenous mixture must be prepared in a controlled atmosphere. In respect of the work carried out in this thesis, the controlled atmosphere environment was provided by using a Braun glove-box. The combined starting materials are placed into a glass or quartz ampule. The ampule is then evacuated using a vacuum line and with the tube under active vacuum, the neck of the tube is heated using a blowtorch to melt the glass/quartz and seal the contents inside. The sealed tube is then placed in the center of a tube furnace and heated. When the heat cycle is finished the tube is scored and carefully broken open to retrieve the sample inside.

To prevent sample materials reacting with the sealed tube material, a graphite coating is often applied to the inside of the ampule. This is done by putting a small amount of a solvent, such as acetone, into the ampule and heating to white heat with a blowtorch to decompose the solvent into carbon which is deposited as a film on the inner surface (Fig. 19).



Figure 19: Photograph of a quartz ampule (c.10mm diameter) with internal graphite coating for use in sealed tube reaction experiments.

2.3. Hydrothermal Methods

Solvothermal methods involve carrying out reactions in a solvent that is sealed and heated. In these experiments which are mimicking nature, the solvent is water and the reactions are described as hydrothermal. Water that is heated in a sealed vessel may be superheated (above 100°C) or even supercritical (above approximately 374°C), to generate significantly high-pressure conditions. These elevated temperature and pressure conditions can allow reduced reaction times and temperatures for some reactions. The range of temperature and pressure dictates the type of vessel that can be used for the reactions as extreme conditions can require the use of very specialized equipment.

2.3.1. Parr® PTFE Lined Hydrothermal Bombs

PTFE lined hydrothermal bombs made by Parr® are relatively simple pieces of equipment. For this project two sizes were available, 25ml and 125ml; these allow a maximum reaction mixture volume of approximately 2/3 of that value. The vessel is sealed by tightly compressing the lid and body of the PTFE liner using the outer steel body to create a flat gasket seal, encapsulating the reaction mixture. The vessel is then heated by placing in a temperature controlled oven at up to 250°C, allowing a maximum pressure of approximately 124 bar (Fig. 20).

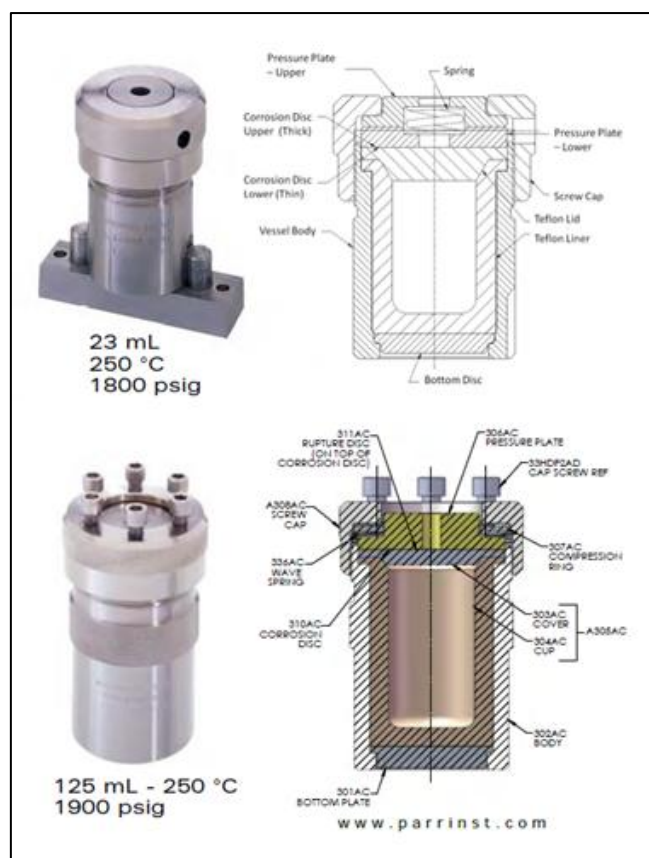


Figure 20: Images of Parr PTFE lined hydrothermal bombs with corresponding cross sectional diagrams, as used in this study.

2.3.2. Tuttle Apparatus

Many of the mineral types that are relevant to this study are formed naturally under hydrothermal conditions at high pressures and temperatures below the Earth's surface. To

replicate these conditions a purpose-built Tuttle-type cold-seal high-pressure hydrothermal rig was used. This rig is capable of providing controlled reaction conditions of up to 800°C and 3kbar (300MPa) pressure.

Tuttle-type cold-seal apparatus is widely used in geological research. The “cold-seal pressure vessel” was developed by O.F. Tuttle (1949)⁹⁵ and uses a simple cone in cone seal (whereby a seal is created by the deformation of a metal cone as it is tightened into a smaller cone) at one end of an alloy rod, which has a hole bored to near the opposite end. Reagents are sealed in a capsule (generally made from precious metals) that is inserted into the bored rod and the remaining volume is filled with fitted filler rods of the same alloy to minimise the internal volume. Water is used as the pressure medium and heat is applied externally to the reaction vessel, with the cold-sealed end kept external to the heating source to minimise the possibility of heat deformation.

Since its inception the cold-seal apparatus has been developed and improved by several researchers to further increase temperature and pressure limits and the levels of control of these conditions but the principle remains the same.⁹⁶⁻⁹⁸

The apparatus used in these experiments utilises Rene77 alloy reaction vessels. Rene77 is a nickel based super alloy used for applications that require strength at high temperatures, making it suited to this work (Fig. 21).

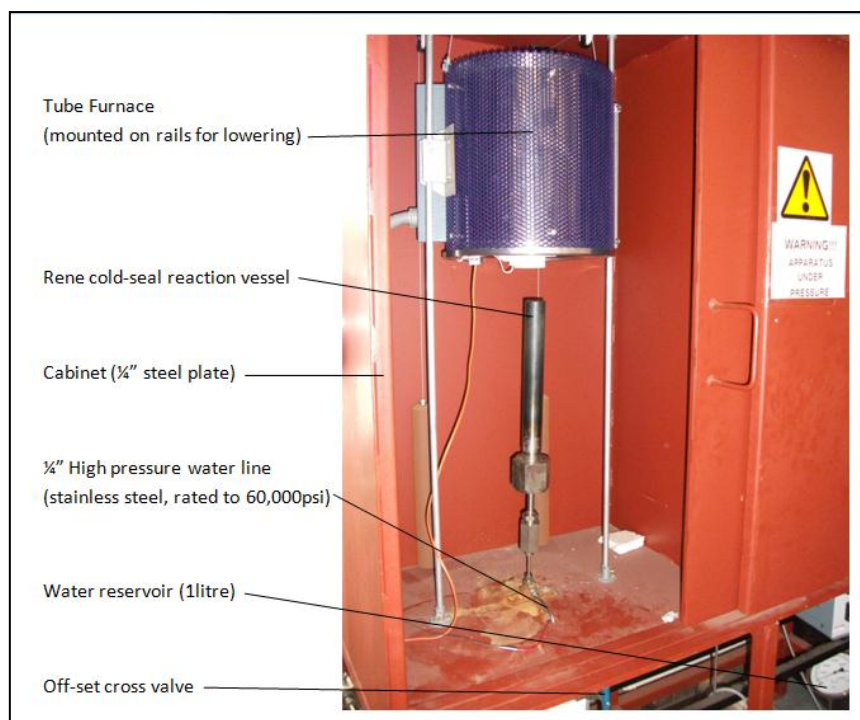


Figure 21: Labeled photograph of the Tuttle-type hydrothermal rig.

Pre-fabricated Au tubing (Au purity >99.9%, wall thickness approx. 0.25mm, external diameter approx. 9.5mm) has been used to make sealed reaction capsules. To do this the Au tube was annealed at 750°C for 3hrs to remove faults and make the material malleable for welding. The tube was then sealed at the bottom (in a 3-point wedge to prevent it getting lodged inside the reaction vessel) using a pen-type graphite arc welder, with the nib sharpened to a fine point to allow intricate, precise welding. All welds were inspected under a microscope to ensure the tube was completely sealed. Reagents were then loaded into the capsule and the top was also weld-sealed into a 3-point wedge (Fig. 22) whilst ensuring no reagents contaminated the seal.

If a solvent was to be sealed inside the capsule (e.g. H₂O) this was added by needle injection when the capsule was almost completely sealed. This minimised evaporation of the solvent during welding which otherwise causes problems in creating a good weld. In some cases volatility was a problem, so the contents of the capsule were frozen by dipping in liquid N₂ prior to creating the final sealing weld. This allowed more time to form the weld before the liquid is vaporised by the heat of welding.



Figure 22: Photographs of: Left - arc welding apparatus for sealing gold tubes.

Inset right – Close up of arc welded 3-point weld-sealed gold tube.

The mass of the sealed Au-capsule was recorded then it was loaded into the reaction vessel. Filler rods were then added to minimise the internal volume (Fig. 23). The remaining volume (max. 5ml) was filled with distilled H₂O and the vessel was tightly sealed using a vice and 36” Stilson wrench. The reaction vessel was then attached to the rig using a prepared length of coned and threaded high-pressure tubing. The vessel, line and reservoir were tested for leaks by increasing the pressure by hand-pumping to 1kbar and leaving overnight to check for any pressure loss.

For reactions below 1.5kbar; the vessel was left open to the reservoir while the reaction was heated to temperature (under supervision) using the tube furnace. When the vessel reached equilibration at the desired temperature (min. 3hr) the reservoir was closed and pressure was increased to the desired level using the water pump.

For reactions above 1.5kbar; because the water pump could only reach pressures up to 1.5kbar an alternative method, which required very close supervision, was used to achieve higher pressures. The vessel was isolated from the main line at approximately 1kbar. The temperature of the reaction vessel was then increased slowly and the pressure constantly monitored. As the pressure rose with increasing temperature, it was periodically reduced by carefully opening the vessel to the reservoir (note, near the critical point of water, the

pressure in the system rises more rapidly). When the required temperature and pressure were obtained equilibration was monitored (min. 3hr) to ensure stability.

After the required reaction time, heating was stopped and the vessel was carefully opened to the reservoir to reduce the pressure and balance any fluctuations during cooling. Once at ambient temperature, the vessel was closed to the line and removed from the rig. The Au-capsule was removed and weighed to check integrity then opened with cutters to remove the sample.

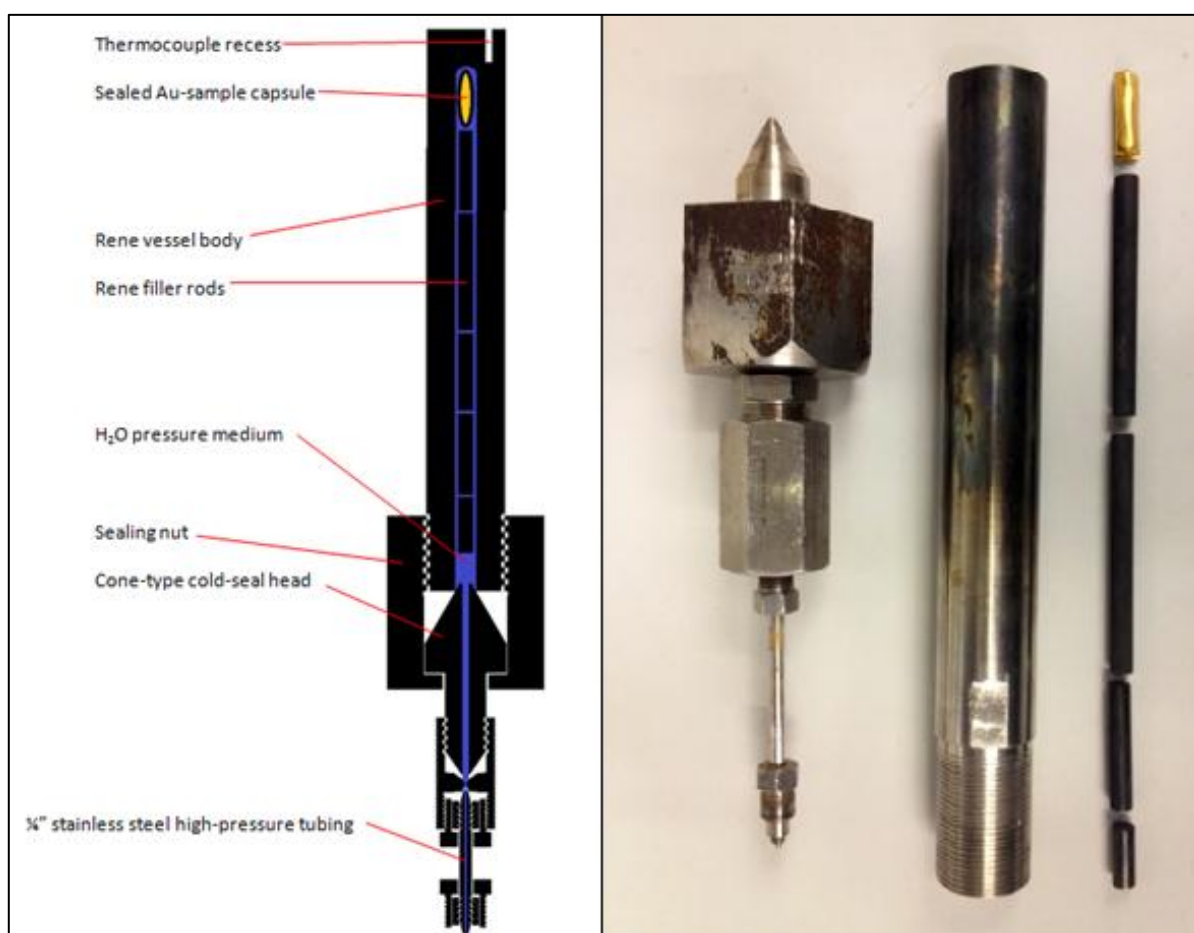


Figure 23: Tuttle rig hydrothermal bomb: Left – Cross sectional diagram of hydrothermal bomb. Right - Photograph of hydrothermal bomb components

3. Characterisation Techniques

Characterisation of natural and synthetic materials has been carried out using several complementary techniques. These include powder X-ray diffraction, electron probe microanalysis, thermal analysis, Raman and infrared spectroscopy.

This section discusses the theory behind each of these techniques, its application for these types of materials and the standard procedures and parameters used.

3.1. Powder X-ray Diffraction (PXRD)

3.1.1. Theory of PXRD

The principal theory of any diffraction technique is the interaction of a beam of radiation with matter, causing scattering of the radiation beam. As the name suggests powder X-ray diffraction (PXRD) uses X-ray radiation, which is scattered by a polycrystalline solid (i.e. a powder).

When an X-ray beam impinges on a crystalline solid made up of an ordered arrangement of atoms/ions it interacts with the electrons of the atoms/ions and is scattered. A crystalline phase can be thought of as an ordered lattice of atoms/ions consisting of repeating planes with translational symmetry. The relation of these planes to the unit cell is described by “Miller Indices” denoted by h , k and l , which correspond to reciprocal values along the unit cell (0 being the origin and 1 being the cell length), these then define the Miller plane (hkl) (see Fig. 24).

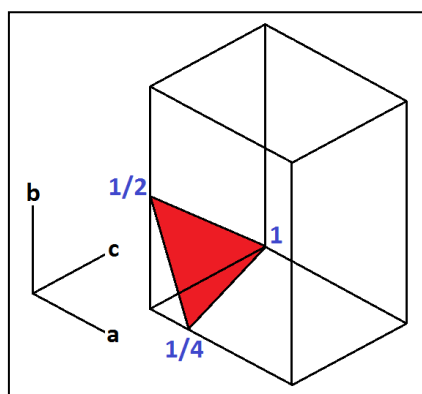


Figure 24: Representation of the Miller plane (421) corresponding to a plane that intercepts: **a:** $\frac{1}{4}$, **b:** $\frac{1}{2}$ and **c:** 1.

Scattering of the X-ray beam from these planes generates interference that can be either constructive or destructive. Constructive interference, i.e. waves which are scattered in-phase, is known as diffraction and the intensity of this is measured (Fig. 25). For diffraction to occur the scattering conditions must satisfy the Bragg equation:

$$n\lambda = 2d_{hkl} \sin\theta$$

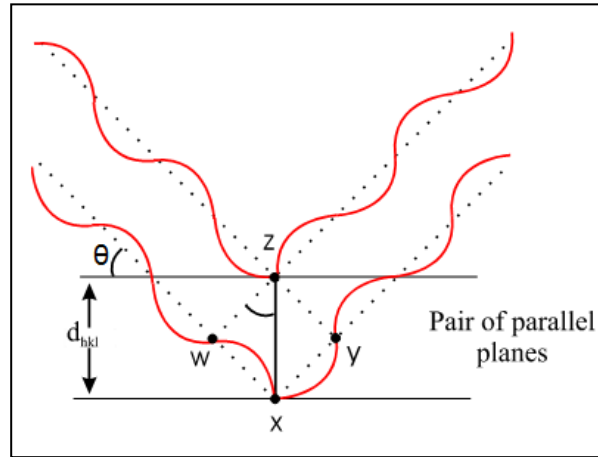


Figure 25: X-ray diffraction from a set of parallel planes⁹⁴.

Therefore, where n is an integer and λ is the X-ray wavelength, $W-X$ and $X-Y$ ($d_{hkl} \sin\theta$) must be an integral number of wavelengths, as path difference is dependent on both the plane spacing (d_{hkl}) and the incidence angle of the X-ray beam (θ). From this it can be seen that for diffraction from different planes to be observed variation of either the wavelength or the angle of the incidence is required. The angle and intensity of the diffracted beam which is observed depends on the size and shape of the crystal structure's unit cell, its space group and the type of atoms present. Thus, collection of diffraction data (known as a pattern) can be used to generate the full crystallographic structure of a material.

3.1.2. X-ray generation

X-ray generation can be explained as the interaction of an incident high-energy electron with electrons from the inner shells of atoms (see Fig. 26). An incident electron with sufficient energy can cause the ejection of an inner-shell electron from a stable orbit in an atom;

relaxation of another electron into this hole allows generation and emission of an X-ray photon.

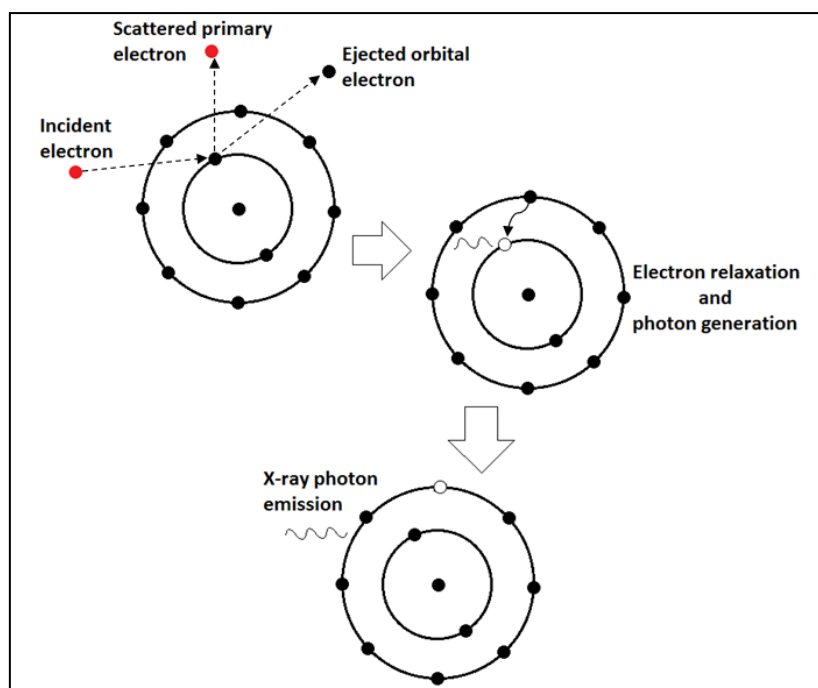


Figure 26: Schematic diagram of X-ray generation from a simple atom.

The energy of the generated X-ray photon is equal to the energy difference between the two energy levels, so is controlled by the electronic transition that occurs, K X-rays (the most energetic) are emitted when an electron from the innermost shell is ejected, L X-rays are emitted when an electron is ejected from the second shell and so on, with energy decreasing as the distance from the nucleus increases. The X-ray properties are also defined by the location from where the relaxing electron originates, e.g. $2p$ to $1s = \alpha$, $3p$ to $1s = \beta$ and the spin state of the electron which is referred to by a subscript 1 or 2. $K_{\alpha 1}$ X-rays have the highest generated intensity so are primarily selected for use in monochromatic (single wavelength) powder diffraction.

In an X-ray diffraction instrument this process of generating X-rays is performed by an X-ray tube. An X-ray tube uses a heated tungsten filament to produce electrons (by thermionic emission); the electrons are accelerated in a vacuum and fired at a defined metal target (typically Cu, Co, Fe or Mo) to generate X-rays. The X-rays can then pass through the beryllium window in the tube (see Fig. 27).

The generated X-ray radiation then goes through a monochromator to block unwanted X-rays, such as $K_{\alpha 2}$, $K_{\beta 1}$ and $K_{\beta 2}$. The remaining ($K_{\alpha 1}$) X-rays are then passed through a collimator and a series of slits to focus the beam into a single direction.

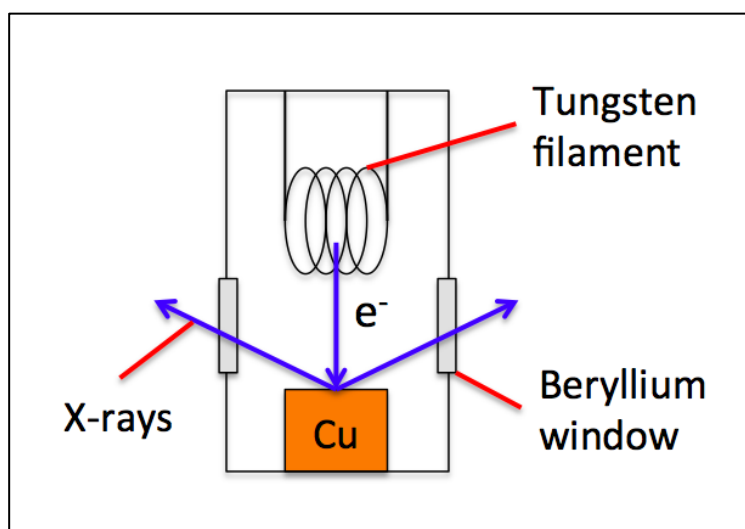


Figure 27. Diagram of an X-ray tube

3.1.3. XRD Instrumentation

At the most fundamental level, instrumentation of an XRD experiment requires: a source of X-ray radiation (X-ray tube), a sample to be analysed and a device (of known orientation, relative to the X-ray source and sample) capable of detecting the scattered X-rays. The actual composition of such an instrument can vary greatly. A typical laboratory based instrument (and the type used for the majority of this work) is that of fixed wavelength and variable incident angle (Fig. 28)⁹⁴. The sample (located in the sample stage) is a polycrystalline (powdered) material mounted such that a flat surface incident to the X-ray beam is ensured. The detector has a well-defined geometry due to the goniometer set up.

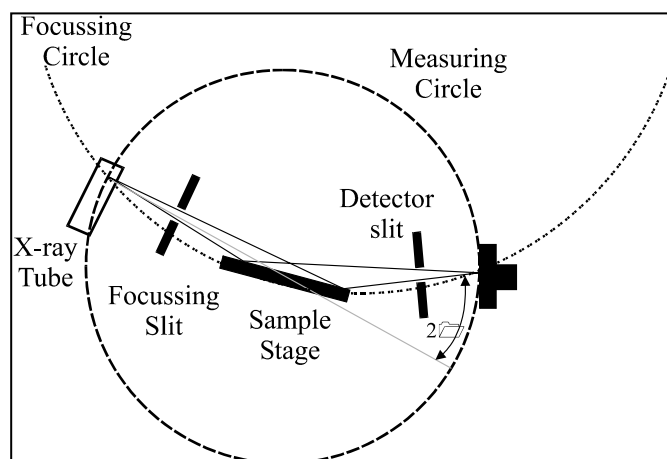


Figure 28: Diagram of goniometer PXRD instrument⁹⁴.

3.1.4. Synchrotron Source PXRD

A synchrotron is type of particle accelerator that is used to generate very high intensity X-ray beams, 100-10,000 more intense than $K\alpha_1$ radiation from X-ray tubes. This allows significantly better resolution and reduced data collection times; giving more detailed structural information compared to a standard X-ray tube instrument.

Electrons, which originate from an electron gun, are accelerated to velocities close to the speed of light using a series of particle accelerators called: the linear accelerator (aka: Linac), the booster synchrotron and the storage ring (Fig. 29). The “storage ring” is strictly a polygon of straight sections in which the electrons are forced to travel in a near circular path by dipole (bending) magnets that are placed at regular intervals. The action of the magnets on the electrons causes them to loose energy, which is emitted in the form of synchrotron radiation that covers a wavelength range from infrared to very short X-ray wavelengths. This radiation is then tunnelled from the storage ring to “experimental stations” where it meets a crystal monochromator, set to reflect the particular wavelength required. Each experimental station (also known as a “beam line”) is optimised for a particular type of experiment.

Aside from the higher intensity that is achieved with a synchrotron source, the radiation also differs from an X-ray tube instrument, in that a synchrotron source monochromator can be “tuned” to reflect a desired wavelength as opposed to the fixed nature of an X-ray tube. Also, radiation from a synchrotron source is polarised (in the plane of the storage ring) whereas an X-ray tube is unpolarised. Although synchrotron source PXRD offers significantly greater

power for structural resolution, access to these resources is generally very limited and expensive in comparison.^{99,100}

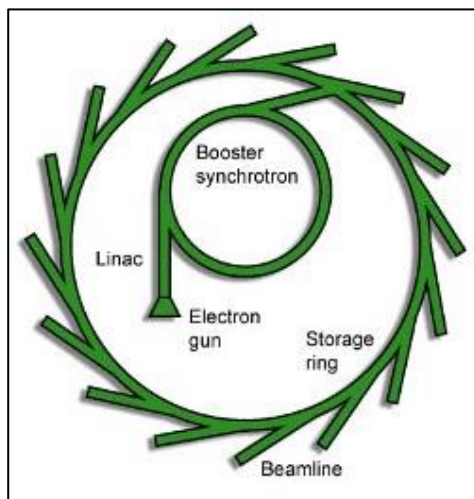


Figure 29: Diagram of the Diamond synchrotron light source

3.1.5. Application of PXRD to Saprolitic Minerals

Powder X-ray diffraction is a widely used characterisation technique in this area. Databases, such as ICDD (International Centre for Diffraction Data) are used to analyse PXRD data and identify phases present. XRD also gives an assessment of how crystalline phases are and can be used in some situations to give, quantitative or at least semi-quantitative information too.

The choice of X-ray radiation source can prove to be quite important in the study of saprolitic minerals. Copper is the most common source of radiation in use and is suitable for most samples, but problems can arise if certain elements, such as iron, are present in the sample. Due to the energy of the copper radiation, excitation within the iron atoms/ions occurs that generates secondary fluorescence, leading to XRD patterns with high backgrounds. The use of cobalt radiation, for instance, when analysing iron-containing materials, does not produce this fluorescence effect. Other advantages in using cobalt-radiation, are improved peak resolution due to the radiation having a longer wavelength.

PXRD data collected on the target mineral groups (see Table 2) have characteristics that can assist in their identification. Serpentine group ($M_3Si_2O_5(OH)_4$) minerals typically exhibit a strong basal (001) reflection at around 7.3\AA with the (002) reflection occurring around half this at about 3.65\AA . For the amesite group minerals ($M_2Al(Si,Al)_2O_5(OH)_4$) the (001) and (002) reflections are observed at slightly lower d-spacing of 7.05\AA and 3.52\AA . Talc ($M_3Si_4O_{10}(OH)_2$) yields a strong (001) reflection at around 9.3\AA and a strong (003) reflection at 3.11\AA . Chlorites ($(M_{4-6}(Si,Al,B,Fe)_4O_{10}(OH,O)_8$) typically show a reflection about 14.2 - 14.4\AA . Smectites ($(Na,Ca)_{0.3}M_{2-3}(Si,Al)_4O_{10}(OH)_2.nH_2O$) typically exhibit broad reflections caused by random layer stacking, these reflections tend to be asymmetrical towards the higher angles.

As with all techniques, PXRD does have limitations: it determines averaged structural characteristics of samples so limits of detection can be relatively low and minor constituents can go undetected; little information can be drawn from poorly crystalline samples (typical of species such as the smectites); isomorphous substitutions (e.g. substitution of Ni^{2+} for Mg^{2+}) can be difficult to detect. Another problem common to XRD of saprolitic minerals is preferred orientation. The platy nature of many of the saprolitic minerals can cause the particles to align increasing the intensity of reflections from certain lattice planes.

3.1.6. X-ray Diffraction Experiments

For this research, Powder X-ray Diffraction (PXRD) has been the principle technique used to determine the phases present in samples.

PXRD data were collected on a Bruker D8 Advance and a Nonius PDS120 powder diffraction system with an INEL curved position sensitive detector. Synchrotron based high-resolution PXRD and a micro-diffraction instrument has also been used to collect diffraction data in this work.

All diffraction data were analysed using STOE WinXPOW v2.08 software. Phase identification was carried out by search-match procedures in the software, using the Powder Diffraction File PDF-2 supplied by the International Centre for Diffraction Data (ICDD). Unit cell parameters were refined using the Pawley refinement method, part of the Topas Academic v4.1 software.

A Bruker D8 Advance system was used to collect PXRD patterns at Loughborough University. The Bruker D8 Advance system used Cu K α_1 ($\lambda = 1.5406\text{\AA}$) radiation selected from the primary beam using a germanium 111 single-crystal monochromator and position sensitive detector (PSD). Diffraction patterns were collected using Cu K α_1 (1.5406\AA) radiation, over a chosen 2θ range between 5° and 100° , using a step size of 0.00717106° , for a given time (2-12h). Samples were powdered using an agate pestle and mortar and either mounted on a flat silicon substrate or in a shallow-well Si-substrate (depending on sample size available). Samples where diffraction patterns were collected for refinement were also prepared with an internal standard for calibration. This was done by combining the sample with powdered silicon (NIST-Si SRM640b), using the agate pestle and mortar, to give a homogenous mixture. All samples were rotated throughout data acquisition.

The standard run period used for phase identification was for 2h, over a 2θ range of 5° - 60° , although some samples were run over longer times and/or 2θ ranges to improve data quality. Data acquired for refinement was collected for 4h, over a 2θ range of 5° - 80° .

A Nonius PDS120 Powder Diffraction System with an INEL curved position sensitive detector (PSD) was used to collect PXRD patterns at the Natural History Museum, London. This detector has an output array of 4096 digital channels, representing an arc of 120° 2θ , permitting the simultaneous measurement of diffracted X-ray intensities at all angles of 2θ across 120° with a static beam-sample-detector geometry. This diffractometer also used Copper K α_1 radiation, selected from the primary beam using a germanium 111 single-crystal monochromator. Data collection times were 30 minutes for each sample and the angular range recorded was 4° - 120° 2θ . NIST silicon powder SRM640 and silver behenate were used as external 2θ calibration standards and the 2θ linearization of the detector was performed using a least-squares cubic spline function. Samples were powdered using an agate pestle and mortar and mounted on a quartz substrate, which was rotated during data acquisition.

Synchrotron high-resolution PXRD was carried out on beamline I11, at the Diamond Light Source Synchrotron facility in South Oxfordshire.¹⁰¹ Data were collected using synchrotron radiation at a wavelength of 0.82626\AA , over a 2θ range 0.935 - 151.740° for 30 min. Samples were prepared as a fine powder mounted in a 0.7mm sodium borosilicate capillary and the capillary was rotated throughout data acquisition.

X-ray micro-diffraction was carried out at the Natural History Museum using their custom micro-source instrument. The micro-source instrument is based on the Nonius PDS120 system, using a $\text{CuK}\alpha$ radiation source that was focused to give a “beam footprint” of around 1mm^2 on the surface of the sample; this allowed the sample to be mounted in a static position to give separate XRD patterns for individually selected points of interest. Diffraction data were collected at each point for 15 min. Unlike the PXRD samples, samples for the micro-diffraction experiments were prepared as thin sections on microscope slides.

3.2. Electron Probe Microanalysis (EPMA)

Although the relationship between atomic number and generated X-ray lines has been known for some time the “electron microprobe” was first described by Castaing and Gunier in 1950¹⁹.

Electron probe microanalysis (EPMA) combines the high magnification imaging capabilities of scanning electron microscopy (SEM) with the ability to perform non-destructive chemical analysis of a very small volume ($<30\mu\text{m}^3$) of a solid sample, with good detection limits for most elements (B-U, down to 100ppm). This enables information to be determined such as crystallite size and morphology along with chemical compositions and variation thereof, making it a valuable tool for the study of both natural and synthetic minerals.

EPMA generates information by firing a focused, accelerated beam of electrons (of known current and voltage) at a sample, either in a static spot or in a raster pattern across the surface. When the electron beam interacts with the sample it causes stimulation effects within a small volume near the surface of the sample (see Fig. 30), these effects include the emission of, secondary electrons, back-scattered electrons, characteristic X-ray radiation, cathodoluminescence, bremsstrahlung and auger electrons. Detection of these effects can provide different types of information about the sample. The effects discussed here are secondary electron, back-scattered electron and characteristic X-ray radiation generation and detection, as these are the most relevant to analyses that have been performed in this study.

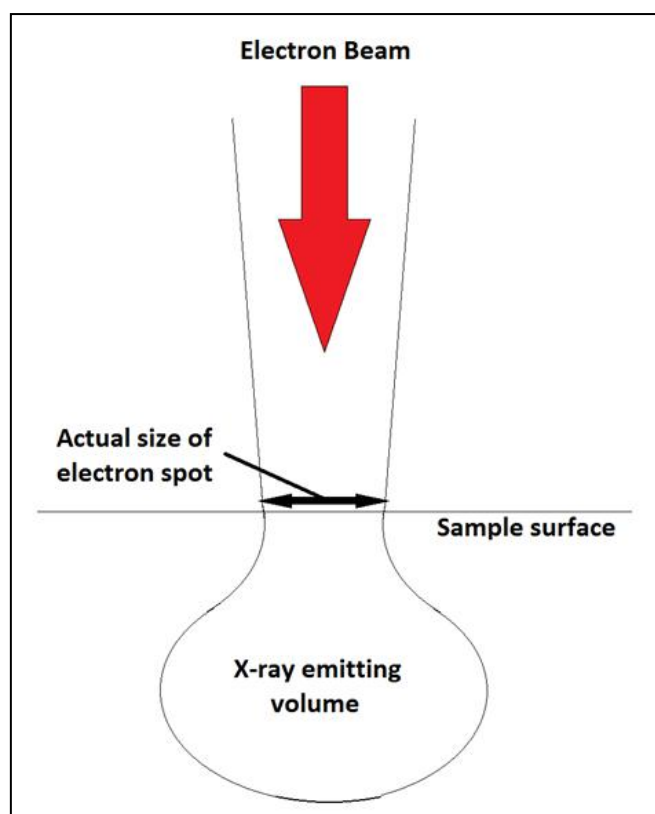


Figure 30: Schematic diagram of EPMA beam analysis volume

3.2.1. Secondary Electrons

Secondary electrons are low-energy (c. 50eV) inelastically scattered electrons that are emitted from the sample when it is bombarded with high-energy electrons (c. 20keV). These are attracted to a detector off to one side of the sample by a positive electrical bias (c. 200V). The collected electrons are accelerated towards a phosphor scintillator in a photomultiplier tube and the current from this is used to modulate brightness on a display. This gives a high-resolution image that provides topographical information on the sample surface, as if viewed from the perspective of the electron beam and lit from the position of the detector (Fig. 31). Secondary electron imaging (SEI) allows easy identification of surface irregularities; secondary electrons are only emitted from a shallow zone under the surface so sharp edges, corners and holes allow electrons to escape in several directions resulting in a bright line in the image. This is useful as edges and holes can provide complex/inaccurate data for elemental analysis.

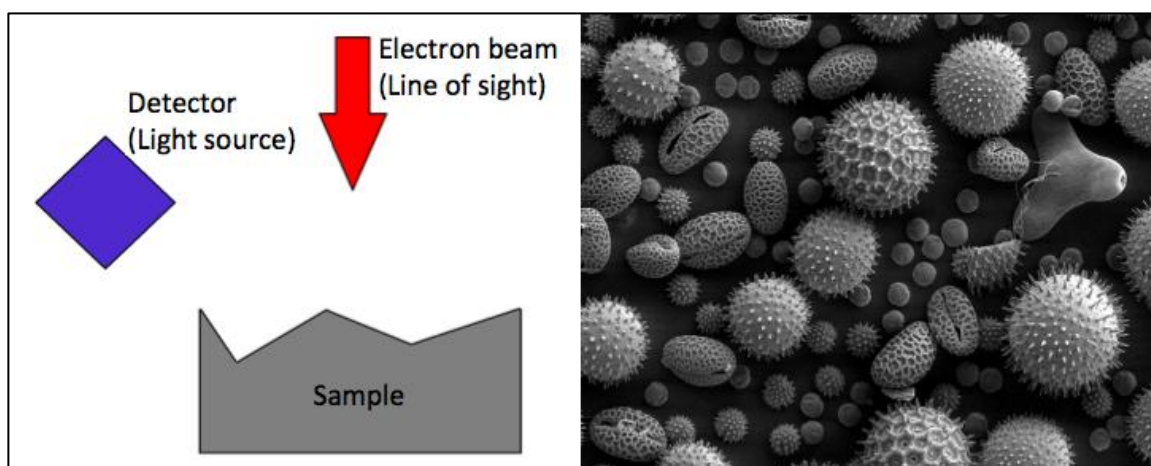


Figure 31: Left - Diagram of secondary electron detector geometry. Right – Example of a secondary electron image illustrating the topographical information achievable.

3.2.2. Back-scattered Electrons

Back-scattered electrons are high-energy electrons scattered from elastic interactions with atoms of the sample. A back-scattered electron detector sits in a ring around the electron beam, directly above the sample, this means only those electrons that are deflected through a very high angle reach the detector. The number and energy of these electrons depends on the sample composition, as backscatter coefficients, known as η (Eta), show a strong relationship with elemental composition. η (Eta) is defined by:

$$\eta = \frac{\text{number of electrons scattered out of sample}}{\text{Number of electrons in the beam}}$$

As the average relative atomic number of the sample volume increases, the backscatter coefficient is increased. High atomic number elements absorb less of the incident electron energy due to their lower electron to unit mass ratio; this corresponds to an increase in brightness in a back-scattered electron (BSE) image.

3.2.3. Characteristic X-rays

EPMA generates X-rays using in much the same way as an X-ray tube (as described in the PXRD section), however instead of the accelerated electron beam being directed at a defined metal target, generating a specific type of X-ray, the beam is directed at a sample under

investigation. Since the energy and wavelength of the generated X-rays are related to the atomic number of the element from which they are generated, and the intensity is related to the quantity of that element, the properties of these characteristic X-rays can be used to determine compositional information for an unknown material.

As illustrated in figure 30, the analysis volume from which X-rays are emitted is significantly larger than the beam spot size. The X-ray emitting volume is determined by 2 main factors: the beam accelerating voltage, which determines the diameter and the atomic composition, which determines the shape. Theoretically, reducing the accelerating voltage should give better analytical resolution, however this results in reduced intensities so a compromise has to be found to collect adequate data.

Emitted X-rays can be detected in two different ways, using wavelength dispersive spectrometry (WDS) or energy dispersive spectrometry (EDS) to determine the elemental composition of the analysis volume. WDS and EDS are often both fitted to the same instrument but detect the generated X-rays in different ways.

Wavelength dispersive (X-ray) spectrometry (WDS/WDX) uses a curved crystal of known d-spacing to diffract a specific wavelength of X-ray radiation (according to Bragg's law) relating to a particular element, the curvature of the crystal focuses the diffraction beam towards the detector. The crystal can then be moved to diffract a different wavelength of radiation. This technique has very good resolution. However, as the detector is a long way from the sample required counting times and beam currents are increased. Also, several different crystals are required as each is only useful over a small range of wavelengths.

Energy dispersive spectrometry (EDS) uses a solid state detector, which produces a voltage pulse proportional to the energy of the interacting X-ray photon; these pulses are sorted, measured and counted by a multichannel analyser to generate a spectrum. The detector is positioned close to the sample, collecting X-rays over a large angle. This allows shorter analysis times than WDS as well as a reduction in beam current which; reduces the possibility of sample alteration by the electron beam and gives beam conditions compatible with higher resolution imaging. However, spectral resolution is significantly lower for EDS with peak overlaps causing poorer quantification of the elements present.

Both of these detection techniques, coupled with BSE-imaging can be used to collect elemental data at specific points on a sample or, alternatively, to provide maps of larger areas

to show the distribution of elements across the sample. This technique is however unable to measure hydrogen and light elements up to fluorine are generally not measured directly, due to the complexity of matrix corrections required and the uncertainty these corrections introduce. Therefore, oxygen is normally calculated by stoichiometry instead, assuming cations exist as simple oxides.

3.2.4. Application of EPMA to Saprolitic Minerals

EPMA allows the heterogeneity of the specimens to be determined with visualisation of distinct phase formations and relationships and important information on how the elemental compositions vary on a micro-scale.

However, the technique also has some clear limitations for the analysis of these types of (hydrous) minerals. The soft and layered nature of many of the samples can make preparation of a smooth surface very difficult. If the surface is not smooth, for example if scratches are present from the grinding or lapping stages of preparation, the path length of the beam will vary across the sample which will change the amount of X-ray absorption (an effect which cannot be accurately modelled by matrix corrections). Also, the hydrous nature of these materials leads to significant uncertainty in the analysis data. This is because O and H are not measured by the microprobe, this results in an automatic reduction in the analysis totals, although these totals can be modelled from formulae calculations, this effect makes identification of poor analyses much more difficult, for example analyses taken at grain boundaries, which effect the analysis totals, become more difficult to identify.

Also, the hydrous and inherently fine grained nature of these samples cause complications with analysis: because the materials are hydrous they are susceptible to alteration (i.e. reduction of H₂O content) caused by both the high energy electron beam and also the high vacuum which is required in the instrument, this alteration effect can be reduced by enlarging the beam spot size. However, a larger spot size also causes problems, as the fine-grained nature of these samples (typically <4µm) makes it impractical because it increases the likelihood of taking measurements at grain boundaries causing further issues. Reduction of analysis times also reduce the effect of sample alteration but result in reduced data quality, i.e. poorer signal to noise ratios.

Finally, problems can also arise where elements, such as Fe (common in saprolitic material), occur in more than 1 oxidation state e.g. Fe^{2+} and Fe^{3+} . This is because the instrumentation bases oxygen quantification on set a of oxide standards (commonly fatality Fe_2SiO_4 for Fe, i.e. Fe^{2+}), therefore if Fe occurs in the +3 state in the sample, oxygen quantities will not be correctly represented and unless the quantity of Fe^{3+} is known this is not easily corrected for. Similarly, elements such as Al, which can occupy both octahedral and tetrahedral sites, can cause complications for mineral formulae calculations.

The nature and complexity of the studied specimens coupled with the limitations of the technique introduce general problems as well as problems specific to each sample. For (these) data to be considered valid these shortfalls must be at least acknowledged and justified.

Ideal models for individual mineral species can be calculated to give expected experimental totals and wt.% oxide values for each cation ($\text{H}_2\text{O}\%$ cannot be measured but can generally be assumed to be the difference between the experimental total and 100%). However, comparison of formulae determined from models, with those calculated from the data is not ideal, due to the variation in stoichiometries and presence of other cations in these systems.

Despite this, some guidance can be taken from general ranges for expected data. For example, in a sample containing a serpentine phase with both Ni and Mg, by calculating the end-member ideal data for Mg-serpentine and Ni-serpentine it can be assumed that these should be the approximate limits expected for points where a serpentine phase is observed. However, this becomes much more difficult to assess with substitution of other elements.

Deviation of experimental data from these ideal ranges can also be expected but must be explained. The most frequently encountered problem associated with these samples is large variation in the experimental totals. Reasons for this can be justified by topographical problems with the sample surface and alteration of the sample due to the actual experimental technique.

3.2.5. EPMA Experiments

EPMA instruments used in this work are typical of a standard EPMA system, using multiple components combined together to provide information from the various stimulation effects

(Fig. 32). The two instruments used in this study were a Jeol 5900 LV and a Cameca SX100, both located at the NHM, London.

The Jeol instrument was optimised for high-resolution imaging, which meant some compromises were made on quantitative elemental data quality but it was easier to acquire time on than the Cameca, so it was used primarily for identifying specimens with areas of interest that were then carried forward for analysis using the Cameca instrument. Conversely, the Cameca instrument was optimised for elemental analysis, so some compromise was made on image quality but afforded more detailed elemental composition information.

This approach made the best use of the facilities available.

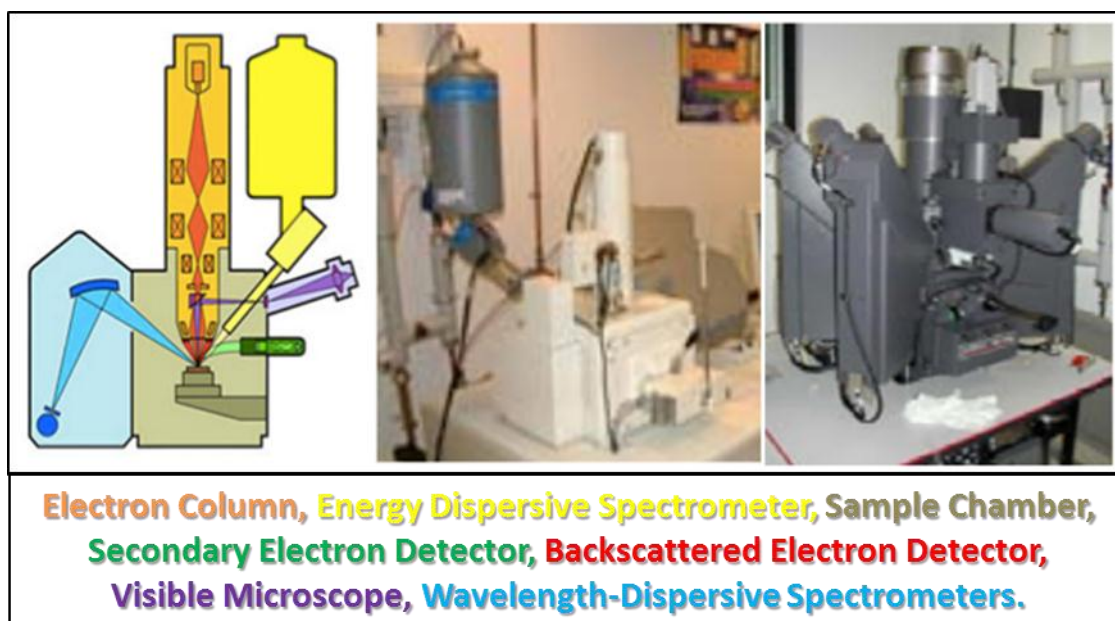


Figure 32: Left – Colour coded schematic diagram of an EPMA system;
Centre – Photograph of Jeol 5900 LV; Right – Photograph of Cameca SX100

Jeol 5900 LV

Analytical SEM instrument equipped with OXFORD WAVE quantitative EDX and WDS and a cathodoluminescence detector. Magnification 20x – 60000x ~2µm microprobe resolution takes coated polished blocks and slides with the option to work in low vacuum mode on uncoated specimens.

Samples were investigated using BSE imaging and points chosen for analysis were analysed using the energy dispersive spectrometer (EDS). Samples that were identified as having notable composition variance, especially with Ni content, were carried forward for more in depth analysis using the Cameca SX100 instrument.

Cameca SX100

Analytical SEM instrument equipped with 5 WDS and 1 Bruker EDX (SDD) detector and a cathodoluminescence detector. Takes coated polished blocks (40mmx25mm) and slides (42mmx25-50mm).

This instrument was used for both point analysis and elemental mapping of areas within the samples. Images were captured in back-scattered electron (BSE) mode and areas for analyses were selected under BSE imaging where notable variations in contrast (pertaining to differences in elemental composition) or grain shapes (indicating probable phase differences) were observed.

Elemental point analysis of selected areas was acquired using the energy dispersive spectrometer (EDS) for Mg, Al, Si, Fe, Ni and the wavelength dispersive spectrometers (WDS) for, S, Cl, K, Na, Ca, Ti, V, Cr, Mn, Co, Zn and Ba content. Oxygen was calculated stoichiometrically from the metals as oxides.

Elemental maps were acquired using EDS to map Al, Cl, Si, Mg and Ni and WDS to map Ca, Co, Cr, Fe and Na. The selected areas (c. 2500 μm^2) were mapped for approximately 6h each. Only maps where significant element abundance was observed are included in this report.

EPMA Sample Preparation

Specimens for EPMA were prepared at the NHM, London, either as polished resin blocks or, as thin sections mounted on microscope slides (Fig. 33). All specimens were carbon coated prior to analysis work.



Figure 33: Photographs of example specimens prepared for EPMA:

Left – polished resin blocks; Right – Thin section slides.

Elemental point analysis

Point analysis provides quantitative elemental information for specific points within a sample, which can be used to determine the mineral compositions present.

Investigation of the samples involved focusing the beam then “exploring” the sample using BSE imaging to find areas of interest, usually identified by differences in brightness in the BSE image that suggested compositional variation or inclusions. Once an area of interest was selected, individual points within the area were chosen for analysis. A snapshot of this image with the labelled points was taken for referral for when analysing the data acquired. This was carried out for multiple points and areas on each sample to build a reasonable representation of the sample composition and to capture as much information for the phases present as possible.

Data acquired from point analysis was generated, by the instrument, as weight% as oxides for each element at each individual point. This data was then amalgamated and analysed to identify mineral compositions present within the sample. This was done by a systematic process of tabulation, grouping and calculations, which is described in greater detail as a worked example later in this report.

Elemental mapping

Elemental maps provide predominantly qualitative information, which can be backed up by quantitative data from point analysis, but also offer extra dimensions of information not easily achievable with point analysis. EPMA elemental mapping can give a broader overall

picture of the composition of a sample and can readily identify phenomena or trends in compositional variation through a sample, which can be missed with point analysis alone.

Selection of areas for elemental mapping was done in much the same way as selecting areas of interest for point analysis. The larger the area selected, the longer the acquisition time required to produce meaningful data, so areas of approximately $2500\mu\text{m}^2$ were selected for 6h acquisition times, which gave adequate detail and made optimal use of available time on the instrument.

3.3. Vibrational Spectroscopy

Vibrational spectroscopy is a term used to classify both Infrared (IR) and Raman spectroscopy because these techniques study the vibrational (and rotational) modes of a molecule. The two techniques can be used to provide complementary information, however, there are significant differences between the two principles, which must be understood.

3.3.1. Infrared (IR) Spectroscopy

Infrared (IR) spectroscopy studies the absorption of light over the range in the electromagnetic spectrum of $10\text{-}14000\text{cm}^{-1}$. This is known as the infrared region. The infrared region can be split into 3 smaller ranges known as: near- ($14000\text{-}4000\text{cm}^{-1}$), mid- ($4000\text{-}400\text{cm}^{-1}$) and far- ($400\text{-}10\text{cm}^{-1}$) infrared.

Molecules (at standard room temperatures) are in a continuous state of vibration and each bond has characteristic vibrational frequencies. These vibrational frequencies are related to the masses of the atoms and types of bonds involved and are capable of absorbing light at these frequencies.

In an IR experiment IR radiation is passed through a sample, some frequencies are absorbed and some are transmitted. For a vibration to be IR active, a change in dipole moment must occur during the vibration, this is called a selection rule. Measuring the percentage of absorbed radiation and plotting it (either as absorbance or transmittance) against frequency (cm^{-1}), generates an IR spectrum for the sample. This spectrum displays absorption bands,

which are characteristic in their appearance and position to the distinct modes of vibration of the molecules. The modes of vibration are commonly given descriptive names such as: stretching, bending, scissoring, rocking, wagging and twisting.^{102,103}

3.3.2. Raman Spectroscopy

Raman spectroscopy is an optical technique that utilises the inelastic scattering of monochromatic light to study molecular vibrations.

When photons are passed through a material they can be scattered in two ways, either elastically or inelastically. Elastic scattering, known as Raleigh scattering, is when the incident photon is reflected back in the same direction with the same frequency and wavelength. Elastic/Raleigh scattering accounts for most of the scattering, but a small number of photons (approximately 1 in 10 million) are scattered inelastically. Inelastic scattering is known as Raman scattering and results in the scattered photon having a frequency greater than, or less than, the incident photon. Caused by an energy transfer with the photons and the interacting molecules. The outcome of Raman scattering depends on the electronic interaction that occurs. If the interacting electron is in a ground state it will be excited to a virtual energy level then, on relaxation, will move to a vibrational energy state higher than its initial value. This results in loss of energy from the incident photon and is known as Stokes Raman Scattering. Conversely, if the incident photon interacts with an electron at an already elevated vibrational state, the electron will be excited to a virtual energy level then, on relaxation, will return to the ground state. This results in a gain of energy by the incident photon and is known as anti-Stokes Raman scattering.

Like in IR spectroscopy the effects of Raman scattering are determined by the vibrations of the molecule and can similarly be used to generate a spectrum. The selection rule allowing a bond to be Raman active requires it to be anisotropically polarisable, so that the vibration mode must generate a change in polarisation.^{104,105}

3.3.3. Application of Vibrational Spectroscopy to Saprolitic Minerals

Vibrational spectroscopy is a versatile and rapid method by which to investigate these materials. Interpreting spectra of saprolitic minerals requires the positive identification of as

many characteristic vibrational bands of individual minerals as possible. Spectra can provide direct information on the structural and compositional characteristics in a relatively simple way, but are best used as a complementary method to techniques such as PXRD, where it can provide extra dimensions of information. The OH-stretching region is perhaps the most important region of the spectrum for these types of minerals, although the full spectrum is required for the best possible interpretation. Key vibrational modes relevant to this study are the structural hydroxyl stretches observed around 3600cm^{-1} ; these provide useful information about the environment around the bond. However, structural water, samples that are not properly dried and structural disorder can have a masking effect on this information by broadening absorption bands in this region, making subtle differences very difficult to accurately determine. Some of this can be combatted by using Raman spectroscopy which allows reduced vibrational bandwidths compared to IR spectroscopy (c. $<10\text{cm}^{-1}$ compared to c. $>10\text{cm}^{-1}$) however, lower intensities can be easily lost in the background noise, typical in Raman, when trying to analyse these types of fine particles. Other weaknesses are similar to those of PXRD in that minor phases and the distribution of the various constituents are very difficult to study. Historically, vibrational spectroscopy techniques have not been as widely applied to mineral sample analysis as techniques such as PXRD and thermal analysis, this is because confident interpretation can require significant skill and experience. This is especially true for complex clay-type mixtures.

3.3.4. IR Experiments

This project has used a Perkin Elmer Spectrum 100 FT-IR spectrometer with a universal attenuated total reflectance (ATR) accessory fitted. FT refers to the fact that a Fourier-transformation (a mathematical process) is used to generate the spectrum from the raw data. This allows simultaneous collection of spectral data over a wide spectral range, permitting rapid generation of a spectrum. ATR is a sampling technique that uses a property of total internal reflection through a crystal that is in contact with the sample to be analysed. This enables samples to be examined directly, with little preparation required. Spectra were recorded for 8 scans over a range selected from $300\text{-}4000\text{ cm}^{-1}$. Data were analysed using Perkin Elmer Spectrum and Microsoft Excel.

3.3.5. Raman Experiments

Raman spectra were acquired on a Horiba Jobin-Yvon LabRAM HR800 system, using a solid-state HeNe laser at 100% power, with a frequency of 632.817nm. Spectra were recorded over a range of 3600-3700cm⁻¹ for 4 accumulations, each of 120s exposure. Data were analysed using LabSpec software v5.25 and Microsoft Excel.

3.4. Thermal Analysis

Thermal analysis encompasses a range of techniques where changes in a physical property of a substance are measured as a function of temperature, whilst the substance is subjected to a controlled temperature program.

The two most commonly used thermal analysis techniques are thermogravimetric analysis (TGA), differential thermal analysis (DTA) and differential scanning calorimetry (DSC).

Thermogravimetric analysis (TGA) is used to measure the change in mass of a sample as a function of temperature. These parameters are plotted against each other to provide a thermogravimetric curve. This can be used to study factors such as moisture contents and decomposition steps. Differential thermal analysis (DTA) and differential scanning calorimetry (DSC) are used to study endothermic and exothermic changes of a sample as a function of temperature. In DTA this is done, by measuring the temperature difference between a sample and an inert standard (e.g. Alumina) as they are heated or cooled simultaneously. These temperature differences are plotted against time to give a DTA curve. DSC uses a similar instrumental arrangement to DTA, however DSC measures the difference in power required to heat a sample, with reference to an empty sample pan. For DSC, this gives a plot of heat flow against temperature.

Since the three techniques all use similar instrumental setups, TGA and DTA/DSC experiments can be carried out simultaneously on a single instrument and although thermal analysis is a destructive technique, only a small amount of sample is required (c. 10mg) for an experiment.^{106,107,108}

3.4.1. Application of Thermal Analysis to Saprolitic Minerals

Thermal analysis is one of the oldest techniques used for characterisation of these mineral types. Thermal techniques can be used for qualitative and quantitative analysis of mineral mixtures, though the thermal variability of many of the mineral types limits it as a standalone technique. As such, thermal analysis is primarily used as a complementary technique to principal PXRD studies, where PXRD is most useful for establishing similarities between samples and in contrast thermal analysis tends to emphasize the differences. In thermal analysis, many physical chemical and structural factors contribute to the results. Consequently, relationships between the thermal properties of a mineral and any single physical or chemical property are rarely simple or straightforward. Whereas, the strengths of PXRD are derived from the absolute nature of measurements and the direct representation of structure and identity.

3.4.2. Thermal Analysis Experiments

TGA-DTA/DSC data were collected using a TA instruments SDT Q600 system. Data were collected in both N₂ and air atmospheres. Data were collected using a heating rate of 10°C.min⁻¹ over the temperature range 20-1450°C in N₂ and 80-1300°C in air. Universal Analysis 2000 v4.5a software was used to: calculate percentage weight-loss; to determine onset points for the weight-loss steps; to determine endo/exo-thermic transitions in heat-flow curves and to measure the gradient of weight-loss steps.

4. Characterisation of Natural Materials

Detailed characterization of a set of natural mineral samples sourced from Ni-laterite mine sites and from the collections at the Natural History Museum (see Fig. 36) has been carried out, using a variety of materials characterization techniques. Analysis of the natural samples has involved visible inspection of the samples, acquisition of their PXRD patterns and identification of mineral phases within the samples using the ICDD database. Further to the examination of the PXRD data, a selection of the specimens have also been analysed using other techniques including synchrotron based high-resolution PXRD, and EPMA.

4.1 PXRD Studies

Powder X-ray Diffraction (PXRD) has been the principle technique used to determine the phases present in the natural samples. As Ni^{2+} and Mg^{2+} have very similar ionic radii (69pm and 72pm respectively), there are only very subtle changes in the lattice parameters of phases within a Ni-Mg solid solution and, although Ni and Mg have different scattering factors, these subtle shifts and intensity changes are very hard to detect (see Fig. 34). This is especially true for natural materials, which are typically complex and disordered. As such, for the sake of identifying phase types present, the ICDD patterns for the Mg members of the series have been used, because the patterns in the database are generally more detailed and reliable. However, this highlights the requirement for further complementary analysis to determine the actual chemical compositions of the phases.

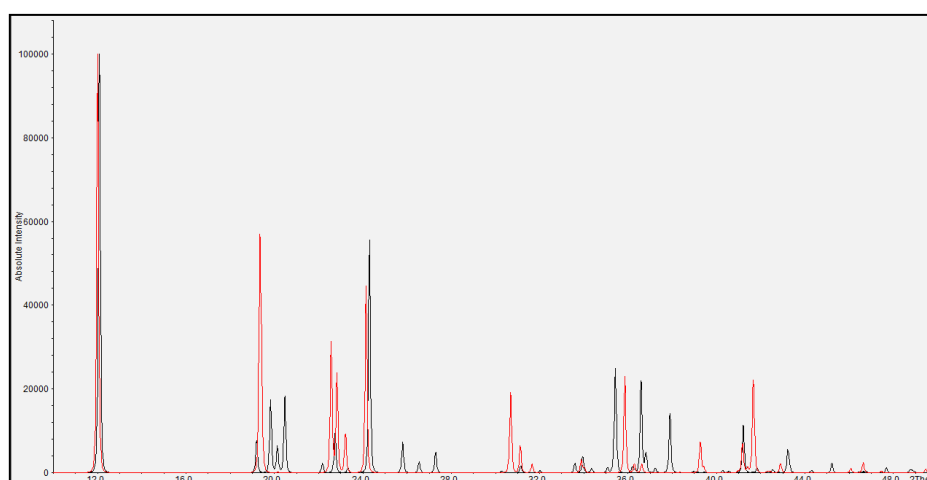


Figure 34: Comparison of theoretical XRD patterns for chrysotile ($\text{Mg}_3\text{Si}_2\text{O}_5(\text{OH})_4$) (black) and pecoraite ($\text{Ni}_3\text{Si}_2\text{O}_5(\text{OH})_4$) (red) the Ni analogue of chrysotile.

The natural mineral samples that have been investigated in this study are from the mineral collections at the Natural History Museum (NHM) and have been labelled using the codes assigned to their catalogue entries (see Table 5); the samples are from lateritic Ni-bearing silicate regions across the world. The specimens are from several different localities and vary widely in appearance as well as their mineral compositions (see Fig. 36 and Table 5).

As the samples are natural materials they exist as complex intimate mixtures of multiple mineral phases, a clear example of this is shown in the example PXRD pattern of sample B105.9.0 (Fig. 35) where 4 separate mineral phases are identified: clinocllore ($\text{Mg}_6(\text{Si,Al})_4\text{O}_{10}(\text{OH})_8$), a chlorite group mineral; talc, a talc group mineral; chrysotile (a serpentine group mineral and manganocummingtonite ($\text{Na,Ca})_2(\text{Mg,Mn,Fe})_5\text{Si}_8\text{O}_{22}(\text{OH})$ a member of the amphibole group of chain silicates.

This complexity can make definitive characterisation of these materials very difficult although several observations can be made from the PXRD data acquired from these specimens.

The PXRD data from the samples have been compared and contrasted, grouping them according to; locality, dominant mineral phases and by any trends that are apparent from these data for ease of discussion.

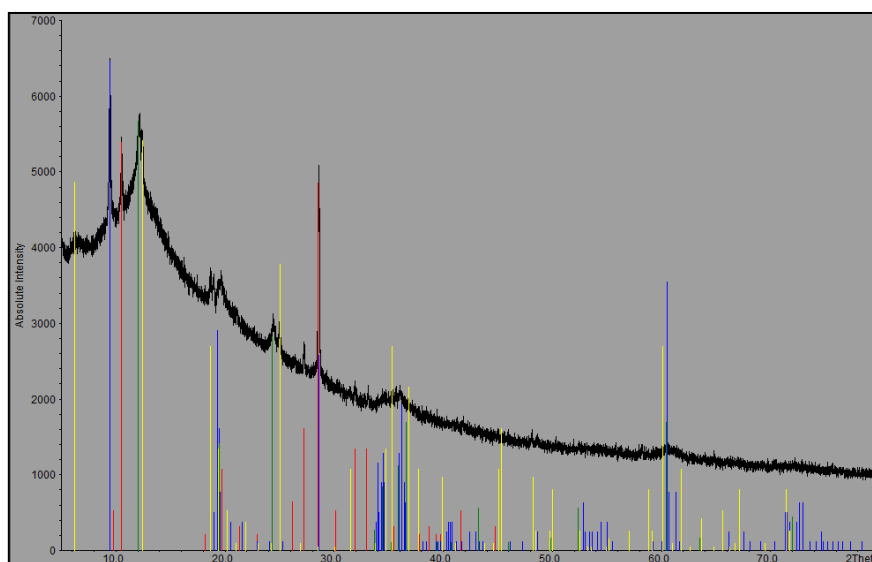


Figure 35: PXRD pattern of B105.9.0 showing ICDD patterns for; clinocllore (yellow, *46-1322*), talc (blue, *19-770*), chrysotile (green, *25-645*), manganocummingtonite (red, *23-60*) (*italics* = ICDD card numbers)

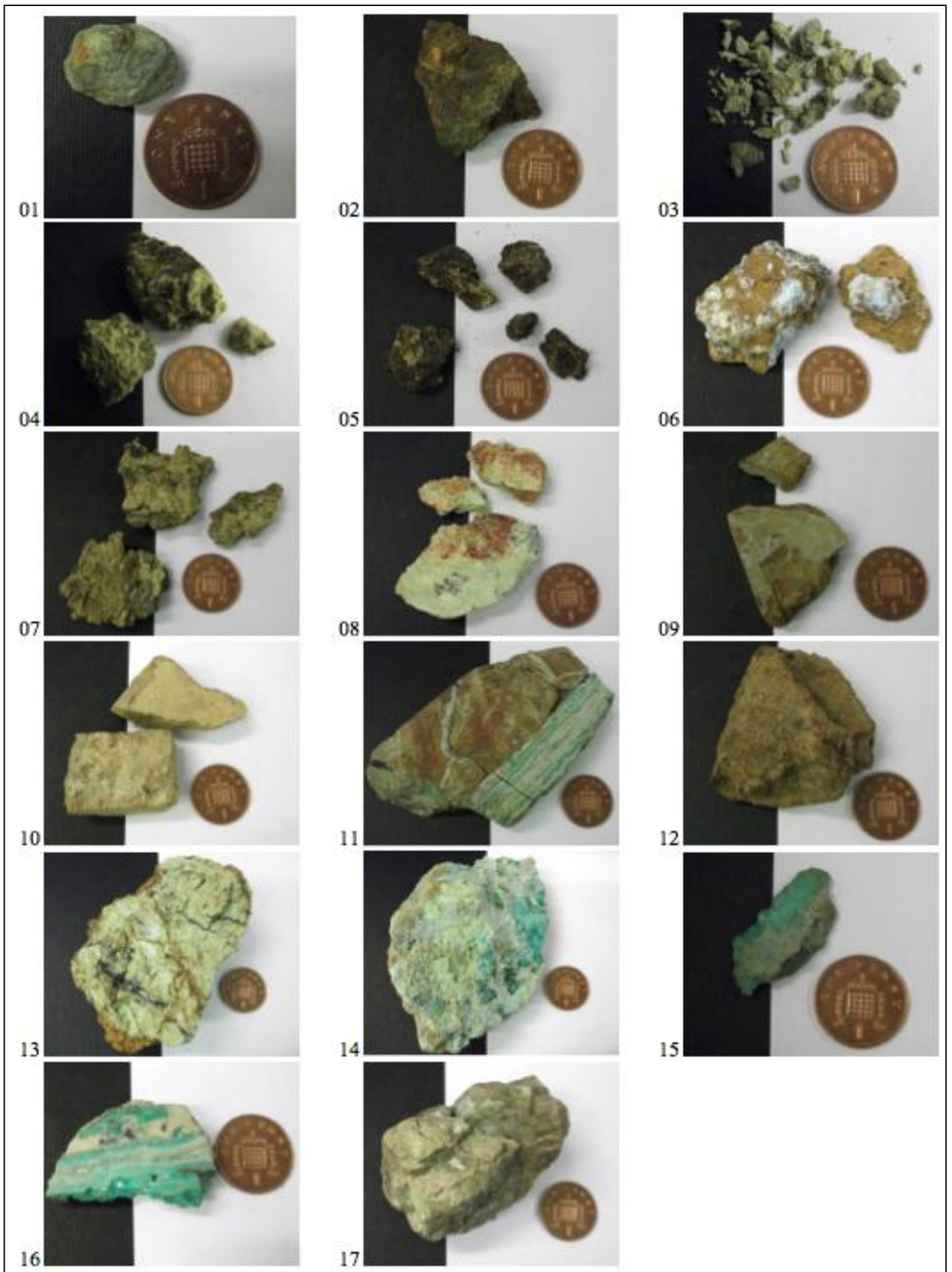


Figure 36: Photographs of natural mineral samples

Sample Name	Photo no.	Locality	PXRD Info: Instrument, 2θ range, time	Phases Identified (ICDD card no.)	Dominant phase grouping*	Unassigned reflections Å (°2θ)
09NIC050501	1	Turkey	High-res PXRD 0.935-151.740° 30 min	(43-310) Ni, Al, Si hydroxide hydrate (Ni,Al) ₇ (Al ₂ Si) ₄ O ₁₀ (OH) ₂ ·4(H ₂ O)	C	
09NIC060503A	2	Turkey	Bruker, 5-60, 2h	(25-645) Chrysotile- Mg ₃ Si ₂ O ₅ (OH) ₄	S	2.69(33.2) 4.18 (21.19)
				(19-770) Talc- Mg ₃ Si ₄ O ₁₀ (OH) ₂		
				(46-1045) Quartz- SiO ₂		
09NIC080502A	3	Turkey	Bruker, 5-80, 4h	(25-645) Chrysotile- Mg ₃ Si ₂ O ₅ (OH) ₄	Sm	
				(29-1497) Nontronite- Na _{0.3} (Fe ³⁺) ₂ (Si,Al) ₄ O ₁₀ (OH) ₂ ·nH ₂ O		
09NIC110509	4	Turkey	Bruker, 5-60°, 2h	(7-417) Antigorite- Mg ₃ Si ₂ O ₅ (OH) ₄	S	
				(29-1497) Nontronite- Na _{0.3} (Fe ³⁺) ₂ (Si,Al) ₄ O ₁₀ (OH) ₂ ·nH ₂ O		
09NIC110510	5	Turkey	Bruker, 5-60°, 2h	(52-1572) Antigorite- Mg ₃ Si ₂ O ₅ (OH) ₄	S	
				(52-1044) Chlorite-serpentine		
09NIC110512	6	Turkey	Bruker, 5-60°, 2h	(76-1782) Gibbsite - Al(OH) ₃	T	3.95(22.45)
				(83-2247) Ktenasite - (Cu,Zn) ₄ (SO ₄) ₂ (OH) ₆ ·6H ₂ O		
				(19-770) Talc- Mg ₃ Si ₄ O ₁₀ (OH) ₂		
				(25-645) Chrysotile- Mg ₃ Si ₂ O ₅ (OH) ₄		
B105.9.0	7	Shevchenko Ni deposit (Kazakhstan)	Bruker, 5-100°, 12h	(23-603) Manganocummingtonite- Na(Na,Mn) ₂ (Mg ₄ Fe ³⁺) ₂ Si ₄ O ₁₂ (OH) ₂	T	
				(19-770) Talc- Mg ₃ Si ₄ O ₁₀ (OH) ₂		
				(25-645) Chrysotile- Mg ₃ Si ₂ O ₅ (OH) ₄		
				(46-1322) Clinocllore - Mg ₆ (Si,Al) ₄ O ₁₀ (OH) ₂		
B122. 21.2	8	Shevchenko Ni deposit (Kazakhstan)	Nonius, 120°, 30 min	(25-645) Chrysotile- Mg ₃ Si ₂ O ₅ (OH) ₄	C	1.35(69.4)
				(46-1322) Clinocllore- Mg ₆ (Si,Al) ₄ O ₁₀ (OH) ₂		
				(19-770) Talc- Mg ₃ Si ₄ O ₁₀ (OH) ₂		
CM048B.97	9	Cerro Matoso (Columbia)	Bruker, 5-60°, 4h	(19-770) Talc- Mg ₃ Si ₄ O ₁₀ (OH) ₂	T	2.78(32.08)
				(25-645) Chrysotile- Mg ₃ Si ₂ O ₅ (OH) ₄		
				(46-1045) Quartz- SiO ₂		

Table 5: Characterisation Table of Results (part 1/2)

Sample Name	Photo no.	Locality	PXRD info: Instrument, 2θ range, time	Phases identified (ICDD card no.)	Dominant phase grouping*	Unassigned reflections Å(2θ)
CM050.97	10	Cerro Matoso (Columbia)	Bruker, 5-60°, 2h	(19-770) Talc- $Mg_3Si_4O_{10}(OH)_2$ (25-645) Chrysotile- $Mg_3Si_2O_5(OH)_4$ (46-1045) Quartz- SiO_2	T/S	8.4(10.53) 2.78(32.17)
CM053.97 (Brown)	11	Cerro Matoso (Columbia)	Bruker, 5-60°, 2h	(46-1045) Quartz- SiO_2 (25-645) Chrysotile- $Mg_3Si_2O_5(OH)_4$	S	
CM053.97 (Green)	11	Cerro Matoso (Columbia)	Bruker, 5-60°, 2h	(46-1045) Quartz- SiO_2 (25-645) Chrysotile- $Mg_3Si_2O_5(OH)_4$ (19-770) Talc- $Mg_3Si_4O_{10}(OH)_2$	S/T	
CM060.97	12	Cerro Matoso (Columbia)	Bruker, 5-60°, 2h	(46-1045) Quartz- SiO_2 (25-645) Chrysotile- $Mg_3Si_2O_5(OH)_4$	S	
CN-05	13	Turkey	Bruker, 5-60°, 2h	(25-645) Chrysotile- $Mg_3Si_2O_5(OH)_4$ (19-770) Talc- $Mg_3Si_4O_{10}(OH)_2$ (29-1499) Montmorillonite – $(Na,Ca)_{0.3}(Al,Mg)_2Si_4O_{10}(OH)_2 \cdot nH_2O$	S	
Lipovka [52]	14	Lipovka (Russia)	Bruker 5-60° 2h	(19-770) Talc- $Mg_3Si_4O_{10}(OH)_2$ (25-645) Chrysotile- $Mg_3Si_2O_5(OH)_4$ (46-1045) Quartz – SiO_2	S	3.34(26.63)
M14707	15	Serov (Russia)	Bruker 5-60° 2h	(25-645) Chrysotile- $Mg_3Si_2O_5(OH)_4$ (29-1433) Falcondoite- $Ni_4Si_6O_{11}(OH)_3 \cdot 6H_2O$	S	5.07(17.47) 4.03(22.02)
OR.467	16	Cerro Matoso (Columbia)	Bruker 5-60° 12h	(46-1045) Quartz- SiO_2 (19-770) Talc- $Mg_3Si_4O_{10}(OH)_2$ (25-645) Chrysotile- $Mg_3Si_2O_5(OH)_4$	T	
Pimelite.Bohemia.860	17	Czech Republic	Nonius 120° 30 min	(43-310) Ni, Al, Si hydroxide hydrate $[(Ni,Al)_3(Al,Si)_4O_{10}(OH)_3 \cdot 4(H_2O)]$ (46-1322) Clinocllore- $Mg_4(Si,Al)_4O_{10}(OH)_8$	C	

Table 5: Characterisation Table of Results (part 2/2)

*Dominant Phase Groupings:

S = serpentine $M_3Si_2O_5(OH)_4$, T = talc $M_3Si_4O_{10}(OH)_2$, C = chlorite $M_6(Si,Al)_4O_{10}(OH)_8$,

Sm = smectite $(Ca,Na)_{0.3}M_{2-3}(Si,Al)_4O_{10}(OH)_2 \cdot nH$

4.1.1 Samples from Turkey

Although all of the samples from Turkey (Fig. 36 images 1-6 and 13) are from the same locality and look relatively similar (green/brown friable masses, with the exception of 09NIC110512, image 6) the PXRD patterns show that there is a wide variation in mineral composition and differences in crystallinity between the specimens (see Fig. 37). Serpentine type phases are identified in 4 of the 6 specimens from Turkey but crystallinity of these serpentine phases varies dramatically; for example the PXRD pattern of sample 09NIC060503A (2) shows a relatively ordered crystalline phase; indicated by clear, sharp reflections at d-spacings around 7.3Å (12°2θ) and 3.65Å (24°2θ) (corresponding to the 001 and 002 reflections of a serpentine type phase respectively). Whereas, in the PXRD for sample 09NIC110510 (5) serpentine is only identified by a very broad bump at around 7.3Å. Other relevant phases identified include talc, clinocllore (a chlorite type phase) and nontronite (a smectite type mineral). The relative difference in background between each of the patterns is also quite clear. Sample 09NIC050501 (1) shows a very low background; this increases the signal to noise ratio at lower intensities and may hide reflections from other phases at lower intensities. The strongly reflecting crystalline phase is identified as a chlorite type phase but exhibits a very regular repeating pattern of reflections between 6.1-6.3°2θ. This phenomenon is likely to be due to preferred orientation resulting from the plate-like crystals, causing alteration of the expected relative intensities of the pattern. The specimen 09NIC110512 (Fig 36, image 6) is somewhat different in appearance to all of the other specimens that have been analysed since it clearly contains some blue coloured material. This can possibly be explained by identification of the Cu containing mineral phase Ktenasite ((Cu,Zn)₅(SO₄)₂(OH)₆.6H₂O) in the phase which is hydrated Cu-Zn sulphate.

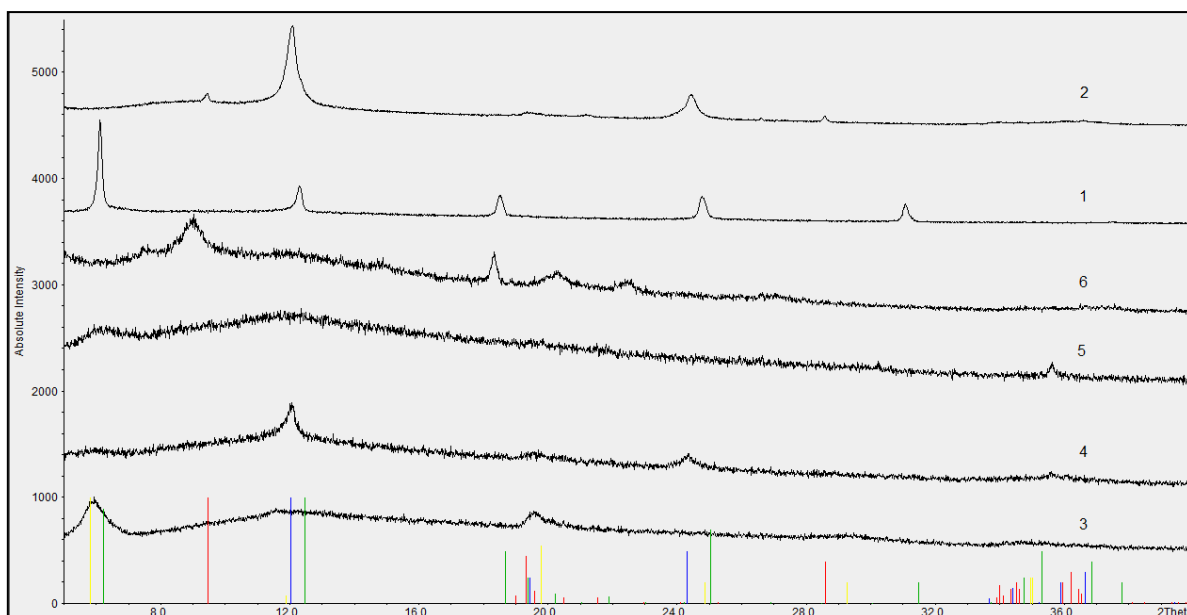


Figure 37: Turkey set. ICDD data for talc (red, 19-770); clinocllore (green, 46-1322); chrysotile (blue, 25-645); nontronite (yellow, 29-1497), 3) 09NIC080502A; 4) 09NIC110509; 5) 09NIC110510; 6) 09NIC110512; 1) 09NIC050501; 2) 09NIC060503A

4.1.2. Samples from Cerro Matoso (Columbia)

In comparison to the set of natural specimens from Turkey there is a larger variation in the appearance the specimens from Columbian Cerro Matoso (Fig. 36, images 9, 10, 11, 12, 16) and the materials are generally harder, with light coloured quartz type material visible in 3 of the 5 samples. Quartz is observed in the PXRD patterns of all of the Cerro Matoso specimens (Fig. 38) and may explain the hardness of the materials. The strong sharp major quartz reflections are clearly visible in the PXRD patterns at around 3.34\AA ($26.64^\circ 2\theta$) and 4.25\AA ($20.86^\circ 2\theta$). The pronounced quartz reflections make detection of other phases more difficult but serpentine and talc are also identified in these materials. Serpentine and talc occur in varying ratios but overall talc is the most dominant phase after quartz; although it is generally poorly crystalline. Comparison of the PXRD patterns shows that CM048B.97 (9), CM053.97 green (11) and OR.467 (16) have very similar patterns which correlate to the similarities in their appearance where all have some green phase separated by quartz-like veins (Fig. 36, images 9, 11 & 16). The PXRD patterns suggest that these green phases are some disordered form of talc, although further analysis is required to fully characterise these materials.

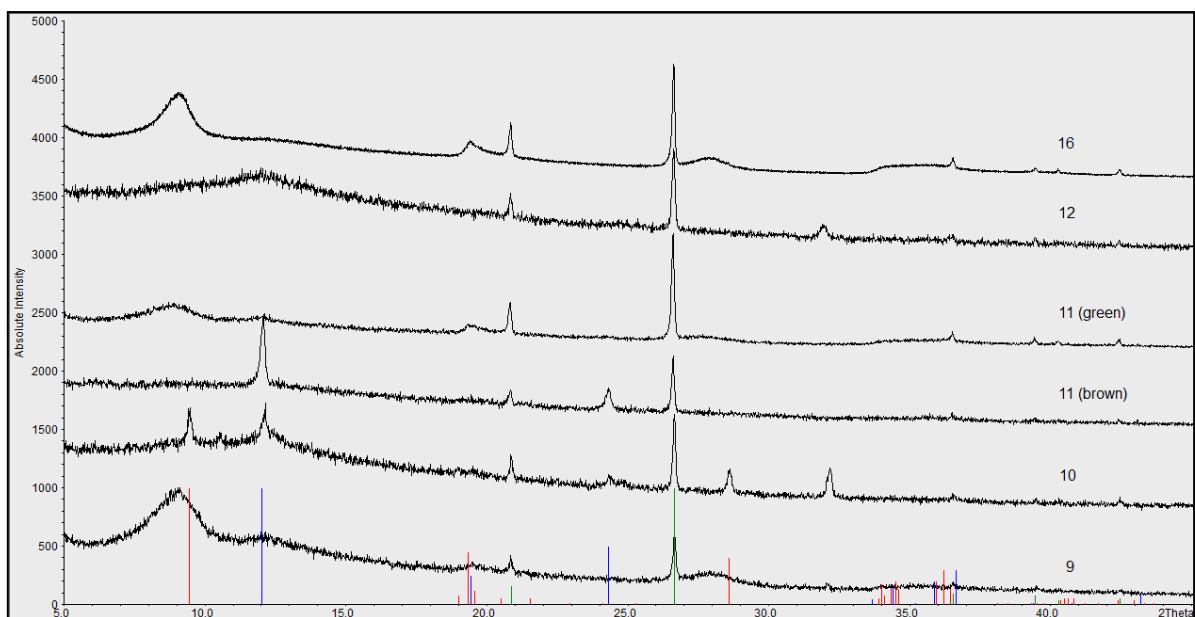


Figure 38: Cerro Matoso set. ICDD data for talc (red, 19-770); chrysotile (blue, 25-645); quartz (green, 46-1045); 9) CM048B.97; 10) CM050.97; 11) CM053.97 brown; 11) CM053.97 green; 12) CM060.97; 16) OR.467

4.1.3. Serpentine

Of the 17 specimens that have been analysed 15 are found to have serpentine phases present in varying amounts in their PXRD patterns and for 10 of these, serpentine is the most dominant phase that is identified (Fig. 39). This clearly shows serpentines are very significant phases within these types of material. Whilst the ICDD data for chrysotile (card no. 25-645) seems to be the best match to several of the identified serpentine phases it is difficult to be certain about this observation as the subtle differences between the patterns for the different polymorphs of the serpentine group (lizardite, chrysotile and antigorite)(Fig. 40) are difficult to detect in such complex PXRD patterns. However, it is clear that serpentines occur in these materials in both ordered and disordered forms with 09NIC060503A (2), 09NIC110509 (4), CM050.97 (10) and CM053.97 brown (11) showing more ordered serpentine crystalline structures than the others.

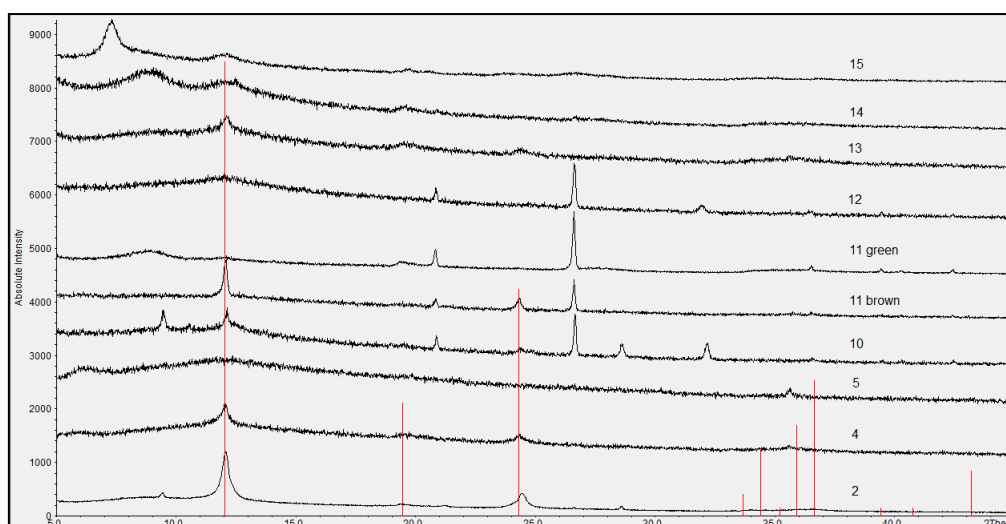


Figure 39: PXRD of serpentine dominated specimens. ICDD data for chrysotile (red, 25-645); 2) 09NIC060503A; 4) 09NIC110509; 5) 09NIC110510; 10) CM050.97; 11 brown) CM053.97 brown; 11 green) CM053.97 green; 12) CM060.97; 13) CN-05; 14) Lipovka[52]; 15) M14707x5428x5432

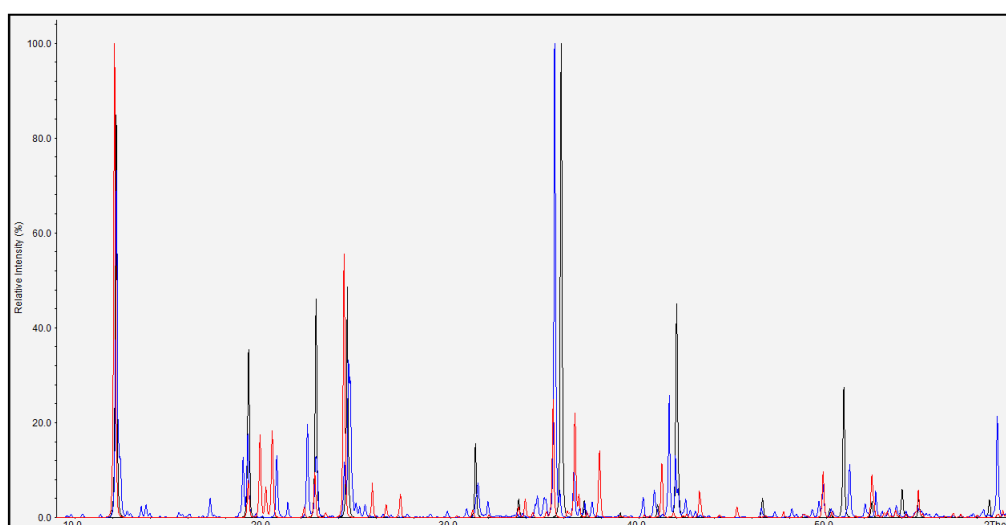


Figure 40: Comparison of theoretical patterns for the serpentine polymorphs: lizardite (black); chrysotile (red); antigorite (blue)

4.1.4. Talc

Talc type phases are identified in 10 of the 17 specimens, making them the second most common mineral phase in this collection, in 6 of these specimens talc is identified as being the dominant phase (Fig. 41). As observed with the serpentine set, the talc phases also show a large variation in crystallinity between the samples. The well ordered talc phases (Fig. 42)

show good correlation with ICDD data for talc, with sharp reflections observed at around 9.35Å (9.45°2θ) and 3.12Å (28.6°2θ) corresponding to the 002 and 006 reflections of talc. However, the broader disordered phases identified as talc show distortion and shifting of the reflections (Fig. 43). This distortion may be explained by alteration of the lattice parameters. The shift to higher d-spacings (to the left) that is observed for the 002 and 006 reflections indicates increased basal spacing and the shift to lower d-spacings (to the right) observed for the 020, -111 cluster suggests decreased lattice parameters in the plane of the layers. This can possibly be explained by divergence from the ideal talc formula ($\text{Mg}_3\text{Si}_4\text{O}_{10}(\text{OH})_2$); the substitution of other elements into the structure (e.g. Ni) would cause alteration of the dimensions of the sheets and if a charge imbalance is created in the sheets some water or other interlayer species may be present causing an increase in the layer spacing. Further analysis is required to verify these possibilities.

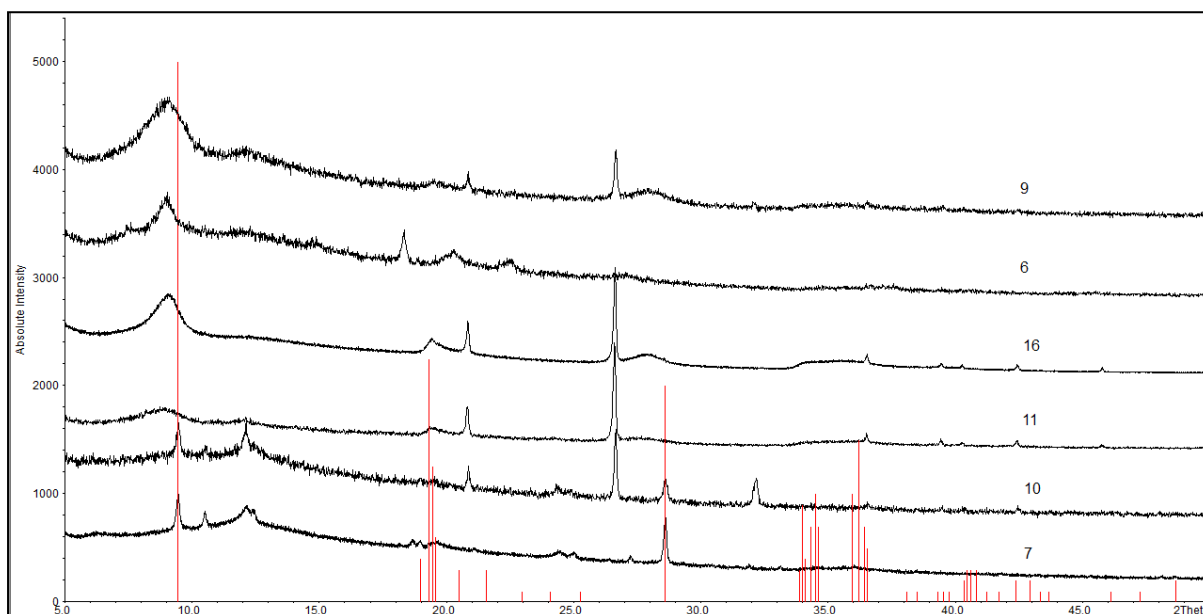


Figure 41: Talc dominated set. ICDD data for talc (red, 19-770); 7) B105.9.0; 10) CM050.97; 11) CM053.97 green; 16) OR.467; 6) 09NIC110512; 9) CM048B.97

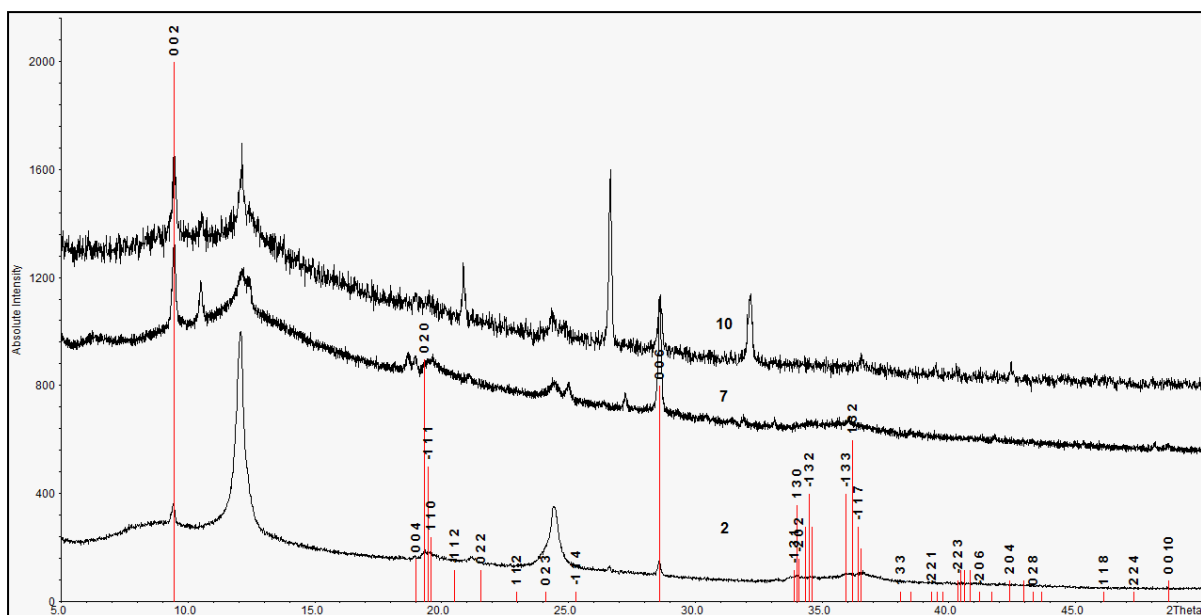


Figure 42: Ordered crystalline talc set. ICDD data for Talc (red, 19-770); 2) 09NIC060503A; 7) B105.9.0; 10) CM050.97

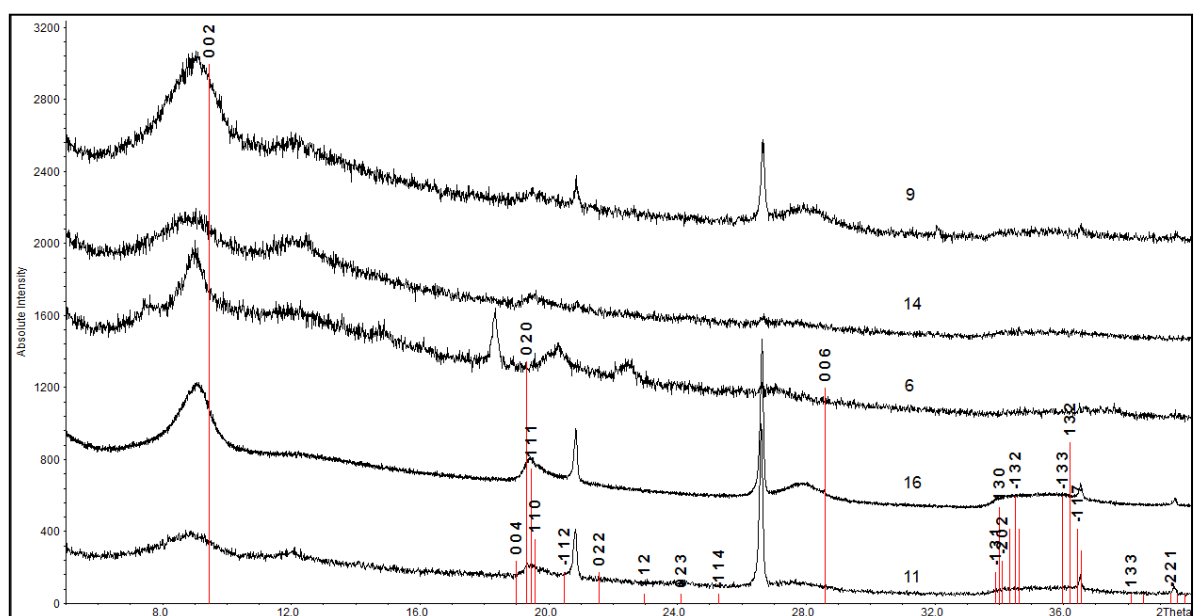


Figure 43: Distorted Talc set. ICDD data for talc (red, 19-770); 11) CM053.97 green; 16) OR.467; 6) 09NIC110512; 14) Lipovka[52]; 9) CM048B.97

4.1.5. Chlorites

Chlorite type phases (clinochlore, 46-1322) have been identified in 5 of the 17 specimens; in 3 of these occurrences chlorite is observed to be the dominant phase present (Fig. 44). Relative to the talc and serpentine type phases that have been identified from these materials,

the chlorite type phases tend to have more ordered crystalline structure. This is shown by intense sharp reflections in the PXRD patterns that match well with the ICDD data.

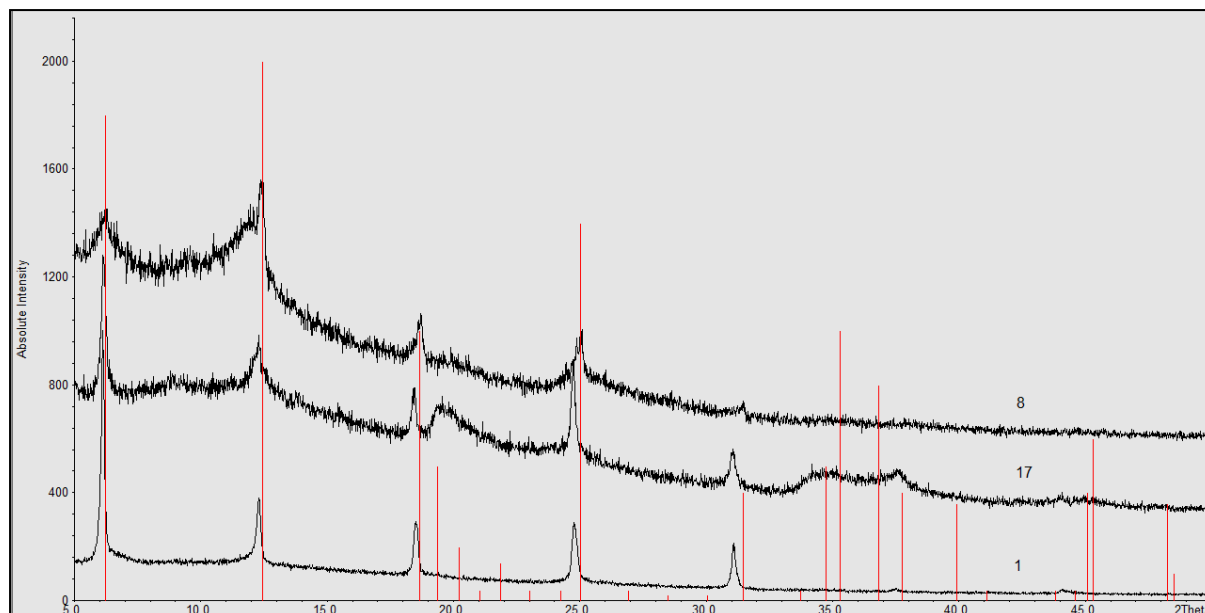


Figure 44: Chlorite dominated set. ICDD data for clinochlore (red, 46-1322); 1) 09NIC050501; 17) Pimelite.Bohemia.860; 8) B122.21.2

4.1.6. Smectites

The typically disordered nature of smectite type minerals along with their variable basal spacings and preferred orientation effects (sensitive to exchangeable cation and relative humidity) make these mineral phases very difficult to characterise from the PXRD patterns of natural materials. High background levels easily mask the characteristic diffuse reflections and the variable basal spacings make matching these phases to ICDD data very difficult. Smectite phases are likely in these types of materials and several of the specimens show reflections that may be from smectite contributions i.e. broad asymmetrical reflections at high d-spacings. However, only 3 specimens show reflections that can be matched closely to ICDD data (Fig. 45) and only 09NIC080502A (3) can be classified as a smectite dominated sample; with correlation to the ICDD data for nontronite ($\text{Na}_{0.3}(\text{Fe}^{3+})_2(\text{Si},\text{Al})_4\text{O}_{10}(\text{OH})_2 \cdot n\text{H}_2\text{O}$). Sample 09NIC110509 (4) (from the same locality as 09NIC080502A (3)) exhibits nontronite reflections but at much lower intensities than 09NIC080502A (3). The third identified smectite containing specimen is CN-05, this shows

possible montmorillonite $((\text{Na,Ca})_{0.3}(\text{Al,Mg})_2\text{Si}_4\text{O}_{10}(\text{OH})_2n\text{H}_2\text{O})$ contributions but again the reflections are very diffuse.

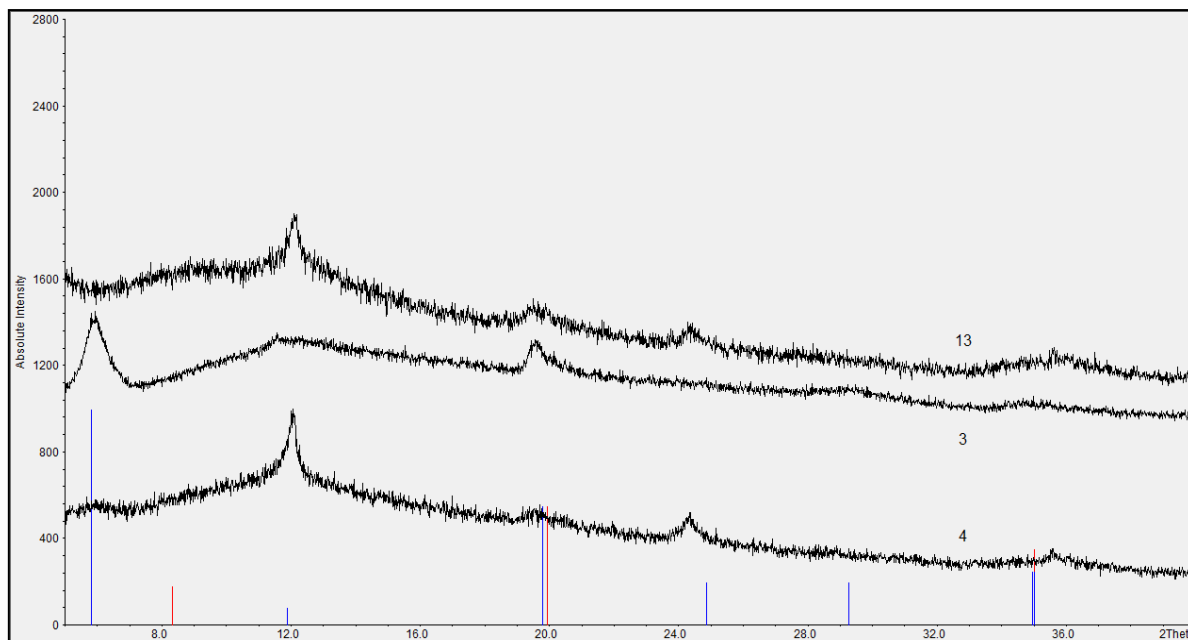


Figure 45: Smectite dominated set. ICDD data for nontronite (blue, 29-1497); montmorillonite (red, 29-1499); 4) 09NIC110509; 3) 09NIC080502A; 13) CN-05

4.1.7. PXRD Conclusions

The PXRD studies of these natural specimens show that the materials are typically complex and disordered, and whilst this highlights the limitations of PXRD as a characterisation technique on its own (e.g. the restriction of phase identification to the broad term of phase type rather than specific minerals), some useful observations have been made from the PXRD data; serpentine, talc, chlorite and smectite phases have all been identified and although quartz has been a commonly identified phase in these samples no other phases have shown recurrence. The most significant observation from the PXRD study though has been the identification of serpentine and talc as the most prominent phase types in these materials, irrespective of locality.

4.2. Synchrotron based High-Resolution PXRD

Following from the standard PXRD studies, synchrotron based high-resolution PXRD was used to collect data for the specimen 09NIC050501 (Fig. 46), to reduce the preferred orientation effects observed in the data from the standard method. The data collected using synchrotron radiation shows much more information about the crystalline structure than the data collected on the Bruker D8 instrument. However, some preferred orientation is still observed, with the most intense reflection at around 14.369\AA having an absolute intensity of over ten times the next most intense reflection at 2.395\AA . This is quite unusual considering that the sample was recorded using a capillary which normally removes preferred orientation effects and may suggest the crystals have a needle shaped morphology. Nevertheless, the acquired pattern does indicate a better correlation with a vermiculite ($(\text{Mg},\text{Fe}^{2+},\text{Al})_3(\text{Al},\text{Si})_4\text{O}_{10}(\text{OH})_2 \cdot 4(\text{H}_2\text{O})$) type phase rather than the chlorite type phase which appeared to be the best fit to the data collected on the Bruker D8 pattern. The best match to the ICDD database was afforded to the pattern for the synthetic Ni-substituted vermiculite (nickel aluminium hydroxide hydrate, ICDD card 43-310). Vermiculite is a phyllosilicate from the mica group and a realistic phase in these types of materials, although there are no known natural Ni-bearing analogues. These results show the enhanced resolving power of synchrotron high-resolution PXRD for these complex materials, although accessibility seriously restricts the use of this technique.

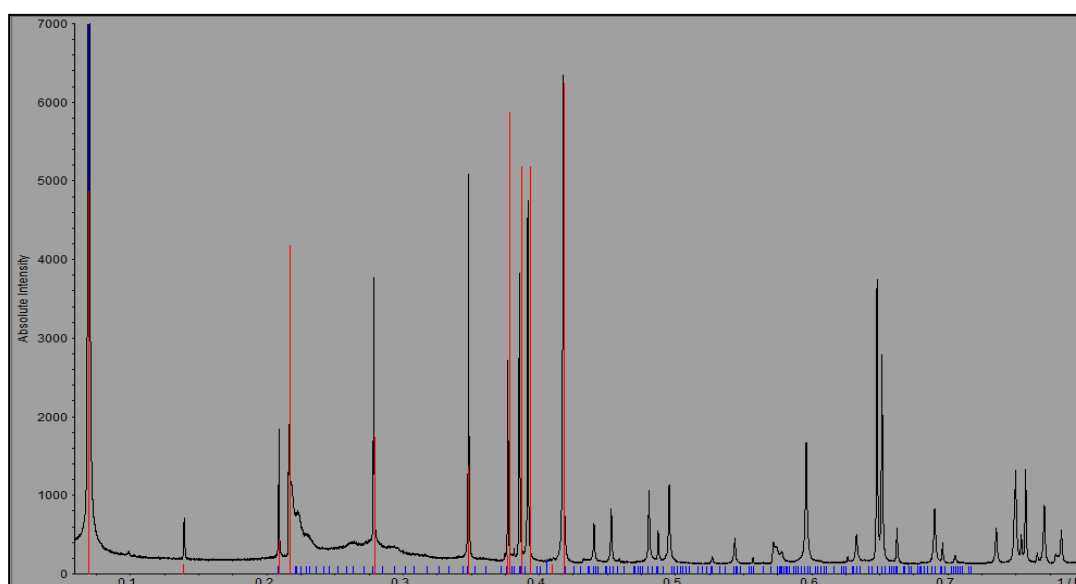


Figure 46: Expanded section from Synchrotron high-res PXRD pattern of 09NIC050501 showing similarity with vermiculite (blue) and nickel aluminium silicate hydroxide hydrate (red) from ICDD.

4.3. EPMA Studies

Subsequent to the initial PXRD studies, a selection of the natural specimens were analysed further using EPMA as a complementary technique. Samples were chosen on the basis of determination of relevant phase presence from PXRD patterns (e.g. talc and serpentine; which have been identified as most relevant to this study) and also unusual phases such as falcondoite (see M14707). Physical characteristics of samples, such as visible zoning of materials also influenced selection. These samples and their reasons for selection are:

- M14707: because of an identified presence of the unusual phase falcondoite ($\text{Ni}_4\text{Si}_6\text{O}_{15}(\text{OH})_2$)
- CM048B.97, CM053.97 and OR.467: talc and serpentine phases are clearly identified from PXRD; they are from the same locality (Cerro Matoso) and are also comparable in appearance with green colouration and clear zoning of materials.
- B105.9.0 and B122.21.2: both from Shevchenko Ni deposit (Kazakhstan) and have similar mineral compositions (talc, serpentine and chlorite) although quite different appearance.
- Pimelite Bohemia.860 and 09NIC050501: Both specimens have been identified as unusual, well crystalline, layered materials, not known as natural Ni-bearing phases.

4.3.1. M14707 (worked example)

Sample M14707 is from the saprolitic (Si-rich) region of a Ni-laterite mine site in Serov (Russia). The sample is hard and vivid green (see Fig. 47), characteristic of a siliceous nickeliferous material. From the PXRD pattern acquired for this sample 2 phases are identified, a serpentine-type phase ($\text{Mg}_3\text{Si}_2\text{O}_5(\text{OH})_4$) and a falcondoite-type phase ($\text{Ni}_4\text{Si}_6\text{O}_{15}(\text{OH})_2$) (see Fig. 48), both of which are known to occur in laterite materials. EPMA analysis of this material was performed to further characterize the sample.



Figure 47: Photograph of sample M14707

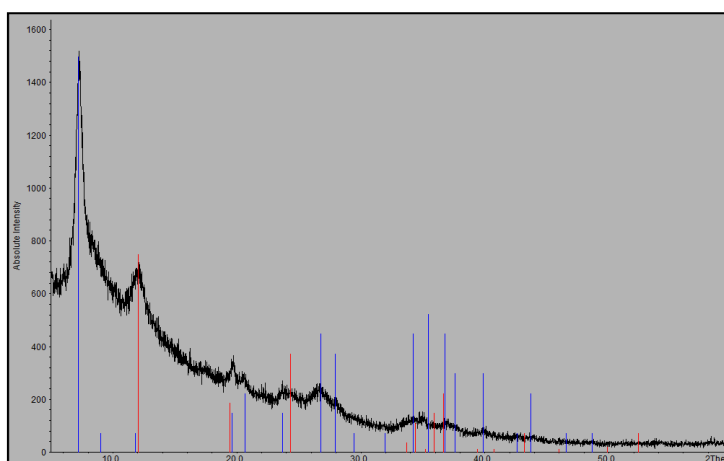


Figure 48: Sample M14707; PXRD pattern showing serpentine (red, chrysotile from ICDD card no. 25,645) and falcondoite (blue, ICDD card no. 29,1433) phase presence.

Analysis of the sample using BSE imaging shows it consists of two clear zones; a bright edge that varies in thickness around the sample and a darker core zone (see Fig. 49), this observation indicates a difference in elemental composition (the brighter area having a higher relative mass). The sites for investigation were therefore chosen to investigate these characteristics further. Point analyses were acquired for 3 different areas, with one used to record elemental maps.

Point Analysis

From the 3 areas elemental data (for: Na, Mg, Al, Si, S, Cl, K, Ca, Ti, V, Cr, Mn, Fe, Co, Ni, Zn, Ba) were acquired at 75 different points that were selected to analyse the difference in composition through the material (see Fig. 49).

Data Handling

Examination of the raw data acquired from these points involved discarding any points that returned totals lower than 70%, as, although totals lower than 100% are expected for hydrous-silicate materials anything less than 70% indicates a problem with the measurement. For example, the analysis volume may have fallen on an edge or grain boundary, the surface may not be smooth or the beam may have been poorly focused. With these data removed (for this sample there were 4 such points to discard) the general composition of the points were assessed and the data set reduced to incorporate only the elements which contributed at least 0.1% of the oxide total. For this sample, this step reduced the data set to data for NiO, MgO, SiO₂ and FeO. The data were then tabulated in a spreadsheet to allow comparisons and trends (in the data) to be observed more easily (see table 6).

To ensure points were not missed when carrying out the above data handling procedure, a further column of the difference between the reduced total and the experimental total was created. Values in this column that are high may indicate addition of other elements needs to be considered to complete the data analysis.

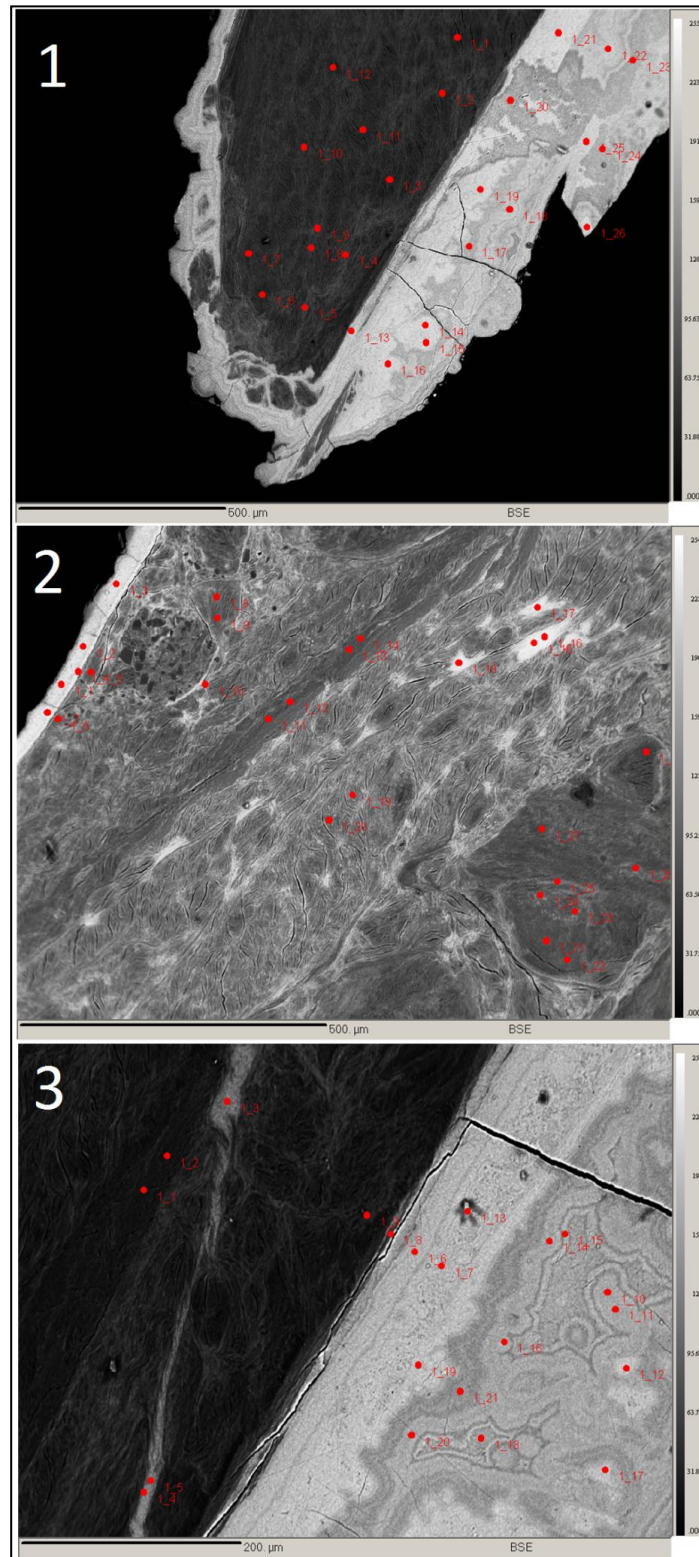


Figure 49: BSE images of sample M14707 (red spots indicate points analysed)

Area	Point	MgO	NiO	FeO	SiO ₂	Exp. Total	Red. Total	Diff Total
1	1	16.82	17.17	0.00	49.62	83.79	83.61	0.18
1	2	16.84	20.86	-0.01	56.04	93.86	93.73	0.13
1	3	19.11	17.38	0.01	56.44	93.07	92.94	0.13
1	4	16.11	23.11	0.00	56.19	95.60	95.41	0.19
1	5	16.87	21.11	0.00	56.24	94.38	94.22	0.16
1	6	18.65	17.96	-0.02	57.83	94.50	94.42	0.08
1	7	16.50	22.22	0.01	55.85	94.70	94.58	0.12
1	8	16.58	22.09	0.01	56.81	95.62	95.49	0.13
1	9	15.32	22.51	0.00	55.28	93.31	93.11	0.20
1	10	17.91	18.94	0.00	55.48	92.47	92.33	0.14
1	11	18.19	17.89	-0.01	56.38	92.53	92.45	0.08
1	12	18.37	18.55	-0.02	57.05	94.08	93.95	0.13
1	13	10.70	35.15	0.02	49.40	95.70	95.27	0.43
1	14	3.24	47.77	0.81	38.93	91.11	90.75	0.36
1	15	3.03	48.23	0.26	39.11	90.94	90.63	0.31
1	16	3.04	48.18	0.34	39.73	91.65	91.29	0.36
1	17	5.79	45.86	-0.01	40.71	92.61	92.35	0.26
1	18	4.12	47.30	0.00	39.84	91.49	91.26	0.23
1	19	3.49	48.46	0.17	39.97	92.23	92.09	0.14
1	20	5.43	43.56	0.67	43.42	93.17	93.08	0.09
1	21	3.12	48.57	0.16	40.20	92.27	92.05	0.22
1	22	6.04	44.26	0.09	42.66	93.25	93.05	0.20
1	23	4.16	45.75	0.36	43.00	93.50	93.27	0.23
1	24	4.32	44.86	0.48	42.60	92.56	92.26	0.30
1	25	3.00	47.59	0.23	42.44	93.43	93.26	0.17
1	26	4.18	38.03	0.09	34.11	77.14	76.41	0.73
2	4	4.22	41.97	0.10	42.63	89.15	88.92	0.23
2	5	3.58	43.16	0.19	41.13	88.22	88.06	0.16
2	6	4.17	42.99	0.24	42.32	89.86	89.72	0.14
2	8	14.65	24.78	0.11	54.82	94.43	94.36	0.07
2	9	15.43	23.39	0.07	54.37	93.30	93.26	0.04
2	10	21.01	21.23	1.47	48.80	92.81	92.51	0.30
2	11	15.84	20.18	0.00	55.18	91.34	91.20	0.14
2	12	16.13	21.47	0.02	56.15	93.99	93.77	0.22
2	13	17.02	20.22	-0.04	58.06	95.36	95.26	0.10
2	14	16.24	21.53	0.02	56.85	94.77	94.64	0.13
2	15	3.60	45.17	0.03	44.59	93.51	93.39	0.12
2	16	4.11	44.06	-0.01	44.84	93.04	93.00	0.04
2	17	6.94	38.59	0.00	48.35	94.01	93.88	0.13
2	18	7.21	37.48	0.05	48.03	92.91	92.77	0.14
2	19	10.93	29.38	-0.02	53.60	94.05	93.89	0.16
2	20	12.45	25.98	0.00	55.32	93.84	93.75	0.09
2	21	17.78	18.71	-0.01	56.52	93.11	93.00	0.11
2	22	17.42	20.13	0.03	57.08	94.78	94.66	0.12
2	23	16.07	23.10	0.02	56.00	95.34	95.19	0.15
2	24	14.34	24.17	0.03	54.15	92.90	92.69	0.21
2	25	15.13	23.02	0.01	54.09	92.41	92.25	0.16
2	26	14.94	23.25	0.03	53.40	91.68	91.62	0.06
2	27	17.95	18.66	0.01	56.72	93.58	93.34	0.24
2	28	17.15	20.23	0.01	56.10	93.77	93.49	0.28
3	1	16.32	20.21	-0.01	54.91	91.70	91.43	0.27
3	2	16.92	19.96	-0.03	55.19	92.15	92.04	0.11
3	3	7.91	38.51	0.00	44.35	90.79	90.77	0.02
3	4	15.02	24.22	0.00	52.10	91.51	91.34	0.17
3	5	13.73	26.99	-0.02	51.37	92.24	92.07	0.17
3	6	4.56	46.91	0.06	40.34	92.03	91.87	0.16
3	7	3.79	47.14	1.01	39.97	92.08	91.91	0.17
3	8	10.46	33.64	0.00	52.25	96.43	96.35	0.08
3	9	15.05	24.21	0.01	54.43	93.88	93.70	0.18
3	10	3.98	47.58	0.01	39.43	91.18	91.00	0.18
3	11	4.07	47.62	0.00	39.19	91.02	90.88	0.14
3	12	3.37	48.27	0.07	39.11	91.03	90.82	0.21
3	13	3.42	45.33	0.33	38.85	88.12	87.93	0.19
3	14	4.22	47.23	0.03	40.08	91.66	91.56	0.10
3	15	2.64	47.69	0.00	43.56	94.02	93.89	0.13
3	16	4.32	47.50	0.01	40.11	92.09	91.94	0.15
3	17	2.80	49.00	0.16	39.10	91.15	91.06	0.09
3	18	2.64	48.14	0.01	42.23	93.11	93.02	0.09
3	19	3.16	48.67	0.20	39.77	91.93	91.80	0.13
3	20	4.74	46.92	0.01	40.38	92.18	92.05	0.13
3	21	5.89	45.45	0.02	40.51	92.00	91.87	0.13

Table 6: Reduced raw data set of wt.% oxides from point analysis for sample M14707. Bright “edge” points = highlighted in green. Red text = discarded data

Where it was possible to do so, the data are then split on the basis of appearance in the BSE image; this can give a reasonable indication of different phases by variation in contrast. For this sample simply separating the data into “bright edge” points and “dark core” points was readily achievable (see Table 6 and Fig. 49). In other samples, determination of similar phases simply by appearance was not practical as BSE imaging contrast is sometimes only very subtly different between phases. This was often identified by large standard deviation of grouped data sets.

Manipulation of the data can then be performed to highlight abnormal inclusions as well as further trends or patterns, for example sorting them by SiO₂ content makes identification of quartz or chalcedony straightforward i.e. >95% SiO₂. More subtle differences can also be indicative of multiple phase presence, for example close inspection of a group of points sorted by weight% oxide may show gaps in the series of data (>1% between 2 points) which can indicate phase separation, a difference that may not be immediately noticeable from the BSE image.

When the data were separated into these groups related by some factor (with acceptable standard deviation between the points, generally targeted around $\pm 10\%$ for the major elements) it was often possible to highlight data that could be discarded for justifiable reasons, such as if the point is noticeably close to an edge or boundary. This then reduces the standard deviation of the set (see the 8 “discarded data” in Table 6 and their locations on the related BSE images Fig. 49).

Formula Extraction

		MgO	NiO	FeO	SiO₂	Exp. Total	Red. Total	Diff Total
Overall Av.		10.20	33.77	0.11	48.19	92.44	92.27	0.17
Overall Sd.		6.21	12.25	0.25	7.28	2.69	2.74	0.10
N = 71								
Edge Av.		3.96	47.14	0.21	40.66	92.15	91.96	0.19
Edge Sd.		1.02	1.42	0.27	1.49	0.88	0.90	0.08
N = 25								
Core Av.		14.94	24.25	0.05	54.08	93.46	93.31	0.14
Core Sd.		4.03	7.10	0.24	3.69	1.23	1.23	0.06
N = 38								

Table 7: Tables of average wt.% oxides and standard deviations for data sets for M14707
Av. = average. Sd. = standard deviation. N= number of points.

Averages from these assembled groups (see table 7) are assumed to be a reasonable representation of a single mineral phase present in the sample. This sample shows there is still a significant standard deviation with respect to MgO and NiO average wt.% in the edge and core groupings, although both were significantly reduced from the overall averages. The reasoning for this variation is discussed later in this chapter. Using the wt.% oxide data it is possible to get some idea which mineral species is being observed. The PXRD data indicate a serpentine-type and a falcondoite-type phase are present in this sample and the average SiO₂% from the “edge” group and the “core” group of points are 40.66% and 54.08% respectively. Given that the ideal expected SiO₂% for a Ni-bearing serpentine-type and falcondoite-type mineral would fall in the 34.9-49.8% or 54.68-69.10% range respectively it would suggest the “edge” is made up of a serpentine-type mineral and the “core” of a falcondoite-type mineral.

Calculations Explained

Although some conclusions may be drawn purely from the data averages, some relatively simple calculations can give a better indication of the general formula for the observed mineral phase and its fit to a certain mineral type³⁴. These calculations are summarized in Table 8 and each row can be explained thus:

A gives the average wt.% oxides from the relevant data set, expressing the composition.

B is calculated by dividing each average wt.% oxide figure (A) by its respective formula weight (given at the top of Table 8), therefore expressing the molar proportions of each oxide.

C is calculated from B by multiplying by the number of oxygen atoms per cation in the oxide concerned, (e.g. for SiO₂ B is multiplied by 2 and for Al₂O₃ B would be multiplied by 1.5), to give values that are proportional to the number of associated oxygen atoms.

C values are summed ($\sum C$) and the number of oxygen atoms (O_n) is assumed from the expected mineral formula; e.g. for calculation as a serpentine mineral (Mg₃Si₂O₅(OH)₄) $O_n=7$, because H₂O is not measured giving 2SiO₂ and 3MgO as the only observable parts of the mineral.

$D = C \times (O_n / \sum C)$; to give the number of oxygen anions on the basis of the expected formula.

E gives the number of each cation in the formula from D divided by the number of cation atoms per oxygen atom in the oxide concerned (e.g. for SiO_2 B is multiplied by 0.5 and for Al_2O_3 B would be multiplied by 0.66).

F = Tetrahedral : Octahedral cation ratio (O:T) calculated from row E. This is done by totalling the figures from row B that correspond to octahedral cations e.g. Ni^{2+} , Mg^{2+} , Fe^{2+} etc. and the figures that correspond to tetrahedral cations e.g. Si^{4+} . This ratio can then be compared to the expected ratio from the formula on which O_n was based (e.g. serpentine = 3:2) to ascertain if the values fall within an acceptable range.

Also, for the calculation of ratios where Al is present within a mineral that is assumed to be a phyllosilicate-type phase (e.g. serpentine, talc, chlorite etc.), half of the ions are assumed to be tetrahedral and half to be octahedral to satisfy the interlayer charge balance.

G = approximate mineral formula from normalized data based on the assumed ideal formula.

		MgO	NiO	FeO	SiO₂		
	Oxide Formula Weight (F.W.)	40.30	74.69	71.84	60.08		
	Edge						
		MgO	NiO	FeO	SiO₂	O _n =	7
A	Av. Wt.% of oxides	3.96	47.14	0.21	40.66		
B	Mol. props. of oxides (A / F.W.)	0.10	0.63	0.00	0.68		ΣC
C	Atom. props. of O per mol. (B x O in oxide)	0.10	0.63	0.00	1.35		2.09
D	No. Anions on basis of O_n (C x (O_n / ΣC))	0.33	2.12	0.01	4.54		
E	No. Ions in formula (D x cations per O)	0.33	2.12	0.01	2.27		
F	Tet. : Oct. ratio from E:	2.458 : 2.271 \approx 3 : 2					
G	Formula normalised from ideal stoichiometry	(Mg_{0.14}, Ni_{0.86})₃Si₂O₅(OH)₄					
	Core						
		MgO	NiO	FeO	SiO₂	O _n =	16
A	Av. Wt.% of oxides	14.94	24.25	0.05	54.08		
B	Mol. props. of oxides (A / F.W.)	0.37	0.32	0.00	0.90		ΣC
C	Atom. props. of O per mol. (B x O in oxide)	0.37	0.32	0.00	1.80		2.50
D	No. Anions on basis of O_n (C x (O_n / ΣC))	2.38	2.08	0.00	11.54		
E	No. Ions in formula (D x cations per O)	2.38	2.08	0.00	5.77		
F	Tet. : Oct. ratio from E:	4.46 : 5.77 \approx 4 : 6					
G	Formula normalised from ideal stoichiometry	(Mg_{0.53}Ni_{0.47})₄Si₆O₁₅(OH)₂·6H₂O					

Table 8: Molecular formula calculation from wt.% oxide data with H₂O content assumed.

This calculation gives O:T ratios for the “edge” and “core” with acceptable relationship to serpentine ((Ni,Mg)₃Si₂O₅(OH)₄) 3:2 and falcondoite ((Mg,Ni)₄Si₆O₁₅(OH)₂·6H₂O) 4:6 respectively, allowing an indication of the compositions of both phases to be made; the serpentine phase being close to an end-member Ni-serpentine phase ((Mg_{0.14}, Ni_{0.86})₃Si₂O₅(OH)₄) and the falcondoite phase close to a 50:50 Ni/Mg falcondoite ((Mg_{0.53}Ni_{0.47})₄Si₆O₁₅(OH)₂·6H₂O).

Problems and limitations

The nature and complexity of these samples coupled with the limitations of the technique introduce general problems as well as problems specific to each sample. For (these) data to be considered valid these shortfalls must be at least acknowledged and justified.

Ideal models for individual mineral species can be calculated to give expected experimental totals and wt.% oxide values for each cation ($\text{H}_2\text{O}\%$ cannot be measured but can generally be assumed to be the difference between the experimental total and 100%). However, comparison of formulae determined from talc models, with those calculated from the data is not ideal, due to the variation in stoichiometries and presence of other cations in these systems.

Despite this, some guidance can be taken from general ranges for expected data. For example, in a sample containing a serpentine phase with both Ni and Mg, by calculating the end-member ideal data for a Mg-serpentine and a Ni-serpentine it can be assumed that these should be the approximate limits expected for points where a serpentine phase is observed. However, this becomes much more difficult to assess with substitution of other elements such as Al, which can occupy both octahedral and tetrahedral sites and Fe which can occur in more than one valence state (i.e. Fe^{2+} and Fe^{3+}).

Deviation of experimental data from these ideal ranges can also be expected but must be explained. The most frequently encountered problem associated with these samples is large variation in the experimental totals. Reasons for this include topographical problems with the sample surface (as these types of material can be very difficult to prepare a smooth polished surface on) and alteration of the sample due to the actual experimental technique.

Experimental issues can occur due to several factors. Firstly, the H_2O content of these hydrous materials samples can be easily reduced when held in a high vacuum. Secondly, the high energy of the electron beam can alter the sample within the analysis volume, this effect can be limited experimentally but a compromise has to be reached on two factors; the longer the beam counts at a point the more chance there is for the sample to be altered but the better the data for the point will be; a more focused beam, required due to the fine-grained nature of these materials, will cause more damage to the sample. As these materials are inherently fine grained, greater issues can be related with sampling a volume over a grain boundary, in

addition to this the larger the spot size the more time is required to acquire good data drastically reducing the efficiency of data collection.

Possible problems with dehydration are noticed in this sample with the falcondoite-type phase giving experimental totals averaging at 93.31% compared to the expected 80-84%.

Elemental mapping

Elemental maps provide predominantly qualitative information, which can be backed up by quantitative data from point analysis, but also offer extra dimensions of information not easily achievable with point analysis. EPMA elemental mapping can give a broader overall picture of the composition of a sample and can readily identify phenomena or trends in compositional variation through a sample, which can be missed with point analysis alone.

Elemental maps were acquired for 1 area of sample M14707. Of the elemental maps acquired notable observations were only made in the maps for Si, Mg, Ni and Fe (see Fig. 50). The area chosen for the elemental map was selected to include the two main features of the sample, the bright “edge” and darker “core” to develop the understanding of these regions and provide information relating to the compositional variations throughout them, notably in Ni and Mg occupancy through the sample. The maps show good agreement with the point analysis data. Elevated Si presence in the core compared to the edge corresponds with the respective O:T cation ratios 4:6 and 3:2 in the falcondoite $(\text{Ni,Mg})_4\text{Si}_6\text{O}_{15}(\text{OH})_2$ and serpentine $((\text{Ni,Mg})_3\text{Si}_2\text{O}_5(\text{OH})_4)$ phases present. As seen in the point analysis data, Mg is observed at higher levels in the core than the edge, Ni at higher levels in the edge than the core and Fe shows some preferential zoning in the core but with less contrast than Mg and Ni. Ni and Mg also show some interesting trends whereby regions of elevated Ni content within the core (generally towards the centre) show markedly reduced Mg occupancy and a similar effect is also observed in the edge where a Mg enriched pattern is mirrored by Ni deficiency in the same zones (this explains why the standard deviation of both Mg and Ni are relatively high for both groups, see table 7). This can be explained by Mg-Ni substitution occurring with natural alteration of the material thorough laterization.

Additional to these observations this sample is also unusual as the less-hydrous serpentine phase has overgrown the hydrous falcondoite-type phase, suggesting possible low

temperature (max. 25°C) diagenetic serpentine formation. Further investigation will be required to understand this.

This general process has been used to analyse and present the EPMA data acquired for each of the natural samples a summary of the findings are presented in Table 9 with analysis for the remaining samples presented here in a more abbreviated form.

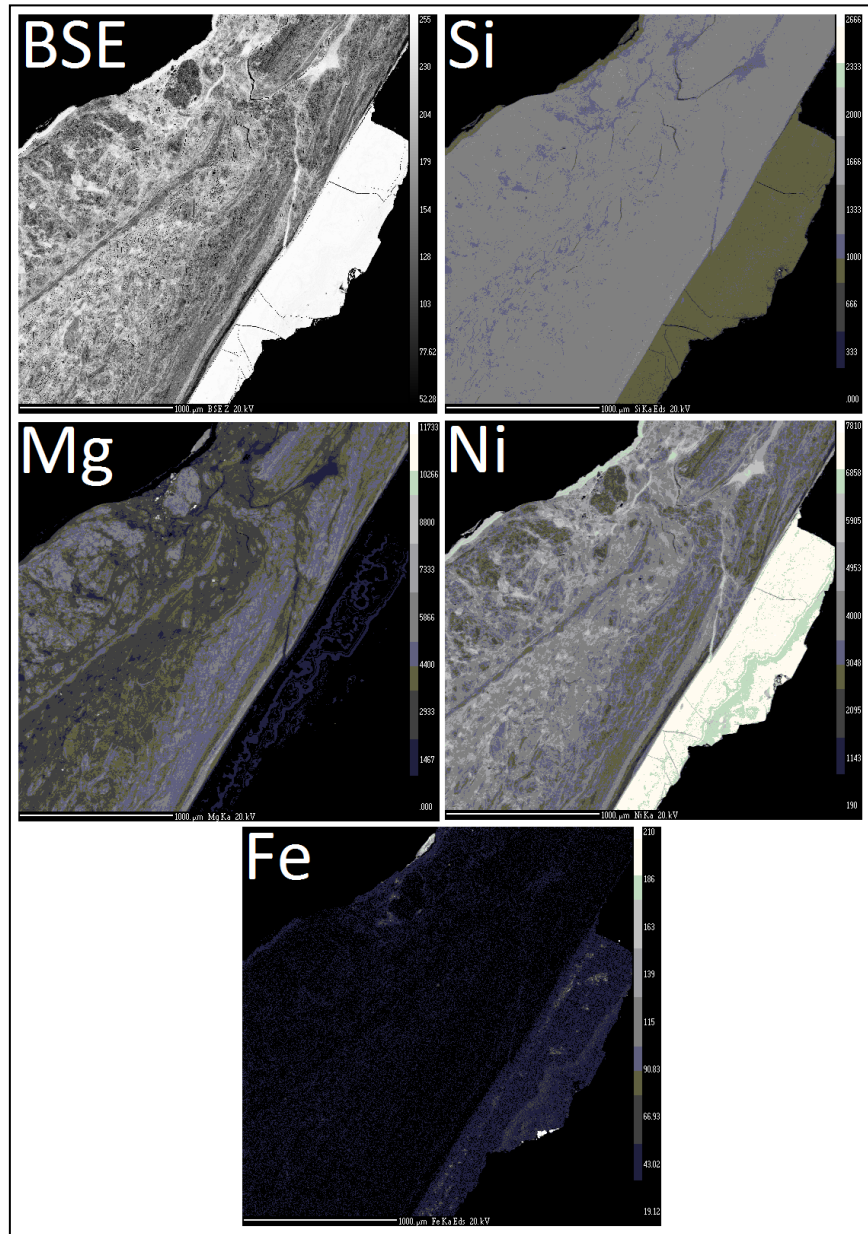


Figure 50: Elemental maps acquired for sample M14707. Level of brightness pertains to element concentration at that point, the brighter the point the higher the concentration.

Sample Name	Phases Identified Using PXRD (ICDD card no.)	EPMA Analyses	EPMA Conclusions	Formulae Calculated
09NIC050501	(46-1322) Clinochlore- $\text{Mg}_6(\text{Si},\text{Al})_4\text{O}_{10}(\text{OH})_8$	Point Analysis (7 Areas, 57 Pts)	Chlorite-type ($\text{Mg}_6\text{Si}_4\text{O}_{10}(\text{OH})_8$) phase observed containing: Mg, Al, Fe, Ni and Ti	Chlorite: $(\text{Mg}_{0.71}, \text{Al}_{0.05}, \text{Fe}_{0.23}, \text{Ni}_{0.01})_6(\text{Si}_{0.92}, \text{Al}_{0.07}, \text{Ti}_{0.01})_4\text{O}_{10}(\text{OH})_8$
	(43-310) Ni,Al,Si hydroxide hydrate			
09NIC110512	(76-1782) Gibbsite – $\text{Al}(\text{OH})_3$	Point Analysis (3 Areas, 71 Pts)	Data analysis in progress	N/A
	(83-2247) Ktenasite – $(\text{Cu},\text{Zn})_5(\text{SO}_4)_2(\text{OH})_6 \cdot 6\text{H}_2\text{O}$			
	(19-770) Talc- $\text{Mg}_3\text{Si}_4\text{O}_{10}(\text{OH})_2$			
	(25-645) Chrysotile- $\text{Mg}_3\text{Si}_2\text{O}_5(\text{OH})_4$			
B105.9.0	(23-603) Manganocummingtonite - $\text{Na}(\text{Na},\text{Mn})_2(\text{Mg}_4,\text{Fe}^{3+})_5\text{Si}_8\text{O}_{22}(\text{OH})_2$	Point Analysis (3 Areas, 73 Pts)	Several different phases are observed including Mn and Cr enriched zones. Variation in composition is very large across any group of points making phase determination very difficult. Serpentine, chlorite and manganocummingtonite are not determined from data.	Asbolane: $\text{Ni}_{0.38}\text{Mg}_{0.11}\text{Ca}_{0.07}\text{Mn}_{1.87}\text{O}_{1.5}(\text{OH})_2 \cdot 0.6(\text{H}_2\text{O})$ Chromite: $(\text{Mg}_{0.48}\text{Fe}_{1.23})(\text{Cr}_{0.79}\text{Al}_{0.61})\text{O}_4$ FeO (<8%) talc: $(\text{Mg}_{0.70}, \text{Fe}_{0.13}, \text{Ni}_{0.17})_3\text{Si}_4\text{O}_{10}(\text{OH})_2$ FeO (>24%) talc: $(\text{Mg}_{0.18}, \text{Fe}_{0.75}, \text{Ni}_{0.07})_3\text{Si}_4\text{O}_{10}(\text{OH})_2$ FeO (10-17%) talc: $(\text{Mg}_{0.53}, \text{Fe}_{0.29}, \text{Ni}_{0.18})_3\text{Si}_4\text{O}_{10}(\text{OH})_2$
	(19-770) Talc- $\text{Mg}_3\text{Si}_4\text{O}_{10}(\text{OH})_2$			
	(25-645) Chrysotile- $\text{Mg}_3\text{Si}_2\text{O}_5(\text{OH})_4$			
	(46-1322) Clinochlore - $\text{Mg}_6(\text{Si},\text{Al})_4\text{O}_{10}(\text{OH})_8$			
B122. 21.2	(25-645) Chrysotile- $\text{Mg}_3\text{Si}_2\text{O}_5(\text{OH})_4$	Point Analysis (2 Areas, 43 Pts)	Sample has little variation in BSE imaging except a few bright inclusions (high Ti or Ca). The best match for the data is as an illite $(\text{Al},\text{Mg},\text{Fe})_2(\text{Si},\text{Al})_4\text{O}_{10}[(\text{OH})_2(\text{H}_2\text{O})]$ type mineral phase.	Illite: $(\text{Mg}_{0.52}, \text{Al}_{0.33}, \text{Fe}_{0.07}, \text{Ni}_{0.08})_2(\text{Si}_{0.86}, \text{Al}_{0.14})_4\text{O}_{10}(\text{OH})_2(\text{H}_2\text{O})$
	(46-1322) Clinochlore- $\text{Mg}_6(\text{Si},\text{Al})_4\text{O}_{10}(\text{OH})_8$			
	(19-770) Talc- $\text{Mg}_3\text{Si}_4\text{O}_{10}(\text{OH})_2$			
CM048B.97	(19-770) Talc- $\text{Mg}_3\text{Si}_4\text{O}_{10}(\text{OH})_2$	Point Analysis (6 Areas, 38 Pts)	Quartz, serpentine and talc are all observed, as well as a Cr rich phase similar to chromite.	Serpentine: $(\text{Mg}_{0.71}, \text{Fe}_{0.16}, \text{Ni}_{0.13})_3\text{Si}_2\text{O}_5(\text{OH})_4$ Talc: $(\text{Mg}_{0.21}, \text{Fe}_{0.08}, \text{Ni}_{0.71})_3\text{Si}_4\text{O}_{10}(\text{OH})_2$
	(25-645) Chrysotile- $\text{Mg}_3\text{Si}_2\text{O}_5(\text{OH})_4$			
	(46-1045) Quartz- SiO_2			

Table 9: Summary of EPMA data analysis results 1/2.

Sample Name	Phases Identified Using PXRD (ICDD card no.)	EPMA Analyses	EPMA Conclusions	Formulae Calculated
CM053.97	(46-1045) Quartz- SiO_2	Point Analysis (5 Areas, 72 Pts) Elemental Maps (1 Area)	Quartz and talc type phases are observed, although serpentine is not. Elemental maps concur with the point analysis data and also show evidence of Ni-Mg substitution.	low Ni talc: $(\text{Mg}_{0.69}, \text{Fe}_{0.01}, \text{Ni}_{0.30})_3 \text{Si}_4\text{O}_{10}(\text{OH})_2$ high Ni talc: $(\text{Mg}_{0.27}, \text{Fe}_{0.01}, \text{Ni}_{0.72})_3 \text{Si}_4\text{O}_{10}(\text{OH})_2$
	(25-645) Chrysotile- $\text{Mg}_3\text{Si}_2\text{O}_5(\text{OH})_4$			
	(19-770) Talc- $\text{Mg}_3\text{Si}_4\text{O}_{10}(\text{OH})_2$			
M14707	(25-645) Chrysotile- $\text{Mg}_3\text{Si}_2\text{O}_5(\text{OH})_4$	Point Analysis (3 Areas, 75 Pts) Elemental Maps (1 Area)	Serpentine (near Ni end-member) and Falcondoite (near 50:50 Ni-Mg) observed Elemental maps concur with the point analysis data and also show evidence of Ni-Mg substitution.	Ni serpentine: $(\text{Mg}_{0.14}, \text{Ni}_{0.86})_3\text{Si}_2\text{O}_5(\text{OH})_4$ Falcondoite: $(\text{Mg}_{0.53}\text{Ni}_{0.47})_4\text{Si}_6\text{O}_{15}(\text{OH})_2 \cdot 6\text{H}_2\text{O}$
	(29-1433) Falcondoite- $\text{Ni}_4\text{Si}_6\text{O}_{15}(\text{OH})_2 \cdot 6\text{H}_2\text{O}$			
OR.467	(46-1045) Quartz- SiO_2	Point Analysis (4 Areas, 58 Pts) Elemental Maps (1 Area)	Quartz and a Ni/Mg talc-type phase are readily identified but serpentine phase not observed Elemental maps concur with the point analysis data and also show evidence of Ni-Mg substitution.	low Ni talc: $(\text{Mg}_{0.55}, \text{Ni}_{0.45})_3 \text{Si}_4\text{O}_{10}(\text{OH})_2$ high Ni talc: $(\text{Mg}_{0.33}, \text{Ni}_{0.67})_3 \text{Si}_4\text{O}_{10}(\text{OH})_2$
	(19-770) Talc- $\text{Mg}_3\text{Si}_4\text{O}_{10}(\text{OH})_2$			
	(25-645) Chrysotile- $\text{Mg}_3\text{Si}_2\text{O}_5(\text{OH})_4$			
Pimelite. Bohemia.860	(43-310) Ni, Al, Si hydroxide hydrate $((\text{Ni}, \text{Al})_3(\text{Al}, \text{Si})_4\text{O}_{10}(\text{OH})_2 \cdot 4(\text{H}_2\text{O}))$	Point Analysis (5 Areas, 40 Pts)	3 phases identified from EPMA, some Ca (possibly diopside $(\text{MgCaSi}_2\text{O}_6)$ or grossular $(\text{Ca}_3\text{Al}_2(\text{SiO}_4)_3$ type) inclusions and 2 silicate phases. Determination of silicate phases not achieved to date. chlorite/vermiculite/odinite.	N/A
	(46-1322) Clinochlore- $\text{Mg}_6(\text{Si}, \text{Al})_4\text{O}_{10}(\text{OH})_8$			

Table 9: Summary of EPMA data analysis results 2/2.

4.3.2. CMO48B.97

Sample CMO48B.97 is from a nickel laterite mine site in Cerro Matoso. The material consists of three visibly different materials, a brown phase a green phase and a white vein-like phase (see Fig. 51).



Figure 51: Photograph of sample CMO48B.97

PXRD has shown: quartz is found throughout the sample, the brown coloured region contains a major serpentine-type phase and shows elevated Fe content and the green coloured region contains a major talc-type phase. Detailed analysis of the acquired EPMA data has been performed to characterize this sample further. Using BSE imaging several different phases are observed within the sample, with a large variation in brightness as well as grain shape and size. Point analyses were acquired at 6 different areas, with a total of 38 points taken over these areas. From the 38 points; 2 points were discarded with totals less than 70% (low SiO₂ suggested possible oxide/oxy-hydroxide-type phases); 6 points gave SiO₂ values close to 100% indicating the presence of quartz; 1 point had high Cr₂O₃ (28.60%) and virtually no SiO₂, suggesting an oxide inclusion similar to a chromite-type phase ((Fe,Mg)(Cr,Al)₂O₄) with corresponding high Al, Mg and Fe (although the data does not fit chromite stoichiometrically from calculations). This leaves 29 silicate points remaining; manipulation of the data identifies 2 points significantly different to the majority, with Al content notably higher than all other points analysed. The two points also differ significantly to each other with reference to Al, Si, Ni and experimental totals (see table 10) so cannot be considered related. Also, whilst they may indicate presence of Al-rich inclusions, the data points are close to grain boundaries, which may contribute anomalous data.

Area	Point	MgO	Al ₂ O ₃	SiO ₂	CaO	FeO	NiO	Total
4	2	4.24	33.48	25.14	0.54	4.97	16.57	85.73
6	7	5.9	3.72	81.27	0.14	5.75	2.49	99.56

Table 10: Table of wt.% oxide point analysis data from CM048B.97 showing differences between the two discarded Al-rich points.

These points were subsequently discarded and the remaining 27 points further divided into: points with NiO >20% (14 pts.) and points with NiO <11% (13 pts.). Averages, standard deviations and the results from formulae calculations for the 2 groups are given in table 11. These results show that from the grouped averages the phase with low Ni content is closest to a serpentine-type stoichiometry (O:T = 3:2) giving a normalized formula of (Mg_{0.71}, Fe_{0.16}, Ni_{0.13})₃Si₂O₅(OH)₄ and the phase with elevated Ni content is closest to a talc-type stoichiometry (O:T = 3:4) giving a normalized formula of (Mg_{0.21}, Fe_{0.08}, Ni_{0.71})₃Si₄O₁₀(OH)₂, assuming Mg, Ni, Fe and half the Al are octahedral and the Si and half the Al are tetrahedral. This fits well with previous work, although the average experimental totals acquired for the points are significantly lower than expected for both phases, this may be purely due to sample dehydration issues.

NiO <11%		MgO	Al ₂ O ₃	SiO ₂	CaO	FeO	NiO	Total	Red. Total	Diff
	Av.	23.68	0.72	40.11	0.22	9.49	7.82	82.68	82.03	0.64
	Sd.	5.72	0.52	2.63	0.11	3.70	1.77	2.78	2.83	0.25
n=	13									
NiO min=	4.82									
NiO max=	10.36									
NiO >20%		MgO	Al ₂ O ₃	SiO ₂	CaO	FeO	NiO	Total	Red. Total	Diff
	Av.	5.10	0.13	44.52	0.29	3.73	32.50	86.64	86.28	0.36
	Sd.	2.81	0.14	2.78	0.08	1.14	5.56	4.53	4.52	0.05
n=	14									
NiO min=	21.19									
NiO max=	39.18									
No. Of ions in formula										
	Mg	Al	Si	Ca	Fe	Ni	O:T	Formula		
NiO <11% (on basis of 7 O) i.e. Serpentine M ₃ Si ₂ O ₅ (OH) ₄	1.89	0.02	2.15	0.01	0.43	0.34	2.66 : 2.15 (ideal=3:2)	(Mg _{0.71} , Fe _{0.16} , Ni _{0.13}) ₃ Si ₂ O ₅ (OH) ₄		
NiO >20% (on basis of 11 O) i.e. talc M ₃ Si ₄ O ₁₀ (OH) ₂	0.66	0.01	3.88	0.03	0.27	2.28	3.21 : 3.88 (ideal=3:4)	(Mg _{0.21} , Fe _{0.08} , Ni _{0.71}) ₃ Si ₄ O ₁₀ (OH) ₂		

Table 11: Results tables for point analysis data groups from CM048B.97

4.3.3. CM053.97

CM053.97 is a specimen from a nickel laterite mine site in Cerro Matoso. The sample shows two clear zones, a massive orange/brown zone and a green zone. Quartz-type veins are observed within both zones of the rock but are more prominent in the green zone where alternating layers of white and green materials are seen (see Fig. 52).

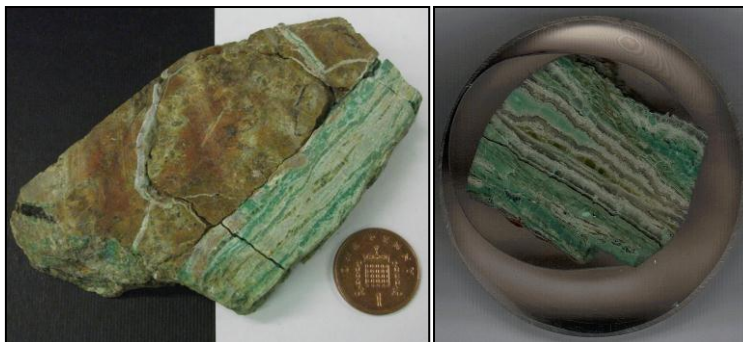


Figure 52: Photographs of sample CM053.97; whole (left) and resin mounted section for EPMA (right).

From PXRD the brown phase was shown to contain a serpentine-type phase and quartz and the green/white layered material was shown to contain quartz, talc and serpentine. Given the colouration of the green phase (which suggests elevated Ni content) and the identification of talc and serpentine as significant phases to the study of Ni-bearing hydrous silicates, the green material was chosen for EPMA analysis (see Fig. 52).

BSE-imaging shows 3 likely differences in composition, a dark phase, an intermediate phase and a notably brighter vein-like which tends to be concentrated towards the edges of the intermediate phase grains (see Fig. 53).

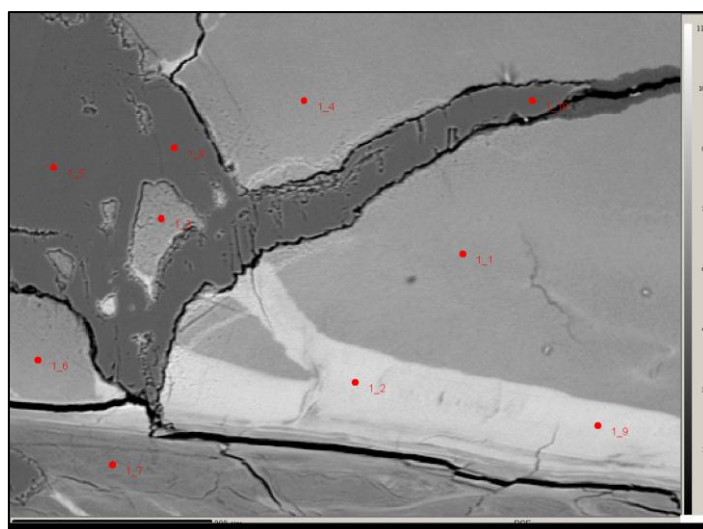


Figure 53: CM053.97; BSE-image from EPMA point analysis.

(red spots indicate points analysed)

Point Analysis

Point analyses were acquired at 5 different areas, with a total of 72 points taken over these areas.

From the 72 points; 6 were discarded with low wt.% oxide totals (<70%); 15 points were clearly identified as quartz ($\text{SiO}_2 \approx 100\%$), matching with the PXRD pattern; and the remaining 51 points can be separated into 2 groups; where $\text{NiO} < 27\%$ (34 pts.) and where $\text{NiO} > 33\%$ (17 pts.). Averages, standard deviations and the results from formulae calculations for the 2 groups are given in table 12

These results show that from the grouped averages both sets of data for the silicates approximate best to a talc stoichiometry (O:T, 3:4) which fits with talc observed in the PXRD pattern as the major phase, although no points match the observed serpentine phase, suggesting this may have been purely a contribution from the brown material contaminating the green material.

NiO <27%		MgO	Al₂O₃	SiO₂	CaO	FeO	NiO	Total	Red. Total	Diff
	Av.	20.90	0.00	54.02	0.12	0.63	17.06	92.97	92.71	0.25
	Sd.	2.50	0.01	1.17	0.02	0.10	4.11	1.53	1.52	0.04
n=	34									
NiO min=	8.92									
NiO max=	26.88									
NiO >33%		MgO	Al₂O₃	SiO₂	CaO	FeO	NiO	Total	Red. Total	Diff
	Av.	7.52	0.02	49.15	0.10	0.53	37.28	94.74	94.59	0.15
	Sd.	1.31	0.11	0.86	0.03	0.08	1.75	1.22	1.21	0.04
n=	17									
NiO min=	33.86									
NiO max=	39.89									

	No. Of ions in formula							
	Mg	Al	Si	Ca	Fe	Ni	O : T	Formula
NiO <27% (on basis of 11 O) i.e. Talc $M_3Si_4O_{10}(OH)_2$	2.23	0.00	3.87	0.01	0.04	0.98	3.25:3.87 (ideal=3:4)	$(Mg_{0.69},Fe_{0.01},Ni_{0.30})_3Si_4O_{10}(OH)_2$
NiO >33% (on basis of 11 O) i.e. Talc $M_3Si_4O_{10}(OH)_2$	0.88	0.00	3.86	0.01	0.03	2.36	3.27:3.86 (ideal=3:4)	$(Mg_{0.27},Fe_{0.01},Ni_{0.72})_3Si_4O_{10}(OH)_2$

Table 12: Results tables for point analysis data groups from CM053.97

Elemental Mapping

Elemental maps were also acquired for 1 area of sample CM053.97. Of the elemental maps acquired notable observations were only made in the maps for Si, Mg and Ni (see Fig. 54). The maps show good agreement with the point analysis data.

The Si map shows separation of the clear SiO₂ quartz regions (bright) and the duller Mg/Ni silicate regions. The Ni and Mg maps show that the bright Ni-rich veining observed in BSE is compliant with Mg deficient zones and that there are degrees of variation through the whole silicate phase pertaining to a Ni-Mg solid solution series.

BSE-imaging shows brightness decreases in the silicate phase as Ni is reduced. This effect demonstrates well the benefit of elemental mapping as the bright diamond shaped zone towards the bottom and centre of the Mg map is indistinguishable in the BSE-image from the adjacent quartz channel but mapping shows this difference clearly.

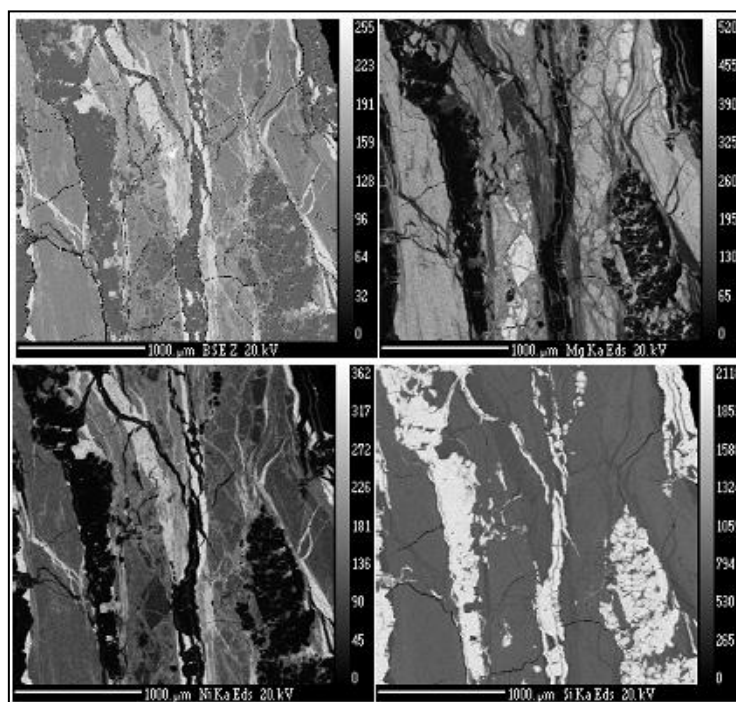


Figure 54: CM053 BSE-image and elemental maps for Mg, Si and Ni (going clockwise from top left).

4.3.4. OR.467

OR467 is a saprolitic sample from a nickel mine site in Cerro Matoso. The specimen exhibits layers of varying thickness alternating between a bright green material and a white/translucent material (see Fig. 55). PXRD studies of this specimen identify quartz and talc as the main constituents with some likely contribution from a serpentine-type phase also.



Figure 55: Photograph of sample OR467

BSE-imaging of OR467 shows clear compositional differences through the sample (see Fig. 56); the layering effect observed in the photograph of the sample (Fig. 55) is mirrored by clear dark channels in the BSE-image, separated by layers of intermediate brightness grains and a phase with unusual bright-intermediate patterning with inkblot or stain-like appearance.

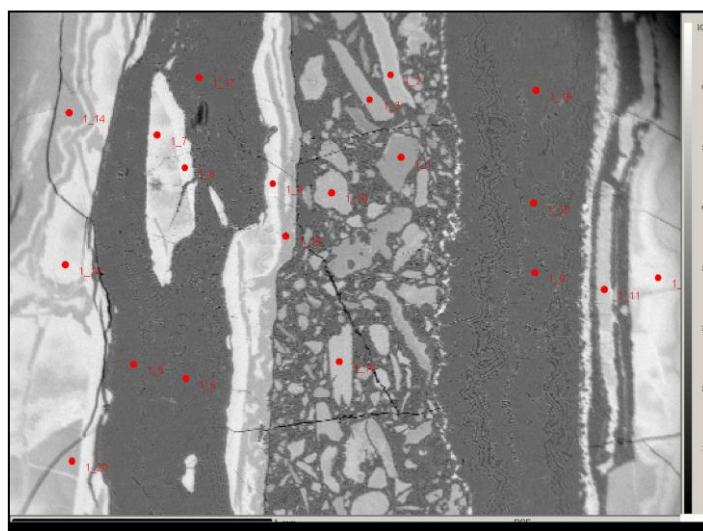


Figure 56: CM053.97; BSE-image from EPMA point analysis
(red spots indicate points analysed)

Point Analysis

Point analyses were acquired at 4 different areas, with a total of 58 points taken over these areas.

From the 58 points; all 11 points from 1 area were discarded as totals were low, likely due to poor beam focus; 15 points were clearly identified as quartz ($\text{SiO}_2 \approx 100\%$), matching with the PXRD pattern; and the remaining 32 Ni/Mg/Fe-silicate type points can be sorted to 2 groups: with NiO <28% (17 pts.) and with NiO >32% (15 pts.). Averages, standard deviations and the results from formulae calculations for the 2 groups are given in table 13.

NiO <28%		MgO	SiO ₂	FeO	NiO	Total	Red. Total	Diff
	Av.	15.45	54.20	0.22	23.86	93.98	93.73	0.25
	Sd.	1.96	1.12	0.10	2.89	1.04	1.09	0.10
n =	17							
NiO min. =	16.3							
NiO max. =	27.62							
NiO >32%		MgO	SiO ₂	FeO	NiO	Total	Red. Total	Diff
	Av.	9.16	49.09	0.23	34.67	93.43	93.15	0.28
	Sd.	1.25	1.42	0.21	1.50	1.05	1.10	0.14
n =	15							
NiO min. =	32.33							
NiO max. =	36.92							
		No. Of ions in formula						
		Mg	Si	Fe	Ni	O : T	Formula	
NiO <28% (on basis of 11 O) i.e. Talc $M_3Si_4O_{10}(OH)_2$		1.68	3.95	0.01	1.40	3.08 : 3.95 (ideal=3:4)	$(Mg_{0.55}, Ni_{0.45})_3 Si_4O_{10}(OH)_2$	
NiO >32% (on basis of 11 O) i.e. Talc $M_3Si_4O_{10}(OH)_2$		1.07	3.86	0.02	2.19	3.27 : 3.86 (ideal=3:4)	$(Mg_{0.33}, Ni_{0.67})_3 Si_4O_{10}(OH)_2$	

Table 13: Results tables for point analysis data groups from OR.467

Calculations give stoichiometries closest to talc (O:T, 3:4) for both groups of data, which matches the PXRD study, although no serpentine contribution is observed at any point, suggesting its occurrence in this sample is limited. Further scrutiny of these data finds that SiO₂ is higher in the NiO <28% group and that the sum of assumed octahedral cation oxides (NiO, MgO, FeO) is lower in this group also which explains its closer corroboration to a talc stoichiometry (O:T, 3:4) at (3.08:3.95) than the NiO>32% group given as (3.27:3.86); this effect may be a result of mobilization of Si and Mg from the talc phase through weathering, which could explain the unusual “staining” appearance in BSE-imaging where the brightest (Ni-rich) areas are Mg deficient, going towards explaining why this phenomenon is concentrated at the edges and faults in these silicate zones.

Elemental Mapping

Elemental maps were also acquired for 2 areas of sample OR.467. Of the elemental maps acquired notable observations were only made in the maps for Si, Mg and Ni (see figs. 57 & 58). The maps show good agreement with the point analysis data.

Elemental mapping shows the unusual stain-like Mg-Ni substitution effect (observed in the point analysis data) more noticeably with clear Mg deficiency in Ni-rich areas and vice versa with Mg and Ni displaying a solid solution within the sample. The more subtle effect of reduced Si content in the Ni-rich areas can also be observed in the Si maps.

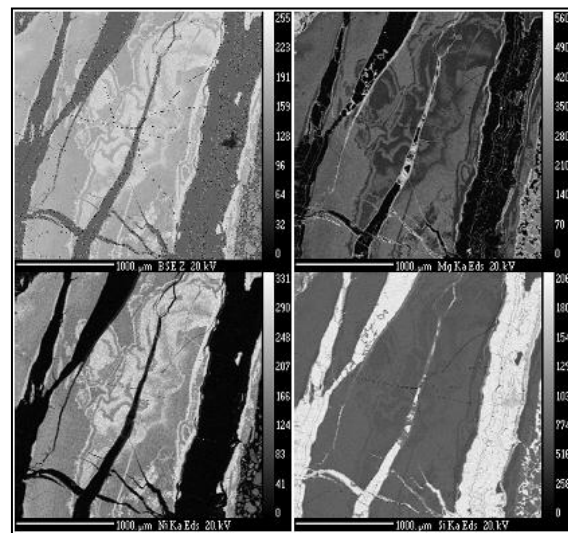


Figure 57: OR467: Map 1; BSE-image and elemental maps for Mg, Si and Ni
(clockwise from top left).

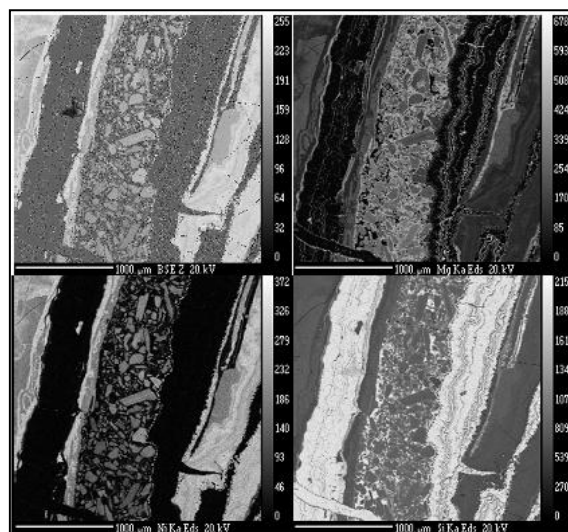


Figure 58: OR467: Map 2; BSE-image and elemental maps for Mg, Si and Ni.
(clockwise from top left)

4.3.5. B105.9.0

B105.9.0 is from the Shevchenko Ni deposit in Kazakhstan. The sample is an olive green material that crumbles easily, with some darker green/brown material also present randomly dispersed within the mass (see Fig. 59). PXRD studies of the sample identify talc, serpentine, chlorite and manganocummingtonite presence within the specimen (see Fig. 60). This clear identification of relevant phases from PXRD necessitated EPMA analysis.



Figure 59: Photo of sample B105.9.0

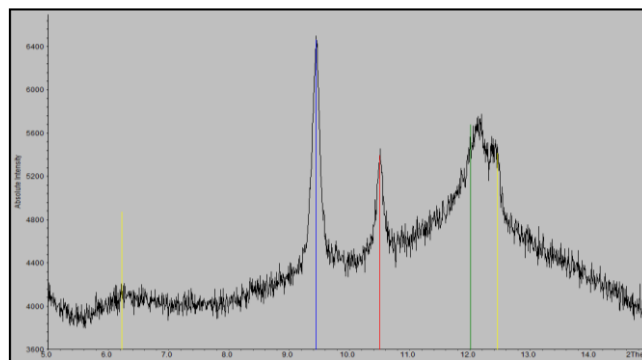


Figure 60: Expanded section of PXRD pattern for B105.9.0.
Showing match to ICDD patterns for: talc (blue); manganocummingtonite (red); chrysotile (green); clinocllore (yellow)

BSE-imaging of B105.9.0 clearly shows the complexity of the sample with multiple different phases apparent with large variation in grain size and brightness across the whole sample (see Fig. 61)

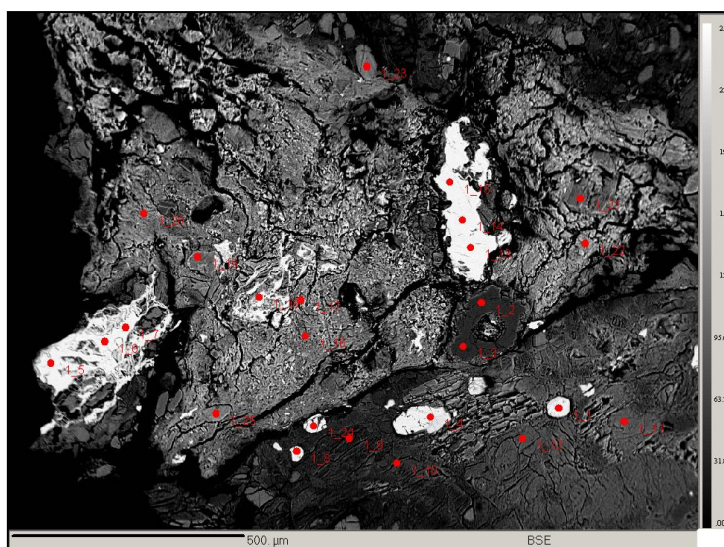


Figure 61: B105.9.0; BSE-image from EPMA point analysis
(red spots indicate points analysed)

Point Analysis

Point analyses were acquired at 3 different areas for a total of 73 points. From the 73 points the first thing that was noticed was the unusual occurrence of high MnO values, with 17 points containing MnO >1%. Closer investigation of these points identified that 5 Mn-rich points had SiO₂ <2%, indicating an oxide phase opposed to a silicate phase and corresponded to bright patches in the BSE-images (see points 13, 14 and 15 in Fig. 61). However the others showed large compositional variation and inspection indicated the likelihood that these are all due to analysis of multiple phases at grain boundaries as the sample is very complex and fine grained, so were discarded from further analyses.

Of the 56 remaining points; 13 were discarded with totals lower than 70%; 3 were identified as Cr-rich oxide points, pertaining to other bright areas in BSE-imaging (see point 4 in Fig. 61); 2 points were found where SiO₂ accounts for approximately 100% of the experimental total, suggesting there is either an element which was not analysed for or that it is a silica-type inclusion giving a low total, possibly due to topographical issues such as if it is raised or recessed (see doughnut shaped area at points 2 and 3 Fig. 61); 3 points contain Al₂O₃ above 1% (see points 21 and 24 in BSE image Fig. 61), although were not comparable with each other suggesting some Al-rich inclusion phase; and from the 35 remaining points, significant variation is observed in Mg, Fe and Ni.

Manipulation of the 35 data points identifies possible separation into 3 constituent groups based on Fe, Mg and Ni content: points with low FeO (<8%), high MgO and high NiO (10 pts.); points with high FeO (>24%), low MgO and low NiO (13 pts.) and an intermediate group of points with Fe content at 10-17%, with varied MgO and NiO (12pts). Averages, standard deviations and the results from formulae calculations for this sample are given in table 14.

Formula calculations show: the MnO inclusion points gives a close match to an asbolane-type mineral phase ($\text{Ni}_{0.3}\text{Co}_{0.1}\text{Ca}_{0.1}\text{Mn}_{1.5}\text{O}_{1.5}(\text{OH})_2 \cdot 0.6(\text{H}_2\text{O})$), based on 2.5 anions giving the formula: $\text{Ni}_{0.38}\text{Mg}_{0.11}\text{Co}_{0.02}\text{Ca}_{0.07}\text{Mn}_{1.87}\text{O}_{1.5}(\text{OH})_2 \cdot 0.6(\text{H}_2\text{O})$, although it is clear that Co is low, Mn is high and Mg is present in appreciable amounts, the experimental total (85.65) also fits well with this formula; the Cr_2O_3 inclusion points do not fit stoichiometrically with a chromite-type phase (FeCr_2O_4) from calculations giving: $(\text{Mg}_{0.48}\text{Fe}_{1.23})(\text{Cr}_{0.79}\text{Al}_{0.61})\text{O}_4$, where Fe+Mg (1.71) is high and Cr+Al (1.4) is low, but this is still the most likely phase observed given the composition; all three groups of silicates approximate close to a talc-mineral stoichiometry (O:T=3:4) from the formula calculations.

Calculated O:T ratios for groups also show the low FeO (<8%) and intermediate FeO (10-17%) groups are very close to talc stoichiometry at (2.99:3.98) and (3.07:3.92) respectively. Whereas, the high FeO (>24%) group gives a ratio which deviates from the ideal (2.49:4.19) which may be due to Mg and Ni mobilization through weathering.

	Point	Na ₂ O	MgO	Al ₂ O ₃	SiO ₂	CaO	Cr ₂ O ₃	MnO	FeO	CoO	NiO	Exp. Total	Red. Total	Diff. Total
MnO inclusions	Av.	1.09	1.89	0.05	0.19	1.71	0.02	55.60	0.21	0.73	11.92	73.72	73.42	0.30
n=3	Sd.	0.18	0.22	0.02	0.04	0.15	0.01	1.50	0.04	0.03	1.68	0.92	0.88	0.09
Cr₂O₃ inclusions	Av.	0.02	5.52	17.93	1.34	0.05	34.58	0.40	25.39	0.11	0.30	86.37	85.65	0.72
n=3	Sd.	0.01	0.22	0.84	1.00	0.02	1.25	0.04	2.29	0.02	0.15	2.47	2.42	0.08
FeO (<8%)	Av.	0.25	18.90	0.35	53.12	0.28	0.08	0.08	6.03	0.08	8.12	87.51	87.30	0.22
n=10	Sd.	0.11	1.80	0.04	3.61	0.04	0.02	0.03	1.09	0.01	1.72	4.33	4.41	0.08
FeO (>24%)	Av.	0.59	3.53	0.37	50.61	0.87	0.10	0.08	26.97	0.07	2.59	86.02	85.78	0.23
n=13	Sd.	0.34	0.74	0.07	4.67	0.48	0.05	0.07	1.82	0.01	0.52	6.35	6.38	0.13
FeO (10-17%)	Av.	0.36	13.08	0.47	47.07	0.33	0.11	0.11	12.71	0.10	8.08	82.63	82.42	0.22
n=12	Sd.	0.13	2.99	0.17	6.33	0.11	0.09	0.06	2.87	0.03	1.88	5.57	5.61	0.09

	No. Of ions in formula										
	Na	Mg	Al	Si	Ca	Cr	Mn	Fe	Co	Ni	
MnO inclusions based on 2.5 O Asbolane	0.02	0.11	0.00	0.01	0.07	0.00	1.87	0.01	0.02	0.38	Ni _{0.38} Mg _{0.11} Ca _{0.07} Mn _{1.87} O _{1.5} (OH) ₂ •0.6(H ₂ O)
Cr₂O₃ inclusions based on 4 O Chromite (FeCr ₂ O ₄)	0.00	0.48	0.61	0.08	0.00	0.79	0.02	1.23	0.01	0.01	(Mg _{0.48} Fe _{1.23})(Cr _{0.79} Al _{0.61})O ₄
FeO (<8%) based on 11 O Talc - M ₃ Si ₄ O ₁₀ (OH) ₂	0.01	2.11	0.02	3.98	0.02	0.00	0.01	0.38	0.00	0.49	O : T 2.99 : 3.98 (Mg _{0.70} ,Fe _{0.13} ,Ni _{0.17}) ₃ Si ₄ O ₁₀ (OH) ₂
FeO (>24%) based on 11 O Talc - M ₃ Si ₄ O ₁₀ (OH) ₂	0.02	0.44	0.02	4.19	0.08	0.00	0.01	1.87	0.00	0.17	O : T 2.49 : 4.19 (Mg _{0.18} ,Fe _{0.75} ,Ni _{0.07}) ₃ Si ₄ O ₁₀ (OH) ₂
FeO (10-17%) based on 11 O Talc - M ₃ Si ₄ O ₁₀ (OH) ₂	0.01	1.63	0.02	3.92	0.03	0.00	0.01	0.89	0.01	0.54	O : T 3.07 : 3.92 (Mg _{0.53} ,Fe _{0.29} , Ni _{0.18}) ₃ Si ₄ O ₁₀ (OH) ₂

Table 14: Results tables for point analysis data groups from B105.9.0

Elemental Mapping

Elemental maps were also acquired for 1 area of sample B105.9.0. To convey the full complexity and variation across the sample, maps are reported here for Fe, Si, Mn, Mg, Ni, Al, Cr, Ca and Co (Fig. 62). The maps show good agreement with the point analysis data. The Fe distribution corresponds to the identified elevated Si content along with reduced Ni and Mg in these areas, with the converse true also. The high Mn and Cr areas match with Si deficient zones as is expected for oxide phases, whereas, the unusual doughnut shaped high SiO₂ patch is also observed in the Si map as a very bright area suggesting a quartz/chalcedony type inclusion. Ni is observed at appreciable levels through the silicate zones but is shown at highest concentrations, with Co, in Mn-rich areas concurrent with an asbolane-type phase, similarly Al is observed throughout much of the sample and concentrated in Cr-rich areas, indicative of a chromite-type phase.

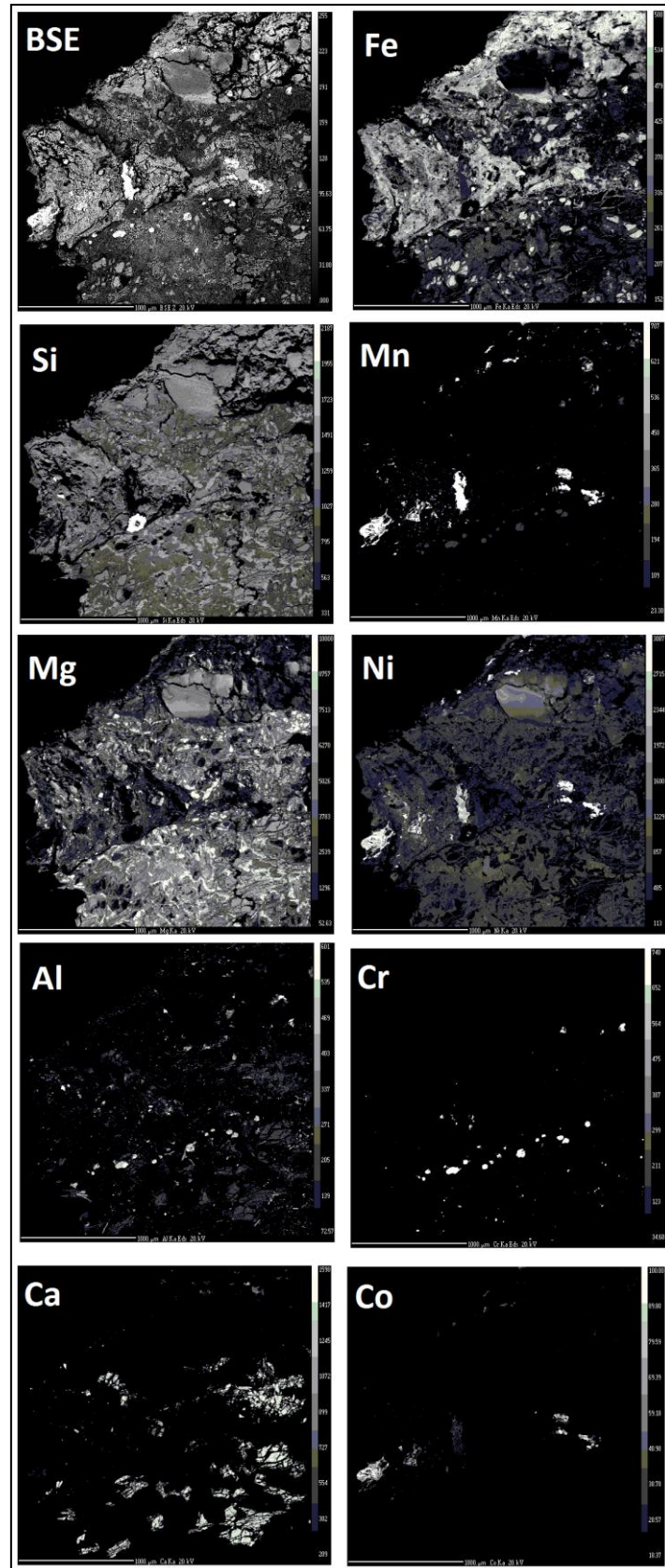


Figure 62: B105.9.0: BSE-image and elemental maps for Fe, Si, Mn, Mg, Ni, Al, Cr, Ca, Co.

4.3.6. B122.21.2

B122.21.2 is from the Shevchenko Ni deposit in Kazakhstan. The sample is predominantly a pale green mass with some black material randomly dispersed throughout and some red/brown tainting to parts of the surface (see Fig. 63). The somewhat homogenous appearance of the green material and the identification of relevant serpentine, talc and chlorite-type minerals from PXRD studies, which are also comparable to sample B105.9.0 from the same locality, were the reasons for selecting this sample for EPMA analysis. BSE imaging of the sample appeared largely homogenous, fine grained and fragmented with a few bright inclusions (see Fig. 64)



Figure 63: Photograph of sample B122.21.2

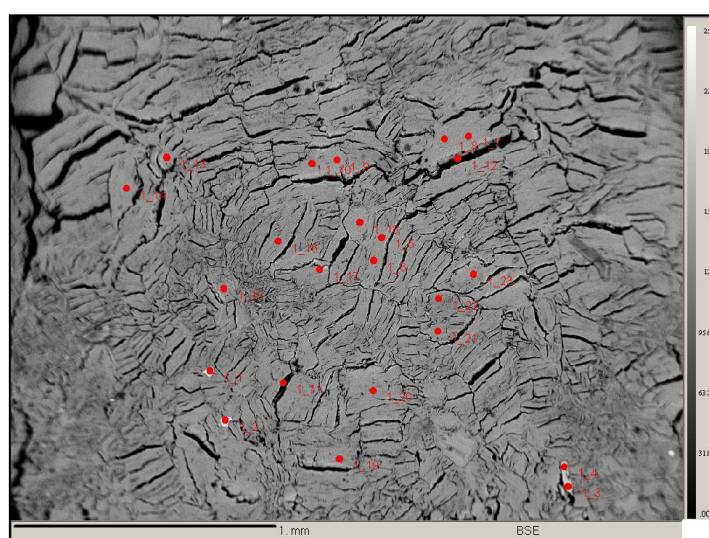


Figure 64: B122.21.2; BSE-image from EPMA point analysis (red spots indicate points analysed).

Point Analysis

Point analyses were acquired at 2 different areas over a total of 43 points. From the 43 points, 4 were discarded with totals below 70% and 8 points were rejected as inclusions, with too few similar data points to count as relevant separate mineral species. These included 1 Ca-rich point, 2 Ti-rich points, 4 points with Cr >0.25% and 1 point with higher Al and lower Fe compared to the rest of the data points. The remaining 31 points returned a reasonable standard deviation and have no other obvious differences, agreeing with the BSE observations. Averages, standard deviations and the results from formulae calculations for this sample are given in table 15.

	MgO	Al ₂ O ₃	SiO ₂	CaO	FeO	NiO	Total	Red. Total	Diff.
Av.	7.65	24.85	46.69	0.36	1.87	2.27	84.10	83.74	0.36
Sd.	1.10	2.27	2.34	0.08	0.39	0.39	4.10	4.13	0.08
n =	31								
NiO min =	1.31								
NiO max =	3.21								
No. Of ions in formula based on 10 O i.e. illite: (Al,Mg,Fe)₂(Si,Al)₄O₁₀[(OH)₂(H₂O)]									
Mg	Al	Si	Ca	Fe	Ni	O : T	Formula		
0.87	1.12	3.58	0.03	0.12	0.14	1.69 : 4.14 (ideal=2:4)	(Mg _{0.52} ,Al _{0.33} ,Fe _{0.07} ,Ni _{0.08}) ₂ (Si _{0.86} ,Al _{0.14}) ₄ O ₁₀ (OH) ₂ (H ₂ O)		

Table 15: Results tables for point analysis data group from B122.21.2

The calculations show the group of 31 points give a stoichiometry reasonably close to the mineral illite (Al,Mg,Fe)₂(Si,Al)₄O₁₀[(OH)₂(H₂O)] (O:T=2:4) calculated on the basis of 10 oxygen atoms, giving an O:T ratio of 1.69:4.14 and approximating to a formula of (Mg_{0.52}, Al_{0.33}, Fe_{0.07}, Ni_{0.08})₂(Si_{0.86}, Al_{0.14})₄O₁₀(OH)₂(H₂O).

Although this shows significant deviation from the phases initially identified from PXRD studies this finding may still be related to the PXRD pattern: the most intense reflection is as observed broad and at low angle (a 2θ angle of approximately 5°), this is characteristic of smectite-type materials which are inherently fine grained and disordered (contributing to the broadening) and have large and variable layer spacing which make them extremely difficult to conclusively identify from a simple PXRD pattern.

4.3.7. 09NIC050501

09NIC050501 was selected for EPMA analysis because high-resolution PXRD suggested the phase was relatively well crystalline, single phase and composed of a phase related to a Ni-bearing vermiculite $((\text{Ni},\text{Al})_3(\text{Al},\text{Si})_4\text{O}_{10}(\text{OH})_2 \cdot 4(\text{H}_2\text{O}), \text{O:T}=3:4)$, making it unusual in the suite of natural samples. Under BSE imaging the material appears largely homogenous (as was suggested from PXRD), in general grains appear to be similar, fragmented and with distinct layering with little contrast variation observed through the material except for a few minor inclusions (see Fig. 65).

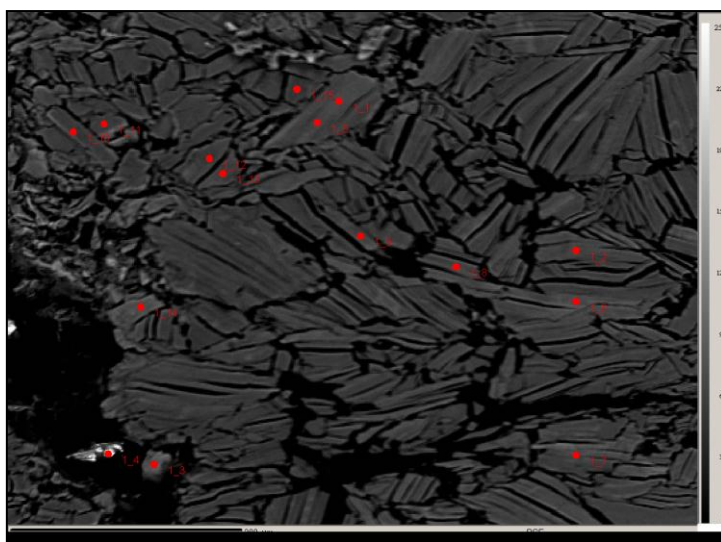


Figure 65: Sample 09NIC050501; Example BSE image.

For sample 09NIC050501 point analysis was acquired at 7 different areas, with a total of 57 points analysed over these areas. From the 57 points; 13 were discarded as totals were below 70%; 1 point displayed Mn presence (MnO, 1.43%) as an inclusion phase and 1 point reported sulphur presence (SO₂, 1.62%) either as an inclusion or more likely from the resin. The remaining 42 points can then be divided into 2 apparent groupings; 33 points with a combined SiO₂ and half Al₂O₃ (i.e. total tetrahedral cations) >40%; and 9 points with a combined SiO₂ and half Al₂O₃ <40%. Averages and standard deviations for these groups are given in table 16 and the results from formulae calculations using these are given in table 17.

Although calculations for the larger (Tet.>40%) group do not give any conclusive formula (see table 17) calculations for the smaller group (Tet.<40%) show good correlation with a

chlorite-type (6:4, O:T) formula with; Mg, Fe, Ni and half the Al assumed as octahedral cations (6.02); and Si, Ti and half the Al assumed as tetrahedral cations (3.98).

This result is contrary to the vermiculite-type phase identified from high resolution PXRD, although chlorite does have a related structure. The EPMA data also suggests that, contrary to both PXRD data and the BSE-imaging, this sample consists of more than 1 silicate-type phase, i.e. the major Tet.>40% group, although no other phase has been determined from the other data so far. This may be partly caused by Fe occurring as Fe^{3+} as well as the Fe^{2+} on which calculations were based on. However, this valency issue is unlikely to be the entire solution as Fe is significantly less abundant in the unaccountable data. Other explanations may be that the other phase/s present are extremely fine grained and therefore have not been represented individually from the data points. Ultimately however, although the material is an unusual example of a Mg-Fe-Al silicate it has low Ni content limiting its significance to the Ni-bearing silicate study.

		MgO	Al ₂ O ₃	SiO ₂	K ₂ O	TiO ₂	FeO	NiO	Total	Red. Total	Diff.	½ Al ₂ O ₃ +Si
1/2Al₂O₃ + SiO₂ >40%	Av.	26.86	12.73	40.48	0.19	0.66	3.87	0.67	85.71	85.46	0.25	46.85
N = 33	Sd.	1.59	1.44	2.17	0.28	0.33	1.8	0.78	3.42	3.42	0.06	2.54
		MgO	Al ₂ O ₃	SiO ₂	K ₂ O	TiO ₂	FeO	NiO	Total	Red. Total	Diff.	½ Al ₂ O ₃ +Si
1/2Al₂O₃ + SiO₂ <40%	Av.	26.32	8.64	33.62	0.04	0.30	14.86	0.95	85.09	84.74	0.36	37.94
N = 9	Sd.	5.58	0.73	1.29	0.04	0.12	3.88	0.83	2.08	2.15	0.10	1.01

Table 16: Sample 09NIC050501: Wt.% oxide averages and standard deviations for determined EPMA point analysis groups. Av.= Average, Sd.= standard deviation, N = number of points in group.

	No. Of Ions in formula							O : T	Formula
1/2Al₂O₃ + SiO₂ >40%	Mg	Al	Si	K	Ti	Fe	Ni		
On basis of 11 O (talc/vermiculite)	3.21	0.60	3.24	0.04	0.04	0.26	0.04	3.81 : 3.58	N/A
On basis of 7 O (serpentine)	2.04	0.38	2.06	0.02	0.03	0.16	0.03	2.42 : 2.28	N/A
On basis of 14 O (chlorite)	4.08	0.76	4.13	0.05	0.05	0.33	0.05	4.84 : 4.56	N/A
	No. Of Ions in formula							O : T	Formula
1/2Al₂O₃ + SiO₂ <40%	Mg	Al	Si	K	Ti	Fe	Ni		
On basis of 11 O (talc/vermiculite)	3.38	0.44	2.89	0.01	0.02	1.07	0.07	4.74 : 3.13	N/A
On basis of 7 O (serpentine)	2.15	0.28	1.84	0.01	0.01	0.68	0.04	3.01 : 1.99	N/A
On basis of 14 O (chlorite)	4.30	0.56	3.68	0.01	0.02	1.36	0.08	6.02 : 3.98	(Mg _{0.71} , Al _{0.05} , Fe _{0.23} , Ni _{0.01}) ₆ (Si _{0.92} , Al _{0.07} , Ti _{0.01}) ₄ O ₁₀ (OH) ₈

Table 17: Sample 09NIC050501; formulae calculations from average data for point analysis groups.

4.3.8. Pimelite Bohemia.860

This sample, from the historical collections at the Natural History Museum London, is from the Czech Republic. The sample consists of a relatively hard olive green mass with some small shiny mica type plates on the surface (see Fig. 66)

The PXRD pattern for Pimelite.Bohemia.860 (see Fig. 67) shows a combination of sharp reflections and broad bumps indicating a mixture of crystalline and disordered phases. The crystalline phase is identified to be related to ICDD data for clinocllore ($\text{Mg}_6(\text{Si},\text{Al})_4\text{O}_{10}(\text{OH})_8$) or a Ni-substituted vermiculite type phase ($(\text{Ni},\text{Al})_3(\text{Al},\text{Si})_4\text{O}_{10}(\text{OH})_2 \cdot 4(\text{H}_2\text{O})$, card no. 43,310. The broad bumps that are observed in the pattern do not match well to any pattern from the database but may suggest a smectite-type $((\text{Ca},\text{Na})_{0.3}\text{M}_{2-3}(\text{Si},\text{Al})_4\text{O}_{10}(\text{OH})_2 \cdot n\text{H}_2\text{O})$ phase contribution. The identification of a well crystalline phase, possibly relating to a Ni-bearing phyllosilicate mineral, presented reason for EPMA analysis of this unusual specimen.



Figure 66: Pimelite.Bohemia.860

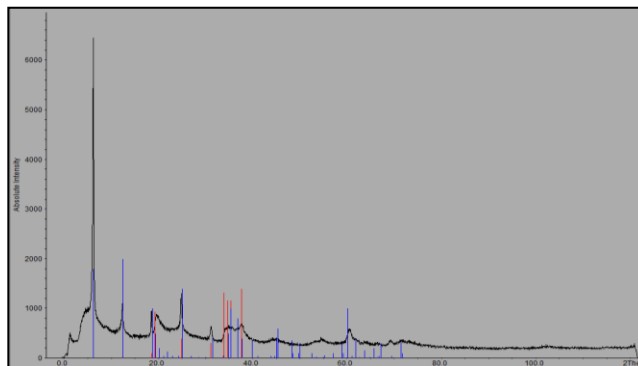


Figure 67: PXRD pattern for Pimelite.Bohemia.860 showing ICDD data for: $(\text{Ni},\text{Al})_3(\text{Al},\text{Si})_4\text{O}_{10}(\text{OH})_2 \cdot 4(\text{H}_2\text{O})$ (red, card no.43,310) and clinocllore (blue, card no. 46,1322)

BSE-imaging of this sample (see Fig. 68) showed 2 distinct major phases and some minor inclusions. The major phases are distinguished as a very fine grained material which made up the majority of the sample and a material which appears as a lighter,

larger, clearly layered phase which is dispersed in fragments throughout the sample. The minor inclusion phase occurs in only a few areas as brighter patches randomly interspersed in the fine grained material.

EPMA point analysis, for Pimelite.Bohemia.860, was acquired at 5 different areas, with a total of 40 points analysed over these areas. All of the point analysis data returned totals greater than 70% so none were discarded on this basis. The 40 points are relatively easily separated into 3 groups according to their appearance in BSE: fine grained mass (22 points), layered fragments (13 points) and inclusions (5 points). Averages and standard deviations from these groupings (see table 18) show little variation of the data and no other separation or other trends are apparent from further data manipulation.

It is clear from the “inclusion” points that these are CaO rich and the high totals indicate that there is little to no hydrous component to the material. Whilst calculations from the average data do not adequately match the stoichiometry for any mineral phase, the general composition may suggest these relate to a phase somewhere between diopside ($\text{MgCaSi}_2\text{O}_6$) and grossular ($\text{Ca}_3\text{Al}_2(\text{SiO}_4)_3$).

The “layered fragments” do not fit the stoichiometry for any mineral from calculations but it can be noted that the composition is similar to a vermiculite ($(\text{Mg,Fe,Al})_3(\text{Al,Si})_4\text{O}_{10}(\text{OH})_2 \cdot 4\text{H}_2\text{O}$) type mineral and the experimental total (av. 86.98%) is also comparable to that expected for a vermiculite type phase (82.3wt.%). FeO content in this group (av.6.49wt.%) is significantly higher than is observed in the rest of the sample. Also, NiO is observed at low but appreciable levels in this group (av. 0.79wt.%) along with TiO_2 (0.37wt.%).

The “fine grained mass” does not fit the stoichiometry of any mineral from calculations either, but it can be noted that FeO is observed at very low levels (av. 0.05wt.%) and NiO is observed at the highest level in this group, although it is still relatively low (av. 1.53wt.%). CaO is observed at higher levels (0.39wt.%) than in the layered fragments (0.09wt.%) but this may be attributable to heterogeneous mixing of very fine particles of the inclusion phase, as this level is too low even for it to be considered as occurring as an interlayer cation. This group also gives the lowest totals (av. 79.43wt%), this possibly

suggests that it is more hydrous than the layered fragments, but it is also likely that the very fine grained nature of this material will affect the totals.

With comparison to the PXRD data, although the identified vermiculite phase could not be confirmed stoichiometrically, there is some evidence that a vermiculite related phase is present as the observed layered fragments. The broad asymmetrical reflections, attributed to a possible smectite phase $((\text{Ca},\text{Na})_{0.3}\text{M}_{2-3}(\text{Si},\text{Al})_4\text{O}_{10}(\text{OH})_2 \cdot n\text{H}_2\text{O})$, could not be confirmed as smectitic from the elemental composition, however a very fine grained and hydrous material is observed as the bulk of the sample which fits the typical smectite-type description.

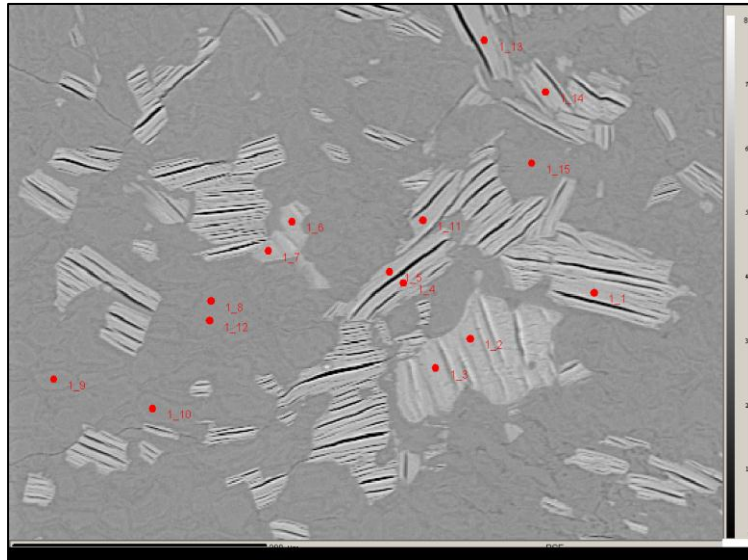


Figure 68: Sample Pimelite.Bohemia.860; Example BSE image

		MgO	Al ₂ O ₃	SiO ₂	CaO	TiO ₂	FeO	NiO	Total	Red Total	Diff
Inclusions	Av.	2.16	32.25	41.04	21.36	0.02	0.39	0.25	97.76	97.47	0.29
	Sd.	1.38	0.61	1.02	1.81	0.02	0.78	0.10	1.63	1.51	0.20
	n= 5	NiO max.	0.15	NiO min.	0.39						
Layered fragments	Av.	23.03	19.79	36.23	0.09	0.37	6.49	0.79	86.98	86.79	0.19
	Sd.	1.37	1.04	1.28	0.06	0.12	1.15	0.19	2.62	2.65	0.09
	n= 13	NiO max.	1.21	NiO min.	0.56						
Fine grained mass	Av.	21.79	18.87	36.53	0.39	0.01	0.05	1.53	79.43	79.18	0.26
	Sd.	1.92	1.96	1.48	0.06	0.01	0.05	0.13	3.48	3.47	0.08
	n= 22	NiO max.	1.73	NiO min.	1.24						

Table 18: Averages (Av.) and Standard deviations (Sd.) from EPMA point analysis of Pimelite.Bohemia.860

4.3.9. Conclusions from EPMA of Natural Materials

The benefits of using EPMA as a complementary characterisation technique to PXRD studies have been clearly demonstrated. It is a very powerful technique (especially when combined with other techniques such as PXRD) capable of: distinguishing different phases within samples (using BSE imaging); providing elemental compositions of these phases (using point analysis) which can be used to generate approximate formulae for mineral phases; and to show the relative abundances of the constituent elements (using elemental mapping).

The limitations associated with EPMA analysis have also been illustrated by these EPMA studies. While EPMA can observe minor inclusions which may not be identified from a technique such as PXRD, only a very small amount of the specimen can be analysed, so, phases that may be identified from a bulk analysis technique (e.g. PXRD) may not be

observed in the EPMA data. An example of this is clearly shown with sample B105.9.0, where while chromite inclusions were found chlorite and serpentine phases were not observed at all. The hydrous nature of these specimens causes significant problems for precise elemental determination as they are very easily altered during analysis which can skew results. Problems also arise where elements occur in more than 1 valency state (such as Fe^{2+} and Fe^{3+}) as the technique calculates figures from a predetermined oxidation state (in this case FeO) which introduces error that is not easily determined. Also very fine grained particles (such as smectite clays typically $<4\mu\text{m}$) are very hard to analyse accurately as the electron beam spot is on a similar scale ($>1\mu\text{m}$).

Ultimately this study has identified that although the 09NIC050501 and Pimelite.Bohemia.860 specimens exhibit the the most ordered crystal structures in the PXRD patterns and demonstrate some interesting silicate phases, they both have very low Ni contents. This may suggest that significantly Ni-bearing silicate phases are inherently disordered, or simply that the well ordered crystalline phases observed in these two samples do not tend to occur in the same environments as high Ni-bearing phases. CM048B.97, OR.467, CM053.97 and B105.9.0 have all shown the presence of Ni-bearing talc, with NiO up to 39.89wt.%, (implying over 70% octahedral cation substitution). Ni-bearing serpentine has also been observed in M14707 and CM048B.97, with NiO up to 48.67wt.% (implying over 85% octahedral cation substitution).

These findings highlight the importance of talc and serpentine-type minerals to the Ni-bearing hydrous silicate study. Sample M14707 also shows evidence of the formation of a diagenetic serpentine-type phase, which is unusual and merits further investigation.

The EPMA elemental mapping of OR.467, CM053.97 and M14707 have also shown evidence of Mg-Ni substitution within mineral phases as an, in-situ, solid solution; the causes of this are unknown to date, meriting further investigation.

5. Synthesis of Relevant Minerals

Parallel to the detailed characterisation study of natural mineral samples, a program of synthesis of relevant silicate phases and their characterisation has been carried out, to create a set of standards for structural and compositional comparison to natural materials.

The synthesis project can be separated into two categories: hydrous minerals, specifically serpentine-type $((\text{Ni,Mg})_3\text{Si}_2\text{O}_5(\text{OH})_4)$ and talc-type $((\text{Mg,Ni})_3\text{Si}_4\text{O}_{10}(\text{OH})_2)$ phases, synthesised via hydrothermal routes; and non-hydrous minerals, namely olivine-type $((\text{Mg,Ni,Fe})_2\text{SiO}_4)$, synthesised via high temperature methods.

5.1. Hydrous Silicate Synthesis

Characterization of the natural Ni-laterite materials, identified talc $(\text{M}_3\text{Si}_4\text{O}_{10}(\text{OH})_2)$ and serpentine $(\text{M}_3\text{Si}_2\text{O}_5(\text{OH})_4)$ as the main Ni-bearing phases in many of the ore materials. Emphasis has been placed on synthesis of these phases.

Synthesis of these minerals as single-phase materials allows them to be studied and compared to the natural materials. This improves the understanding of how nickel is incorporated in these complex systems and what affect this has on their crystallinity and stability. This is achieved by using them as a set of standards for direct comparison during structural analysis. In addition, the ease of extraction of nickel from single phase containing minerals can ascertain which is useful for mining companies that have a variety of nickel based mineral phases to choose from.

5.2. Low T and P hydrothermal synthesis

Low T and P syntheses of hydrous materials were carried out using 23ml stainless steel Teflon lined autoclaves. Various methods have been used and modified from those found in the literature describing the synthesis of relevant hydrous silicate phases. These are detailed in the following section and a summary of the reported experiments is given in Table 19.

Target Material	Starting Reagents	Conditions	Phases Identified Using PXRD (ICDD card no.)
Ni 1:1 Phyllosilicate $\text{Ni}_3\text{Si}_2\text{O}_5(\text{OH})_4$	HCl, Na_2SiO_3 , $\text{NiCl}_2 \cdot 6\text{H}_2\text{O}$, NaOH	Temp: 25°C Duration: 3d	(49-1859) Pecoraite
Ni 1:1 Phyllosilicate $\text{Ni}_3\text{Si}_2\text{O}_5(\text{OH})_4$	HCl, Na_2SiO_3 , $\text{NiCl}_2 \cdot 6\text{H}_2\text{O}$, NaOH	Temp: 250°C Duration: 6d	(49-1859) Pecoraite
Ni-serpentine $\text{Ni}_3\text{Si}_2\text{O}_5(\text{OH})_4$	Silicic acid, $\text{NiCl}_2 \cdot 6\text{H}_2\text{O}$ (3.21g), 1M NaOH (40.5ml)	Temp: 250°C Duration: 1 wk	(25-645) Chrysotile $\text{Mg}_3\text{Si}_2\text{O}_5(\text{OH})_4$
Mg-serpentine $\text{Ni}_3\text{Si}_2\text{O}_5(\text{OH})_4$	Silicic acid, $\text{MgCl}_2 \cdot 6\text{H}_2\text{O}$ (3.21g), 1M NaOH (40.5ml)	Temp: 250°C Duration: 1 wk	(25-645) Chrysotile $\text{Mg}_3\text{Si}_2\text{O}_5(\text{OH})_4$
Ni-talc $\text{Ni}_3\text{Si}_4\text{O}_{10}(\text{OH})_2$	Silicic acid (200ml), $\text{NiCl}_2 \cdot 6\text{H}_2\text{O}$ (1.07g), 1M NaOH (22.5ml)	Temp: 250°C Duration: 1 wk	(19,770) Talc $\text{Mg}_3\text{Si}_4\text{O}_{10}(\text{OH})_2$
Mg-talc $\text{Mg}_3\text{Si}_4\text{O}_{10}(\text{OH})_2$	Silicic acid (200ml), $\text{MgCl}_2 \cdot 6\text{H}_2\text{O}$ (0.92g), 1M NaOH (22.5ml)	Temp: 250°C Duration: 1 wk	(19,770) Talc $\text{Mg}_3\text{Si}_4\text{O}_{10}(\text{OH})_2$
Ni-Saponite $\text{Na}_{0.3}(\text{Ni})_3(\text{SiAl})_4\text{O}_{10}(\text{OH})_2 \cdot 4\text{H}_2\text{O}$	$\text{AlCl}_3 \cdot 6\text{H}_2\text{O}$, $\text{NiCl}_2 \cdot 6\text{H}_2\text{O}$, H_2O , NaOH, NaHCO_3 , $\text{Na}_2\text{O}(\text{SiO}_2)_x \cdot x\text{H}_2\text{O}$	Temp: 170°C Duration: 12d	(13-305) Ca Mg Fe Al silicate hydroxide hydrate/ Saponite
Interstratified Lizardite/Saponite $(\text{Mg}_3)(\text{Si,Al})_2\text{O}_5(\text{OH})_4$ / $\text{Na}_{0.3}\text{Mg}_3(\text{Si,Al})_4\text{O}_{10}(\text{OH})_2$ 1:1	$\text{AlCl}_3 \cdot 6\text{H}_2\text{O}$, $\text{MgCl}_2 \cdot 6\text{H}_2\text{O}$, H_2O , NaOH, $\text{Na}_2\text{O}(\text{SiO}_2)_x \cdot x\text{H}_2\text{O}$, HNO_3	Temp: 250°C Duration: 3d	(70-2509) Halite, (29-1491) Saponite, (25-645) Chrysotile

Table 19: Summary of low temperature and pressure synthetic materials

5.2.1 Ni 1:1 Phyllosilicate

Mizutani et al. (1990)¹⁰⁹ published a synthetic route to Ni 1:1 (serpentine type) phyllosilicates, claiming synthesis of these phases by aging a solution at room temperature. This method was tested and also modified to hydrothermal treatment of the solution at 250°C for 6 d under autogenous vapour pressure.

Method

Sodium orthosilicate (2.07g) was dissolved in 200ml of deionized water and 2M of HCl (ca.18ml) was added to make the pH of the solution 3.0, nickel chloride hexahydrate (3.21g) was dissolved in this solution. The solution was mixed slowly with 1M sodium hydroxide (40.5ml) by dropwise addition (2-4ml/min) with stirring. Half of the obtained suspension was aged for 3d at room temperature and the other half was sealed in a stainless steel, teflon lined autoclave and reacted under autogenous pressure (250°C, 6 d). The green precipitates from these experiments were washed using distilled water in a centrifuge and the final products were then dried (40°C, 18 h) and ground to give fine green powders.

Results

The PXRD patterns for the two methods of synthesis of Ni 1:1 phyllosilicates (Fig. 69) show that while the room temperature aging method forms a product that has some similarity to the ICDD data for pecoraite (card no. 49-1859) the product from the hydrothermally treated solution (6d, 250°C) exhibits a clear improvement in the crystallinity with a better match to the ICDD data.

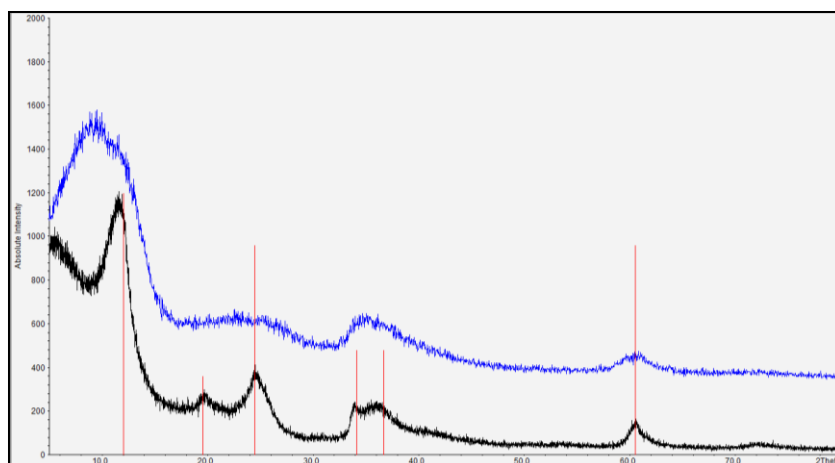


Figure 69: PXRD pattern of synthetic Ni 1:1 phyllosilicates.

ICDD data for pecoraite (red, 49-1859) Aged 3d (blue); Hydrothermal 250°C 6d (black)

5.2.2. Ni and Mg 1:1 and 2:1 Phyllosilicates

Following the synthesis of Ni 1:1 phyllosilicate via the modified Mizutani method (above), the method was then further modified to produce both the Ni and Mg end-member compositions of 1:1 (serpentine-type) silicates, as well as the Ni and Mg end-member compositions of 2:1 (talc-type) silicates.

Method

A solution of silicic acid (200ml), from sodium orthosilicate (2.07g) in distilled water, acidified with 2M HCl to pH 3 (ca.20ml), was mixed with a given amount of metal chloride hexahydrate (see table 19). 1M sodium hydroxide solution was then added to this drop-wise (ca. 1hr, see table 19 for quantity) with constant stirring. The resulting suspension was then reduced slowly to a viscous gel (ca. 50ml) by heating at 70°C, to increase product yield from the reaction. The gel was then transferred to a Teflon lined autoclave and heated to 250°C, under autogenous vapour pressure for 1wk. After cooling to room temperature, the resulting precipitate was washed with H₂O using a centrifuge, to remove residual halite (NaCl) and any other soluble impurities. The product was then dried at 60°C overnight and ground (to give a uniform polycrystalline material).

Results

PXRD patterns show the products from these syntheses match closely to ICDD data for talc (card no. 19,770) and serpentine (card no. 25,645) as well as improved crystallinity (Fig. 70). However, the observed reflections are still very broad and although the features clearly match ICDD data, these materials are still poorly crystalline which prevents any detailed structural analysis.

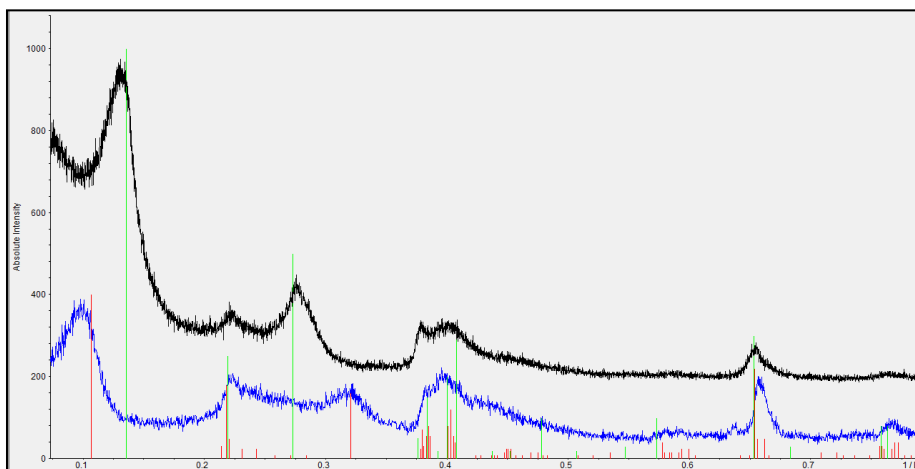


Figure 70: PXRD patterns for Ni-talc (blue) and Ni-serpentine (black), low T and P synthesis route; showing ICDD data for talc (red, card no. 19,770) and chrysotile (green, card no. 25,645)

5.2.3. Ni-Saponite

Method

The synthesis of a Ni-saponite was carried out using the technique as described by Trujillano et al. (2009)¹¹⁰. A solution of aluminium chloride hexahydrate (1.22g) and nickel chloride hexahydrate (7.27g) in water (5.0ml); was added slowly to a solution of sodium hydroxide (3.6g), sodium bicarbonate (6.56g) and sodium silicate solution (5.6ml, Na₂O ~10.6%, SiO₂ ~26.5%). The secondary mixture was sealed in a Teflon lined

stainless steel autoclave (bomb) and heated to 170°C at autogenous pressure for 12 d. The resulting product, a very fine-grained deep green solid, was washed repeatedly with distilled water and dried in an oven (40°C, 24 h).

Results

The product prepared by this method shows good correlation with the XRD patterns provided by Trujillano et al.¹¹⁰ and appears to be single phase, with no reflections observed from crystalline impurities. The product shows characteristics typical of a smectite type phase; broad asymmetrical reflections caused by high degrees of crystalline disorder and a pronounced basal reflection at around 12.4-12.5Å caused by a typically large layer spacing. The ICDD database does not hold data on a pure Ni-saponite but the pattern is comparable to that of a Ca-Mg-Fe saponite (card no. 13-305, Fig. 71), however the basal (001) reflection for the sample occurs at 12.4Å which is significantly different to the 15.38Å reflection observed for the ICDD saponite. This may be due to different interlayer species, as the variation is disproportionate to the relatively small differences in the octahedrally bound cation size. Smectite type materials are particularly susceptible to changes in layer spacing caused by humidity which may be a factor for this drift.

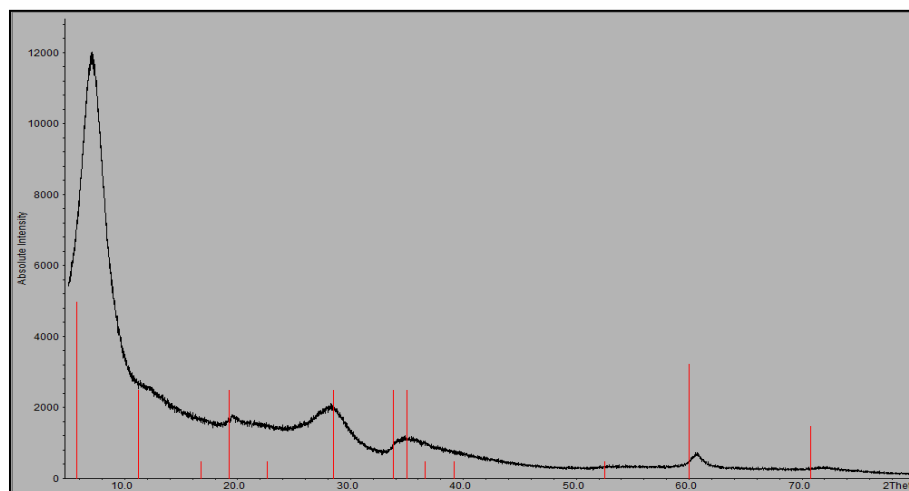


Figure 71: Powder XRD pattern of Ni-saponite showing ICDD data for Ca-Mg-Fe saponite (red).

5.2.4. Interstratified Lizardite/Saponite

Torii et al (1998)¹¹¹ published the hydrothermal synthesis of a novel interstratified lizardite/saponite material. Interstratified materials are mixtures of more than one mineral where the individual components interlayer with each other, to form a material that is a mixture of both components. As a member of the smectite group of minerals, saponite is considered relevant to this study due to the frequent observation of smectite minerals within them, especially with lizardite. The method as described by Torii involved reaction at 300°C for 2 h but due the limitations of available equipment this had to be reduced to 250°C and reaction time was extended, to 3d, to attempt to compensate for this shortcoming.

Method

A silicic acid solution was prepared by mixing water (40ml) and sodium silicate solution (6.87g, 28% SiO₂) and adding nitric acid (1.8ml, 16M). MgCl₂.6H₂O (7.11g) and AlCl₃.6H₂O (0.566g) were added to the silicic acid solution with stirring and when these had dissolved fully the solution was added dropwise to a NaOH solution (42ml, 2M) with stirring. A precipitate formed (suspension ca. pH10) which was filtered and washed. NaOH solution (2.1ml, 1M) was added to the precipitate to produce a slurry (pH ~11.5) which was consequently transferred to a stainless steel, teflon lined autoclave and reacted under autogenous pressure (250°C, 3 d). The final product was then dried (80°C, 4 h) and ground to give a fine white powder.

Results

The PXRD pattern of the product (Fig. 72) shows synthesis of a layer type silicate was achieved, to a certain degree, with a structure possibly related to those of lizardite and saponite. However, the reflections are very broad, due to poor structural order, making conclusive determination of the phases present implausible, the lack of any ICDD data for such interstratified materials also makes characterisation difficult. SEM images of the

product (Fig. 73) show a granular or globular morphology, unlike the platy morphology characteristic of the desired material. In comparison the PXRD patterns from the work of Torii et al.¹¹¹ show more ordered phases and TEM shows more platy morphology; so the reduced reaction temperature used here is likely to be limiting the crystallization process.

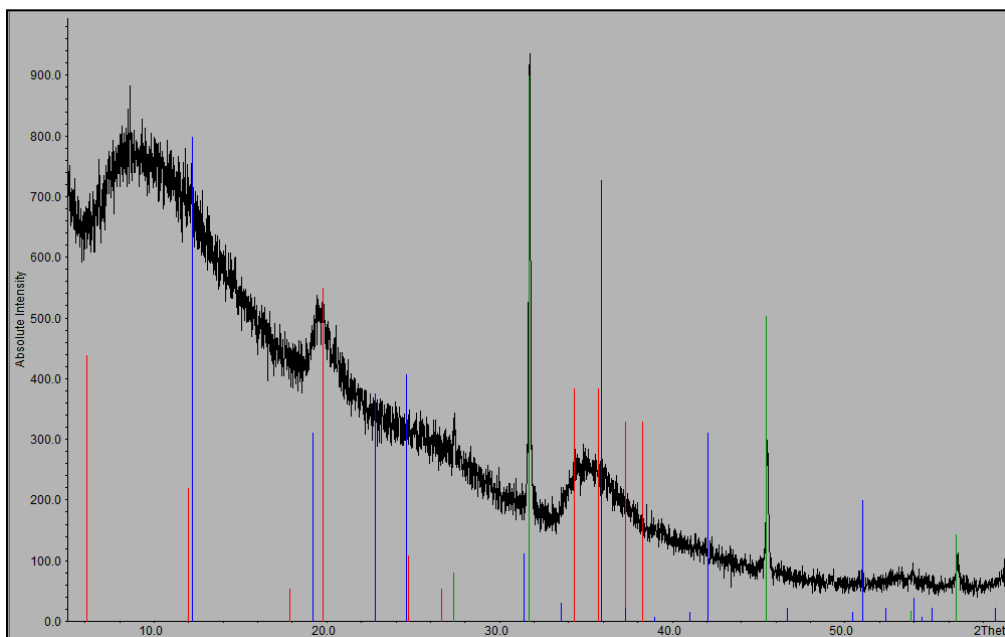


Figure 72: PXRD pattern of interstratified Lizardite/Saponite product showing ICDD data for; saponite (red), lizardite (blue), halite (green)

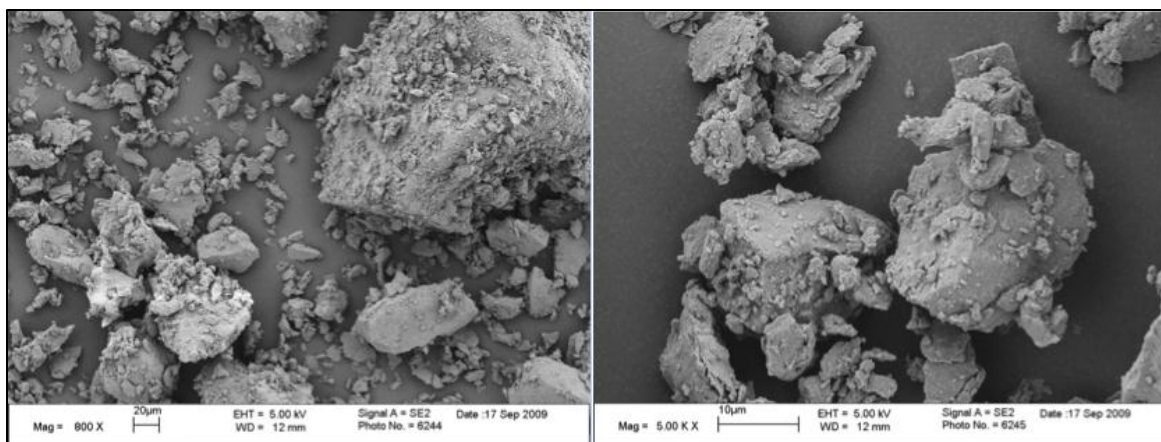


Figure 73: SEM images of powdered Interstratified Lizardite/Saponite product (collected in SEI mode).

5.3. High T and P hydrothermal synthesis

To develop the project and achieve more extreme temperature and pressure conditions for synthesis of these hydrous materials, Tuttle-type cold-seal apparatus has been used. This apparatus allows a dramatic increase in the range of reaction conditions possible. A summary of some of these materials is given in table 20.

Target Material	Starting Reagents	Conditions	Phases Identified Using PXRD (ICDD card no.)
Ni-talc $\text{Ni}_3\text{Si}_4\text{O}_{10}(\text{OH})_2$	SiO_2 , standard NiO, distilled H_2O (H_2O in excess)	Temp: 650°C Pressure: 2000bar Duration: 7d	(22-711) Willemseite- $\text{Ni}_3\text{Si}_4\text{O}_{10}(\text{OH})_2$
			(46-1045) Quartz- SiO_2
			(47-1049) NiO
Ni-talc $\text{Ni}_3\text{Si}_4\text{O}_{10}(\text{OH})_2$	SiO_2 , nano-NiO, distilled H_2O (H_2O in excess)	Temp: 650°C Pressure: 2000bar Duration: 7d	(22-711) Willemseite- $\text{Ni}_3\text{Si}_4\text{O}_{10}(\text{OH})_2$
Mg-talc $\text{Mg}_3\text{Si}_4\text{O}_{10}(\text{OH})_2$	SiO_2 , MgO, distilled H_2O (H_2O in excess)	Temp: 650°C Pressure: 2000bar Duration: 7d	(19-770) Talc- $\text{Mg}_3\text{Si}_4\text{O}_{10}(\text{OH})_2$
Ni/Mg-talc $(\text{Mg}_x\text{Ni}_{1-x})_3\text{Si}_4\text{O}_{10}(\text{OH})_2$ $x = 0.17, 0.25, 0.33, 0.50,$ $0.66, 0.75, 0.83.$	SiO_2 , MgO, nano-NiO, distilled H_2O (H_2O in excess)	Temp: 650°C Pressure: 2000bar Duration: 7d	(19-770) Talc- $\text{Mg}_3\text{Si}_4\text{O}_{10}(\text{OH})_2$
			(46-1045) Quartz- SiO_2
Ni-serpentine $\text{Ni}_3\text{Si}_2\text{O}_5(\text{OH})_4$	Silicic acid $\text{NiCl}_2 \cdot 6\text{H}_2\text{O}$ (3.21g), 1M NaOH (40.5ml)	Temp: 350°C Pressure: 1800bar Duration: 5d	(25-645) Chrysotile- $\text{Mg}_3\text{Si}_2\text{O}_5(\text{OH})_4$
			(22-711) Willemseite- $\text{Ni}_3\text{Si}_4\text{O}_{10}(\text{OH})_2$
			(5-628) Halite - NaCl
			(4-850) Ni (synthetic)

Ni-serpentine $\text{Ni}_3\text{Si}_2\text{O}_5(\text{OH})_4$	Silicic acid $\text{NiCl}_2 \cdot 6\text{H}_2\text{O}$ (3.21g), 1M NaOH (40.5ml)	Temp: 450°C Pressure: 1000bar Duration: 5d	(22-711) Willemseite- $\text{Ni}_3\text{Si}_4\text{O}_{10}(\text{OH})_2$
			(4-850) Ni, (synthetic)
			(5-628) Halite - NaCl
			(47-1049) NiO
Ni-serpentine $\text{Ni}_3\text{Si}_2\text{O}_5(\text{OH})_4$	Silicic acid $\text{NiCl}_2 \cdot 6\text{H}_2\text{O}$ (3.21g), 1M NaOH (40.5ml)	Temp: 350°C Pressure: 1000bar Duration: 5d	(25-645) Chrysotile- $\text{Mg}_3\text{Si}_2\text{O}_5(\text{OH})_4$
			(5,628) Halite - NaCl

Table 20: Summary of High temperature and pressure synthetic materials

5.3.1. Ni-Mg talc ((Ni,Mg)₃Si₄O₁₀(OH)₂)

The study of the relevant natural materials showed Ni-Mg substitution in talc-type minerals. As a result, a systematic program of synthesis of this series has been conducted to provide a set of standard samples for further characterisation.

A search of published literature on high temperature and pressure syntheses of talc-type minerals found a relatively simple method used in several studies;^{56,69,112,113} the method involves the mixture of polycrystalline oxides, in stoichiometric ratios of the composition required, followed by reaction with excess distilled H₂O at temperatures ranging from 500-800°C, pressures from 1-2kbar and durations of 48-120h. Using this method, Bowen and Tuttle (1949)¹¹² report Mg-talc synthesis at 650°C with negligible impurities and Pawley (1998)¹¹³ also reported the synthesis of near-single phase Mg-talc at 650°C and 2kbar pressure, so these conditions were used as a basis for synthesis here.

Method

Nickel-magnesium talc samples were synthesized using high-pressure hydrothermal methods from the constituent metal oxides. Starting reagents used throughout the synthesis were; -325 mesh SiO₂ powder (Sigma-Aldrich UK, 342890); -325 mesh MgO powder (Sigma-Aldrich UK, 342793), NiO powder prepared in-house after the method by Li et al. (2008) and distilled H₂O. Synthesized nano-particulate NiO powder (“nano-NiO”^{**}) was used to prepare the talc samples in preference to standard grade -325 mesh green NiO powder (Sigma-Aldrich UK, 399523) (see PXRD comparison in Fig. 74), as preliminary experiments showed it to significantly improve the rate of formation of the Ni-talcs and significantly reduced unreacted impurities (see table 20). Stoichiometric quantities of the SiO₂, MgO and “nano-NiO” to give the desired composition of Mg/Ni talc (c. 1.5-2g) were ground using a pestle and mortar^{1**} and in sealed gold tube, using

^{**} This NiO material is referred to as “nano” as this was determined in the publication where the preparation method was found⁶⁷, actual particle size has not been determined here.

^{**}Ball-milling of the starting reagents in an agate ball mill (ca. 3hr) was tried to improve the crystalline order and/or rate of crystallization but no noticeable improvement was observed from PXRD data of final products so this step was not continued.

an arc welder, with excess distilled H₂O. The capsules of starting materials were then reacted (650°C, 2kbar, 7d) to produce mostly single phase talc-type materials. Samples were washed from the Au-capsule using distilled H₂O and dried at 100°C overnight.

In total, 9 compositions through the Ni/Mg-talc series were prepared:

(Mg_xNi_{1-x})₃Si₄O₁₀(OH)₂ where x equals: 0; 0.17; 0.25; 0.33; 0.50; 0.66; 0.75; 0.8; 1.

The samples were then analysed using powder X-ray diffraction (PXRD), thermogravimetric analysis (TGA), infra-red spectroscopy (IR) and Raman spectroscopy.

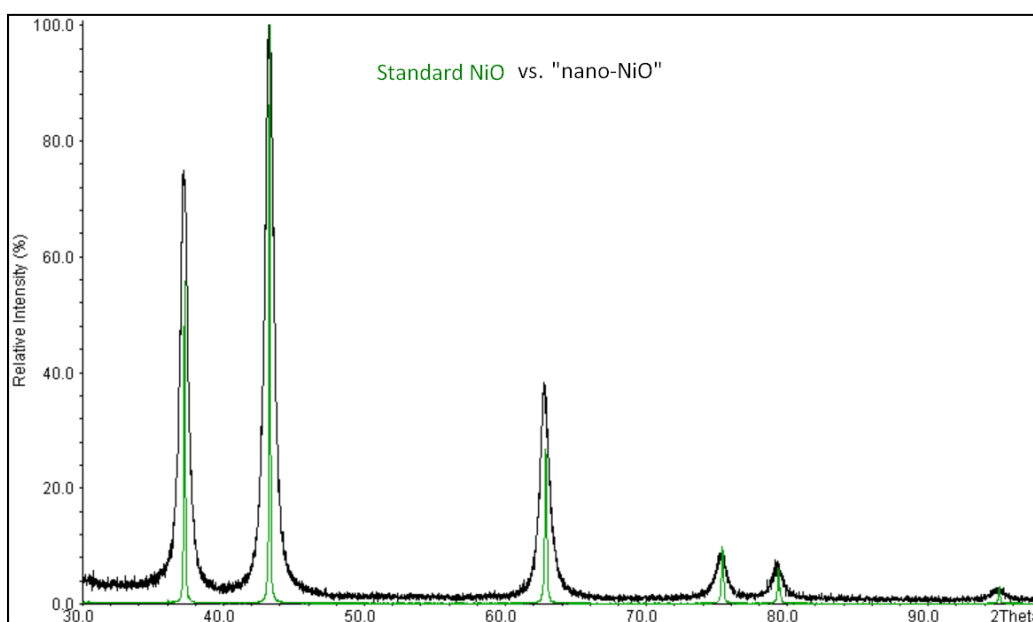


Figure 74: PXRD comparison of nano-NiO (black) and standard NiO (green)

Results

Comparison of PXRD data acquired for Ni-talc synthesized via the low temperature and pressure gel method, to the Ni-talc synthesized from the high temperature and pressure oxide-mix method (Fig. 75) shows a dramatic improvement in crystallinity; with a huge reduction in the half-width of the reflections and clearer definition of characteristic reflections.

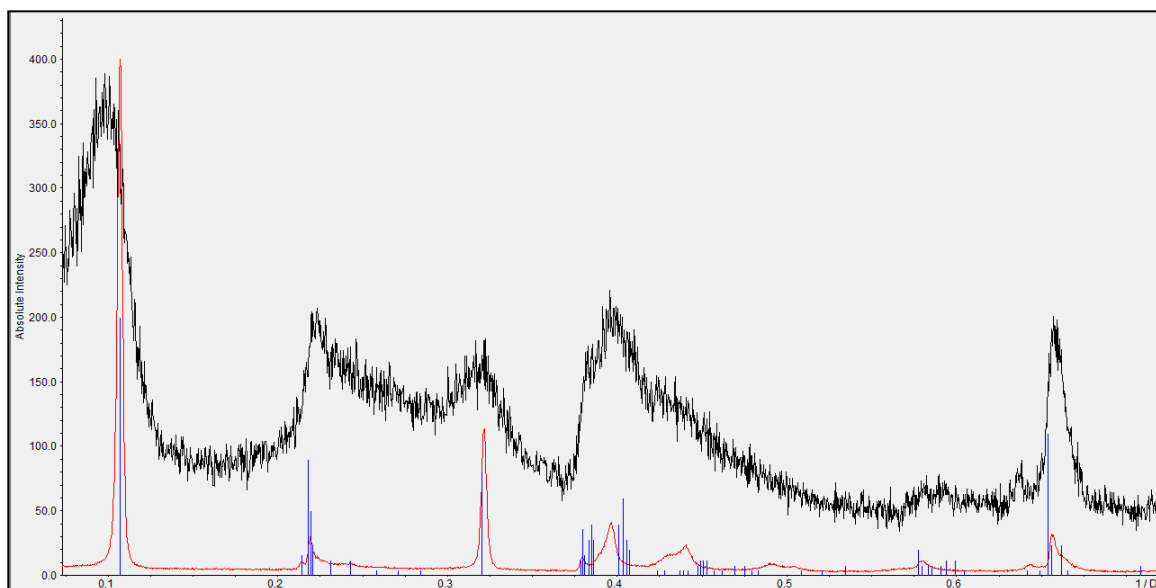


Figure 75: PXRD comparison of synthetic Ni-talcs: Low T & P route (black); High T & P route (red); ICDD data for talc (blue, card no. 19,770)

Analysis of the PXRD patterns show the successful formation of talc type materials across the Mg-Ni compositional series, with a good match to the ICDD data of talc (Fig. 76). Quartz (SiO_2 , card no. 46,1045) is also observed as a trace component in most experiments. As substitution of Ni for tetrahedral Si can be discounted the quartz impurity is likely to be un-reacted starting material. The talc phases show sharp $00l$ reflections indicating an ordered structure along the c -axis, as described by Ferrage et al. (2006⁶⁷). Ni-substitution results in a more poorly crystalline material, often observed in Ni-containing materials. A complete solid solution: $(\text{Mg}_x, \text{Ni}_{3-x})\text{Si}_4\text{O}_{10}(\text{OH})_2$, $0 < x < 1$, is observed. Comparison of the $00l$ reflection positions of Ni and Mg diffraction patterns shows a difference of $\approx 0.03\text{\AA}$ in the d-spacings. This difference is large enough that asymmetry or splitting of this reflection would be observed if phases were mixed.

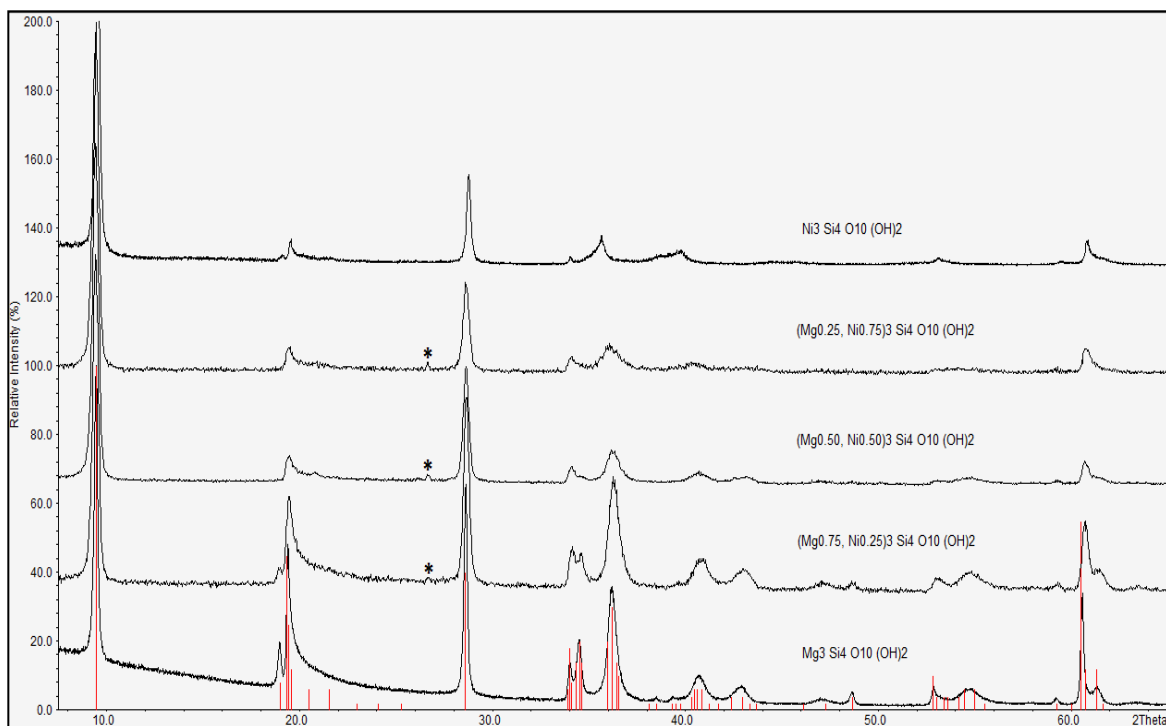


Figure 76: PXRD patterns for synthetic Mg-Ni talc series, from bottom to top:

$(\text{Mg}_3\text{Si}_4\text{O}_{10}(\text{OH})_2)$; $(\text{Mg}_{0.75}\text{Ni}_{0.25})_3\text{Si}_4\text{O}_{10}(\text{OH})_2$; $(\text{Mg}_{0.50}\text{Ni}_{0.50})_3\text{Si}_4\text{O}_{10}(\text{OH})_2$;
 $(\text{Mg}_{0.25}\text{Ni}_{0.75})_3\text{Si}_4\text{O}_{10}(\text{OH})_2$; $\text{Ni}_3\text{Si}_4\text{O}_{10}(\text{OH})_2$; ICDD data for talc (red, card no. 19,770)
 and SiO_2 trace impurity reflection marked with *.

Unit cell parameters were refined in the space group $C-1$, over the 2θ range $5-80^\circ$, and are presented in table 21. In order to model the structural disorder of these phases, which results in the broadening of certain reflections, spherical harmonics¹¹⁴ were included in the refinement (Fig. 77). Unit cell parameters are comparable to those reported by Perdikatsis and Burzlaff⁵⁴, which were refined from single crystal X-ray Diffraction data. Differences between the refined cell parameters of this study compared to that of Perdikatsis and Burzlaff⁵⁴ are not only due to data being collected on powder samples rather than single crystals, but also as the samples under investigation are clearly disordered and the model used in the single crystal refinements assumed ordered stacking.

Trends in unit cell parameters as a function of cation substitutions are often observed in solid solutions, such as the Ni-Mg olivine $((\text{Mg},\text{Ni})_2\text{SiO}_4)$ series¹¹⁵. No systematic trends

are observed with any unit cell parameters as a function of Ni substitution in the synthetic samples (see Appendices 1-7) studied here. The subtle changes in the unit cell parameters may be due to the ionic radii of Ni^{2+} and Mg^{2+} being similar (Mg^{2+} 0.72Å, Ni^{2+} 0.69Å) as well as the disordered nature of these samples, this makes accurate modelling of the crystal structure difficult using powder XRD techniques.

Composition	a (Å)	b (Å)	c (Å)	α (°)	β (°)	γ (°)	vol. (Å ³)
$\text{Ni}_3\text{Si}_4\text{O}_{10}(\text{OH})_2$	5.316(4)	9.126(6)	9.387(6)	92.33(5)	97.51(4)	90.27(5)	451.1
$(\text{Ni}_{0.83},\text{Mg}_{0.17})_3\text{Si}_4\text{O}_{10}(\text{OH})_2$	5.271(3)	9.153(2)	9.485(1)	91.48(2)	98.92(3)	89.88(2)	451.9
$(\text{Ni}_{0.75},\text{Mg}_{0.25})_3\text{Si}_4\text{O}_{10}(\text{OH})_2$	5.318(9)	9.05(1)	9.451(3)	92.6(1)	97.07(8)	90.26(1)	450.9
$(\text{Ni}_{0.66},\text{Mg}_{0.33})_3\text{Si}_4\text{O}_{10}(\text{OH})_2$	5.313(2)	9.1(3)	9.4426(8)	92.60(3)	96.88(2)	90.18(3)	452.8
$(\text{Ni}_{0.50},\text{Mg}_{0.50})_3\text{Si}_4\text{O}_{10}(\text{OH})_2$	5.309(5)	9.08(3)	9.454(2)	92.5(1)	97.11(9)	90.15(4)	451.8
$(\text{Ni}_{0.33},\text{Mg}_{0.66})_3\text{Si}_4\text{O}_{10}(\text{OH})_2$	5.279(9)	9.085(3)	9.488(6)	91.14(3)	99.05(2)	89.86(2)	449.3
$(\text{Ni}_{0.25},\text{Mg}_{0.75})_3\text{Si}_4\text{O}_{10}(\text{OH})_2$	5.273(3)	9.119(4)	9.469(1)	91.35(3)	98.65(4)	89.87(2)	450.0
$(\text{Ni}_{0.17},\text{Mg}_{0.83})_3\text{Si}_4\text{O}_{10}(\text{OH})_2$	5.264(1)	9.066(2)	9.4255(8)	90.80(2)	99.02(2)	89.98(1)	444.2
$\text{Mg}_3\text{Si}_4\text{O}_{10}(\text{OH})_2$	5.29(3)	9.129(2)	9.434(2)	91.94(2)	97.76(2)	90.21(2)	451.1
<i>Lit. data $\text{Mg}_3\text{Si}_4\text{O}_{10}(\text{OH})_2$</i>	<i>5.29(3)</i>	<i>9.173(5)</i>	<i>9.46(5)</i>	<i>90.46(5)</i>	<i>98.68(5)</i>	<i>90.09(5)</i>	<i>453.77</i>

Table 21: Refined unit cell parameters for synthetic Mg/Ni-talc compositions.

Lit. data for talc ($\text{Mg}_3\text{Si}_4\text{O}_{10}(\text{OH})_2$) as determined by Perdikatsis & Burzlaff (1981⁵⁴).
Individual plots for these parameters given in Appendices 1-7.

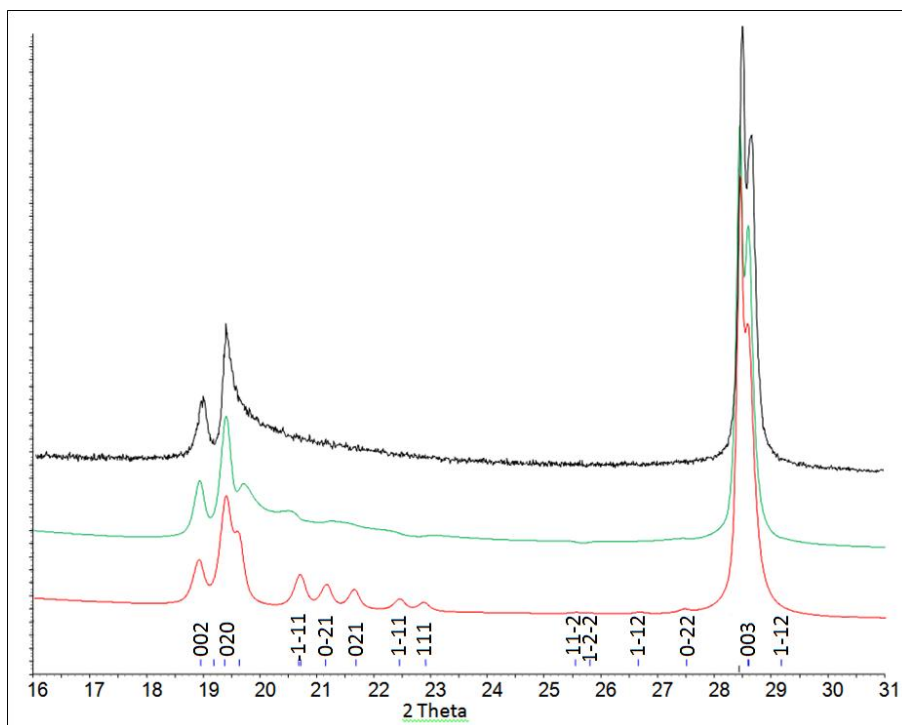


Figure 77: Illustration of the effect of spherical harmonics for modelling disorder in the structural refinement of these phases. Experimental PXRD pattern for Ni-talc (black); Pattern refined using spherical harmonics (green); Pattern refined without spherical harmonics (red), hkl tick marks (blue).

Thermal Analysis

TGA data for all compositions show a single weight-loss step, between 700°C and 1000°C, of 3.7-4.7%, with a corresponding transition in the DTA curve (see Fig. 78 and table 22). This agrees well with the thermal decomposition of talc⁶⁵. The reported mechanism of dehydroxylation as the loss of constitutional water ($M_3Si_4O_{10}(OH)_2 = M_3Si_4O_{11} + H_2O$) followed by recrystallization of the products silica (SiO_2), olivine (M_2SiO_4) and enstatite ($MSiO_3$). The observed weight losses match very closely to calculated weight losses (>90%) across the full compositional range, implying good sample purity. It can also be noted no endothermic transition is observed near 573°C, which would correspond to a quartz α - β inversion, therefore it is suggested that SiO_2 must be a trace impurity of less than 5wt.%.¹¹⁶ The data also show Ni substitution correlates with an enhancement in the thermal stability of the synthetic samples, as

weight-loss maxima temperatures for the dehydroxylation step increase by c.60°C between the end-members (see Fig. 79). This is in contradiction to that reported in the review paper by Wesolowski⁸¹ that states the thermal stabilities of Ni and Mg containing talc are the same due to their cation sizes. However, Wesolowski⁸¹ does not refer to any experimental evidence, so this statement may be simply an assumption based on the similarities of the cation sizes of Mg^{2+} and Ni^{2+} . Additionally, while a reduction in crystallinity has been shown to reduce thermal stability⁴⁷ the Ni-substituted talcs show increased stability even though the PXRD data suggests they are more poorly crystalline, indicating that the effect is not related to crystallinity or particle size.

PXRD data collected on the products after TGA has been carried out show the phases formed are different dependent upon the starting composition of the talc phase. The data show an enstatite-type phase (MgSiO_3 , ICDD card no. 19-768) and NiO present in the Ni-end-member product, more complex mixtures of quartz, Ni/Mg-oxides, enstatite and olivine-type phases from the mixed Ni/Mg compositions and enstatite, forsterite (Mg-olivine) and quartz observed in the Mg-talc (table 22).

To date, there are no published studies into the thermal stability of Ni-substituted talcs, however, it is known that Ni-enstatite (NiSiO_3) should be unstable at pressures of 1 atm. forming Ni-olivine (Ni_2SiO_4) with SiO_2 with the presence of Mg allowing the formation of equilibrium between Ni/Mg-olivine and Ni/Mg-enstatite with cation partitioning dependent on formation conditions.¹¹⁷

Conversely this study found enstatite is identified in all the PXRD patterns of the talc TGA products, with olivine reflections reducing in intensity as Ni-substitution increases. This, coupled with the identification of enstatite from PXRD of the Ni-end-member TGA product, with a non-stoichiometric absence of quartz and excess of NiO ($\text{Ni}_3\text{Si}_4\text{O}_{10}(\text{OH})_2 - \text{H}_2\text{O} = 3\text{NiSiO}_3 + \text{SiO}_2$), highlights an area for further investigation.

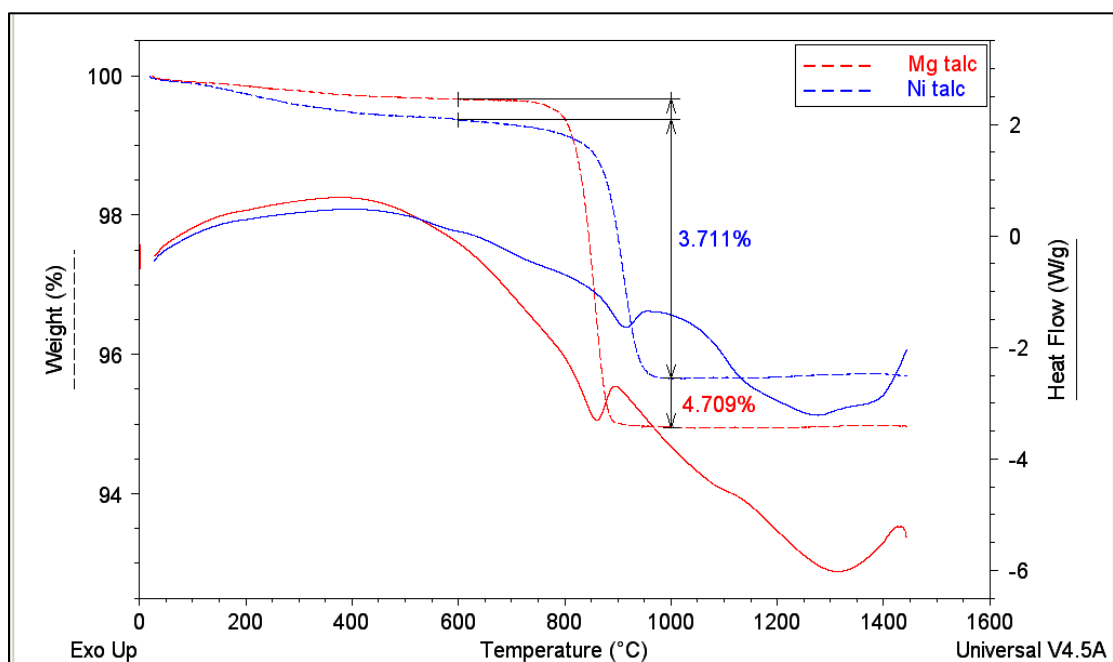


Figure 78: TGA-DTA curves for $\text{Ni}_3\text{Si}_4\text{O}_{10}(\text{OH})_2$ (blue) and $\text{Mg}_3\text{Si}_4\text{O}_{10}(\text{OH})_2$ (red): weight(%) shown as dashed line, heat-flow shown as solid line.

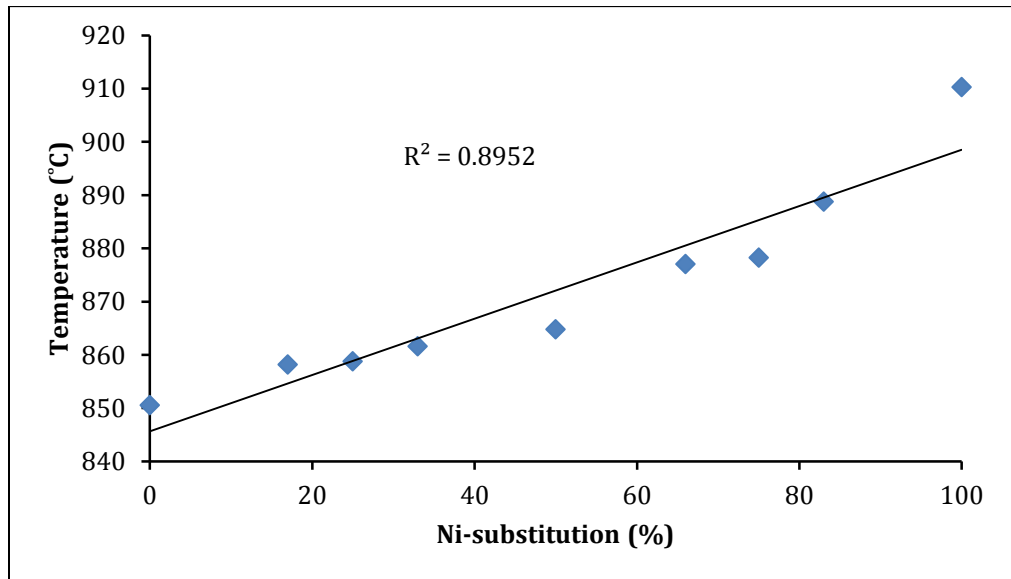


Figure 79: N_2 TGA: Thermal stability of synthetic Ni-doped talcs $(\text{Ni,Mg})_3\text{Si}_4\text{O}_{10}(\text{OH})_2$. Temperature of dehydroxylation weight-loss maxima ($^{\circ}\text{C}$) vs. Ni-substitution (%).

Composition	Calc. Wt. Loss (%)	Obs. Wt. Loss (%)	Wt. loss maxima (°C)	PXRD Phase ID (ICDD card no.)
$\text{Ni}_3\text{Si}_4\text{O}_{10}(\text{OH})_2$	3.73	3.71	910	Enstatite (19,768) NiO (47,1049)
$(\text{Ni}_{0.83}, \text{Mg}_{0.17})_3\text{Si}_4\text{O}_{10}(\text{OH})_2$	3.87	3.63	889	N/A
$(\text{Ni}_{0.75}, \text{Mg}_{0.25})_3\text{Si}_4\text{O}_{10}(\text{OH})_2$	3.95	3.65	878	Enstatite (19,768) Olivine (34,189) Quartz (46,1045) (Ni,Mg)O (24,712)
$(\text{Ni}_{0.66}, \text{Mg}_{0.33})_3\text{Si}_4\text{O}_{10}(\text{OH})_2$	4.02	4.00	877	N/A
$(\text{Ni}_{0.50}, \text{Mg}_{0.50})_3\text{Si}_4\text{O}_{10}(\text{OH})_2$	4.18	3.83	865	Enstatite (19,768) Olivine (34,189) Quartz (46,1045) (Ni,Mg)O (24,712)
$(\text{Ni}_{0.33}, \text{Mg}_{0.66})_3\text{Si}_4\text{O}_{10}(\text{OH})_2$	4.36	4.17	862	N/A
$(\text{Ni}_{0.25}, \text{Mg}_{0.75})_3\text{Si}_4\text{O}_{10}(\text{OH})_2$	4.45	4.26	859	Enstatite (19,768) Olivine (34,189) Quartz (46,1045) (Ni,Mg)O (24,712)
$(\text{Ni}_{0.17}, \text{Mg}_{0.83})_3\text{Si}_4\text{O}_{10}(\text{OH})_2$	4.54	4.23	858	N/A
$\text{Mg}_3\text{Si}_4\text{O}_{10}(\text{OH})_2$	4.75	4.71	851	Enstatite (19,768) Olivine (34,189) Quartz (46,1045)

Table 22: Thermal analysis results. Weight loss calculated as loss of H₂O from composition, observed weight loss calculated between 700-1000°C, weight loss maxima are calculated as the mid-point of the weight-loss step.

Vibrational Spectroscopy

Previous reports on Ni-doped talc phases have used infra-red spectroscopy to study the effect of cation substitution on hydroxyl vibrations,^{68,80} specifically the splitting and relative intensities of the resulting OH-vibrations. Infra-red spectroscopy of the Ni/Mg-talc series reported here in the OH-stretching region show good correlation with previous reports both experimental⁶⁸ and theoretical⁸⁰ (see Fig. 80, table 23 and table 24).

The occurrence and distribution of the 4 observed bands in the OH-stretching region are reported to show random octahedral cation substitution, without any site preference in the structure¹¹⁸.

Raman spectra were also collected. Raman spectroscopy allows reduced vibrational bandwidths compared to IR spectroscopy (c. $<10\text{cm}^{-1}$ compared to c. $>10\text{cm}^{-1}$) and therefore improved resolution. The Raman spectra show a direct correlation with the IR spectra (Fig. 81 and table 26) with the same OH-stretching band characteristics observed.

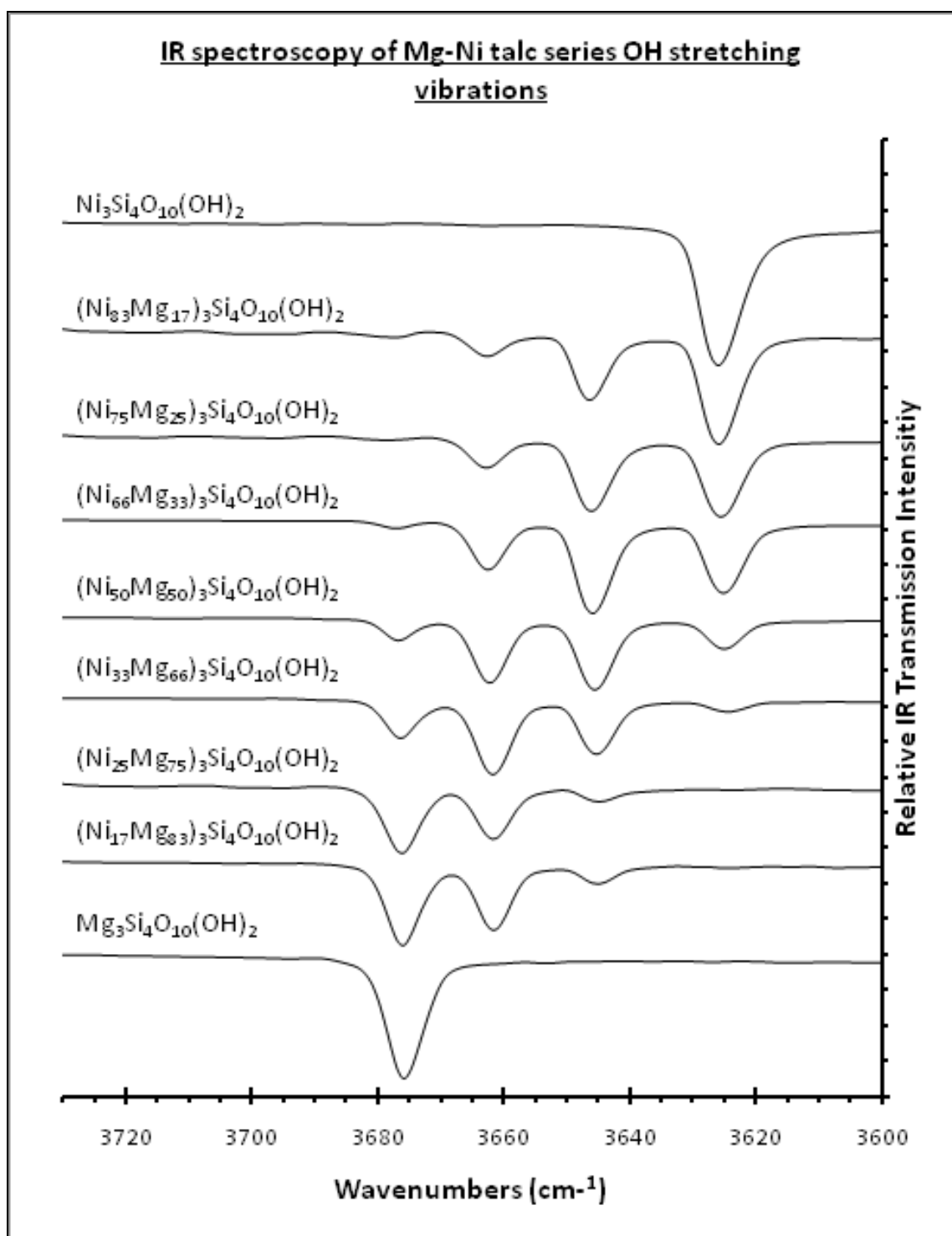


Figure 80: IR spectra for the 9 samples, showing OH-stretch region at $3600\text{-}3700\text{cm}^{-1}$.

Composition		IR OH-stretch Frq. (cm ⁻¹) close to -			
		Ni,Ni,Ni	Ni,Ni,Mg	Ni,Mg,Mg	Mg,Mg,Mg
Exp. Data	Ni ₃ Si ₄ O ₁₀ (OH) ₂	3626	-	-	-
	(Ni _{0.83} ,Mg _{0.17}) ₃ Si ₄ O ₁₀ (OH) ₂	3626	3646.4	3663	3677.9
	(Ni _{0.75} ,Mg _{0.25}) ₃ Si ₄ O ₁₀ (OH) ₂	3625.7	3646.2	3663	3677.5
	(Ni _{0.66} ,Mg _{0.33}) ₃ Si ₄ O ₁₀ (OH) ₂	3625.2	3646	3662.7	3677.2
	(Ni _{0.50} ,Mg _{0.50}) ₃ Si ₄ O ₁₀ (OH) ₂	3625.1	3645.7	3662.4	3676.9
	(Ni _{0.33} ,Mg _{0.66}) ₃ Si ₄ O ₁₀ (OH) ₂	3624.6	3645.4	3662.4	3676.6
	(Ni _{0.25} ,Mg _{0.75}) ₃ Si ₄ O ₁₀ (OH) ₂	3624.5	3645	3661.8	3676.3
	(Ni _{0.17} ,Mg _{0.83}) ₃ Si ₄ O ₁₀ (OH) ₂	3624.5	3645.1	3661.7	3676.1
	Mg ₃ Si ₄ O ₁₀ (OH) ₂	-	-	-	3676
Lit. data	(Ni _{0.99} ,Mg _{0.01}) ₃ Si ₄ O ₁₀ (OH) ₂	3627.2	3646.9	-	-
	(Ni _{0.77} ,Mg _{0.23}) ₃ Si ₄ O ₁₀ (OH) ₂	3627.2	3646.2	3662.9	3676.7
	(Ni _{0.48} ,Mg _{0.52}) ₃ Si ₄ O ₁₀ (OH) ₂	3625.9	3645.9	3662.5	3676.5
	(Ni _{0.24} ,Mg _{0.76}) ₃ Si ₄ O ₁₀ (OH) ₂	3625	3645.2	3662.3	3676.6
	(Ni _{0.16} ,Mg _{0.84}) ₃ Si ₄ O ₁₀ (OH) ₂	-	3644.8	3661.9	3676.5
	Mg ₃ Si ₄ O ₁₀ (OH) ₂	-	-	-	3676.6

Table 23: IR data: Experimental vs. Literature OH-stretching bands.

Literature data from Wilkins & Ito⁶⁸ (Lit. data).

Composition		IR Intensity Ratio of OH-stretch close to:			
		Ni,Ni,Ni	Ni,Ni,Mg	Ni,Mg,Mg	Mg,Mg,Mg
Exp. Data	$\text{Ni}_3\text{Si}_4\text{O}_{10}(\text{OH})_2$	100	-	-	-
	$(\text{Ni}_{0.83},\text{Mg}_{0.17})_3\text{Si}_4\text{O}_{10}(\text{OH})_2$	55	33	11	1
	$(\text{Ni}_{0.75},\text{Mg}_{0.25})_3\text{Si}_4\text{O}_{10}(\text{OH})_2$	43	40	16	0
	$(\text{Ni}_{0.66},\text{Mg}_{0.33})_3\text{Si}_4\text{O}_{10}(\text{OH})_2$	33	42	22	3
	$(\text{Ni}_{0.50},\text{Mg}_{0.50})_3\text{Si}_4\text{O}_{10}(\text{OH})_2$	16	38	35	11
	$(\text{Ni}_{0.33},\text{Mg}_{0.66})_3\text{Si}_4\text{O}_{10}(\text{OH})_2$	6	30	42	21
	$(\text{Ni}_{0.25},\text{Mg}_{0.75})_3\text{Si}_4\text{O}_{10}(\text{OH})_2$	2	10	38	49
	$(\text{Ni}_{0.17},\text{Mg}_{0.83})_3\text{Si}_4\text{O}_{10}(\text{OH})_2$	2	11	39	48
	$\text{Mg}_3\text{Si}_4\text{O}_{10}(\text{OH})_2$	-	-	-	100
Theo. data	$(\text{Ni}_{0.99},\text{Mg}_{0.01})_3\text{Si}_4\text{O}_{10}(\text{OH})_2$	97	3	-	-
	$(\text{Ni}_{0.77},\text{Mg}_{0.23})_3\text{Si}_4\text{O}_{10}(\text{OH})_2$	44	43	11	1.5
	$(\text{Ni}_{0.48},\text{Mg}_{0.52})_3\text{Si}_4\text{O}_{10}(\text{OH})_2$	13	35	35	17
	$(\text{Ni}_{0.24},\text{Mg}_{0.76})_3\text{Si}_4\text{O}_{10}(\text{OH})_2$	2	11	43.5	43.5
	$(\text{Ni}_{0.16},\text{Mg}_{0.84})_3\text{Si}_4\text{O}_{10}(\text{OH})_2$	1	12	24	63

Table 24: IR data: Experimental vs. Theoretical intensity ratios of OH bands.

Theoretical data from Scholtzova et al.⁸⁰ (Theo. data).

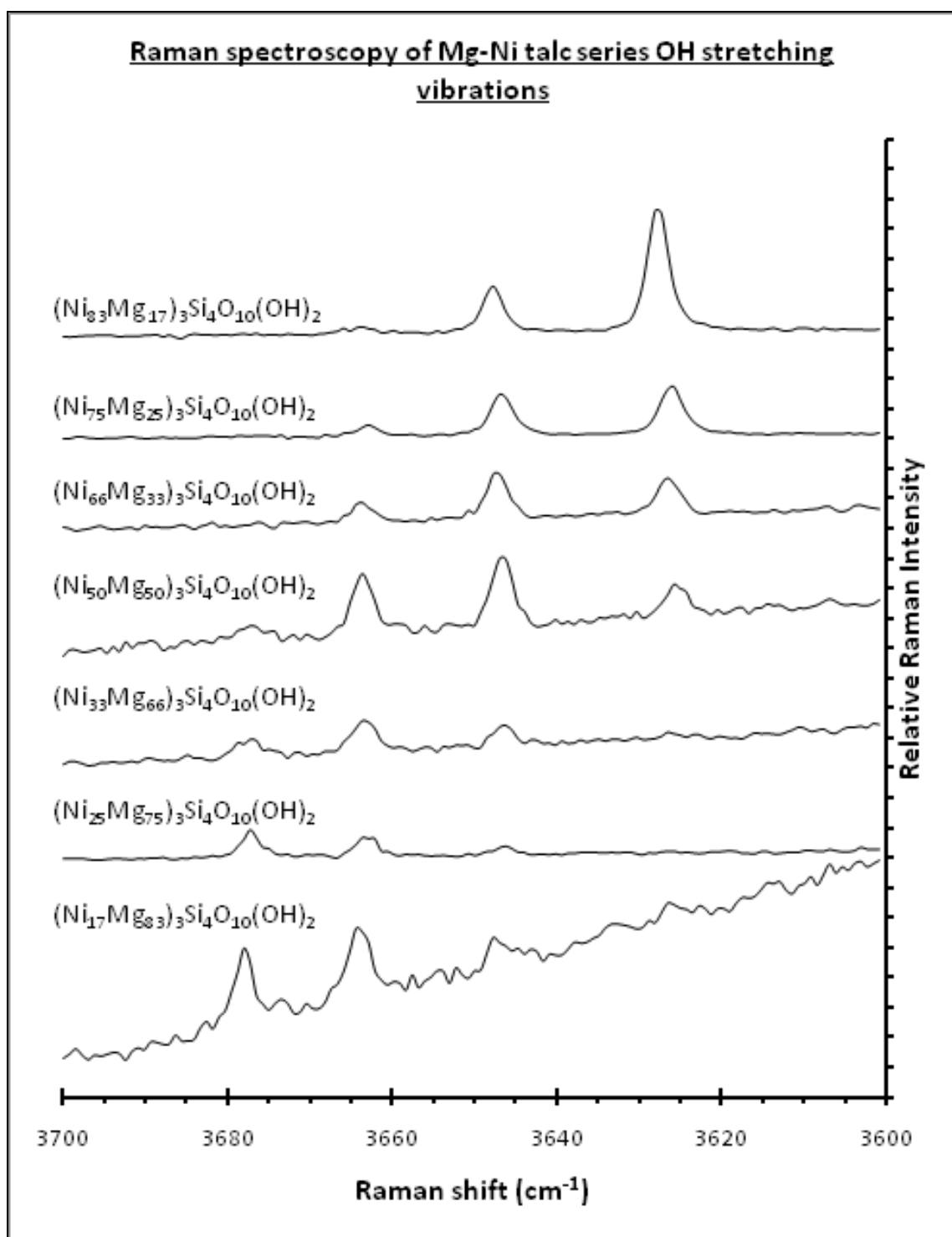


Figure 81: Raman spectra showing the OH-stretching region at $3600\text{-}3700\text{cm}^{-1}$ for the 7 intermediate Ni/Mg compositions.

Composition	Raman OH ion vibrational Frq. (cm ⁻¹) close to:			
	Ni,Ni,Ni	Ni,Ni,Mg	Ni,Mg,Mg	Mg,Mg,Mg
Ni ₃ Si ₄ O ₁₀ (OH) ₂	3625.9	-	-	-
(Ni _{0.83} ,Mg _{0.17}) ₃ Si ₄ O ₁₀ (OH) ₂	3628.0	3647.7	3663.6	-
(Ni _{0.75} ,Mg _{0.25}) ₃ Si ₄ O ₁₀ (OH) ₂	3625.2	3646.6	3662.6	-
(Ni _{0.66} ,Mg _{0.33}) ₃ Si ₄ O ₁₀ (OH) ₂	3626.0	3646.6	3663.4	-
(Ni _{0.50} ,Mg _{0.50}) ₃ Si ₄ O ₁₀ (OH) ₂	3625.3	3646.4	3663.0	3676.5
(Ni _{0.33} ,Mg _{0.66}) ₃ Si ₄ O ₁₀ (OH) ₂	3626.0	3645.8	3663.4	3677.1
(Ni _{0.25} ,Mg _{0.75}) ₃ Si ₄ O ₁₀ (OH) ₂	-	3645.8	3663.4	3677.1
(Ni _{0.17} ,Mg _{0.83}) ₃ Si ₄ O ₁₀ (OH) ₂	-	3647.3	3664.1	3677.9
Mg ₃ Si ₄ O ₁₀ (OH) ₂	-	-	-	3677.0

Table 26: Raman spectra bands.

5.3.2. Ni-serpentine (Ni₃Si₂O₅(OH)₄)

Method

The synthetic method reported for the low temperature and pressure synthesis of serpentine-type phases from a gel, has been adapted for the use with the high temperature and pressure apparatus to improve resulting product crystallinity.

A solution of silicic acid (200ml) from sodium orthosilicate (2.07g) in distilled water, acidified with 2M HCl to pH.3 (ca.20ml) was mixed with nickel chloride hexahydrate (3.21g). 1M sodium hydroxide solution (40.5ml) was then added to this, drop-wise (ca. 1hr) with constant stirring. The resulting suspension was reduced slowly to a viscous gel (ca. 30ml) by heating at 70°C, to increase product yield from the reaction. Some of this gel (ca. 1g) was sealed in a welded Au capsule for hydrothermal reaction. Reaction temperatures and pressures were tried at 350°C and 450°C, at pressures of 1kbar and 1.8kbar, with reaction times of 5d. Due to the small amount of sample acquired from the gel, products were not washed to prevent loss of desired material. The product was then dried at 60°C overnight and ground (to give a uniform polycrystalline material).

Samples were then analysed using powder X-ray diffraction (PXRD).

Results

Products synthesised above 350°C and 1kbar showed presence of impurities including willemseite (Ni-talc, $\text{Ni}_3\text{Si}_4\text{O}_{10}(\text{OH})_2$) and Ni-metal in PXRD patterns (see table 20). This indicates that at or below these conditions the formation of serpentine becomes unstable preventing the synthesis of a single-phase material. Further investigation of these conditions and/or phase diagrams would be required to determine the uppermost limits of single-phase synthesis.

Synthesis carried out at 350°C and 1kbar produced the best quality sample (see Fig. 82), which gave a serpentine phase (and NaCl halite, which remained because the product was not washed). Comparison of PXRD data of this sample with that of the low temperature and pressure synthetic Ni-serpentine shows marked improvement in crystallinity via this modified route, with a clear reduction in the width of the reflections (Fig. 82). However, the reflections are still too broad to allow further structural analysis to be achieved.

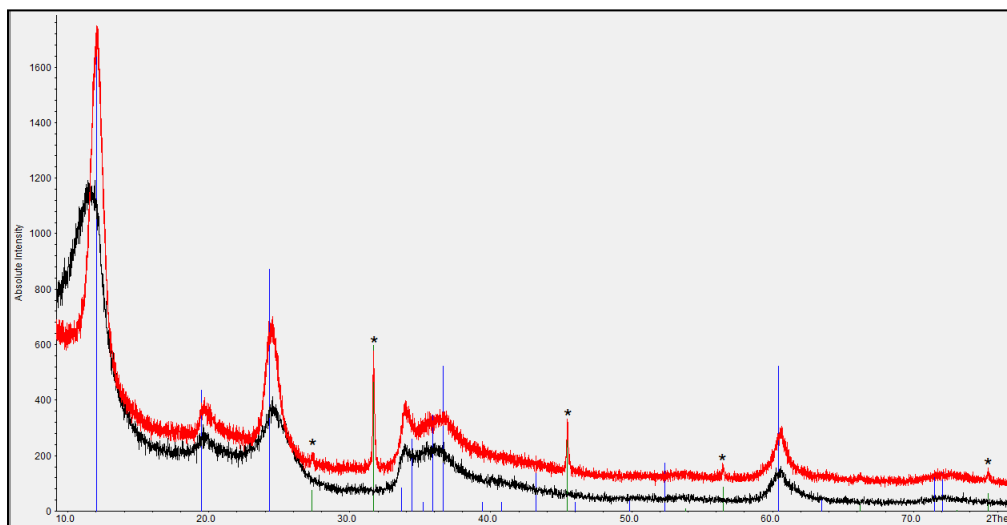


Figure 82: PXRD comparison of synthetic Ni-serpentines:

Low T & P (black); High T & P (red);

ICDD data: chrysotile (blue, card no. 25,645), halite (green and *, card no. 5,628)

5.4. Non-Hydrous Silicate Synthesis

Lateritic Ni-bearing hydrous silicates minerals (such as serpentine and talc) are formed naturally through metamorphic alteration by hydrothermal weathering of parent rocks. These parent rocks are composed mostly of non-hydrous silicate minerals, which, depending on the weathering profile of a laterite zone, can also be found dispersed in the hydrous-materials. Thus, synthetically studying these non-hydrous minerals can lead to better understanding of the hydrous phases.

Peridotite, an igneous rock material, is the most common parent rock type related with lateritic Ni-bearing hydrous silicates. It is rich in olivine group minerals ($(\text{Mg,Fe,Ni})_2\text{SiO}_4$), peridot being the name given to gem quality Mg-olivine. The olivine group of minerals exist as a solid solution series between divalent cations; Ni, Mg and Fe, forming the respective end-members liebenbergite, forsterite and fayalite. Synthesis of these phases has been attempted to provide some understanding of hydrous silicate formation by hydrothermal reaction of these materials and for comparison to dehydration products of hydrous phases. A summary of the synthetic materials is given in table 27.

Target Material	Starting Reagents	Conditions	Phases Identified Using PXRD (ICDD card no.)	Formula from EPMA
Ni ₂ SiO ₄	NiO SiO ₂	Method 1. Alumina crucible, 4d, 1400°C, 4 grinding stages with a pestle and mortar	(15,388) Liebenbergite Ni ₂ SiO ₄	N/A
			(35,610) Enstatite MgSiO ₃	
			(47,1049) Bunsenite NiO	
Ni ₂ SiO ₄	NiO SiO ₂	Method 2 Pt. crucible, 4d, 1400°C, 4 grinding stages with ball-milling and pelletization of reagents	(15,388) Liebenbergite Ni ₂ SiO ₄	N/A
			(35,610) Enstatite MgSiO ₃	
			(47,1049) Bunsenite NiO	
Mg ₂ SiO ₄	MgO SiO ₂	Pt. crucible, 4d, 1400°C, 4 grinding stages with ball-milling and pelletization of reagents	(34-189) Forsterite Mg ₂ SiO ₄	N/A
			(45-946) Periclase MgO	
			(46-1045) Quartz SiO ₂	
			(35,610) Enstatite MgSiO ₃	
NiMgSiO ₄	NiO MgO SiO ₂	Pt. crucible, 4d, 1400°C, 4 grinding stages with ball-milling and pelletization of reagents	(84-1405) NiMgSiO ₄ , Liebenbergite	N/A
			(35,610) Enstatite MgSiO ₃	
			(34-410) (MgNi)O	
			(39-1425) SiO ₂ , Cristobalite	
Fe ₂ SiO ₄	FeO SiO ₂	2d 1100°C in a sealed quartz tube	(34,178) Fayalite Fe ₂ SiO ₄	Fe ₂ SiO ₄

Table 27: Summary of reported non-hydrous synthetic materials

5.4.1. Ni/Mg Olivines

Method 1

Synthesis was performed by high temperature reaction of the constituent oxides in stoichiometric ratio. The constituents were ground together and heated in a box furnace in an alumina crucible (at a rate of 1.5°C per minute) to 1400°C for 24h, then cooled, ground again and re-heated to 1400°C for a further 24h. This “shake and bake” procedure was repeated for 4 heating cycles.

Method 2

Method 2 was as “method 1” except reactions were carried out in Pt crucibles; reagents were ground by ball-milling in an agate ball mill (c. 1hr per cycle) and the powdered reactants were pelletized (c. 1t) for each heating stage.

Results

Although “method 1” showed the formation of a Ni-olivine phase, it did not yield single-phase material, with significant quantities of metal oxide and enstatite-type (NiSiO_3) impurities identified by PXRD. The synthetic procedure was then modified to “method 2”, in an attempt to induce complete reaction. These modifications showed noticeable improvement to the synthesis of Ni-olivine, with notable reduction of impurity phases observed in the PXRD pattern, however, some persistent impurity still remained (see Fig. 83). Using this same method (2) both Mg_2SiO_4 (Forsterite) and NiMgSiO_4 (Ni/Mg-olivine) were produced to a similar quality. Although single-phase products were not achieved for any of the compositions it is possible to observe the expected crystal lattice alteration, as a systematic shift to higher angles of 2θ in the PXRD patterns with increasing Ni-substitution (see Fig. 84).

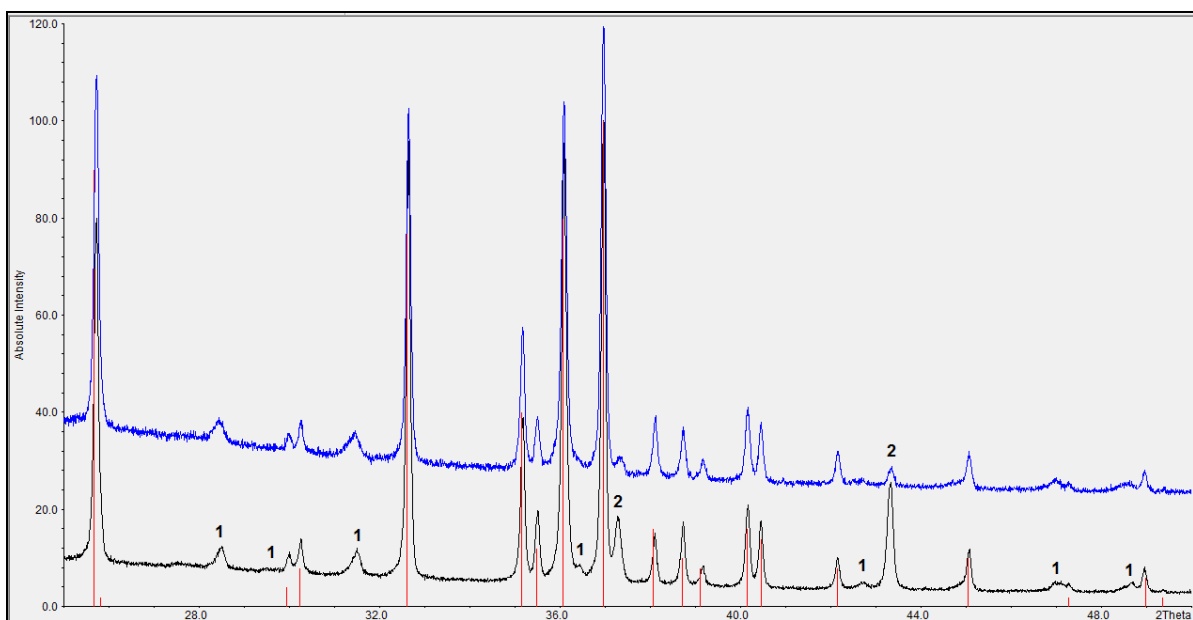


Figure 83: PXRD comparison of synthetic Ni-olivines (Ni_2SiO_4) from;

Reagents ground in pestle and mortar and reacted in alumina crucible (black);

Reagents ball-milled, pelletized and reacted in a Pt crucible (blue); ICDD data: Ni_2SiO_4 (red, Liebenbergite, card no. 15,388) Showing reduction in impurity phases: 1. NiSiO_3 (related to enstatite MgSiO_3 , ICDD card no. 35,610) and 2. Bunsenite NiO (from ICDD card no.47,1049)

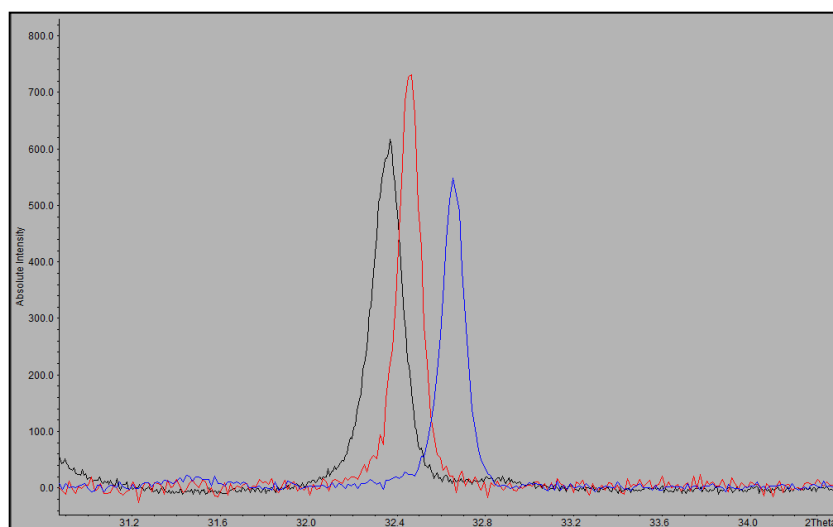


Figure 84: Expanded section showing right to left peak shift in synthetic Ni-Mg olivine;

Ni_2SiO_4 (blue); NiMgSiO_4 (red); Mg_2SiO_4 (black)

5.4.2. Fayalite (Fe_2SiO_4)

Method

Fayalite (Fe_2SiO_4) was prepared via a high temperature sealed quartz tube route. -10 mesh FeO (1.4369g, 0.02 mol., Sigma Aldrich UK, 400866) and -325 mesh SiO_2 (0.6008g, 0.01 mol., Sigma-Aldrich UK, 342890) were ground together using an agate pestle and mortar in an inert atmosphere (in a glove box) and sealed in a carbon coated silica tube under vacuum (to prevent the formation of Fe^{3+}). The sealed tube was then heated in a tube furnace (at a rate of 1°C min^{-1}) to 1100°C for 2 d and cooled at a rate of 1.5°C/min to room temperature. The sample was then analysed using PXRD and EPMA.

Results

The PXRD pattern (see Fig. 85) shows a good match to ICDD data for fayalite, confirming phase formation, although as the pattern was collected using Cu radiation the background is very high (caused by secondary fluorescence of the Fe) making identification of any potential impurity phases difficult.

Further characterisation of this sample using EPMA showed BSE-imaging with good homogeneity across the sample, with little variation (see Fig. 86). EPMA point analysis data of the 40 points gave 1 point which was discarded with a low total (70.28%); investigation of which suggests the analysis volume fell on a hole. Averages and standard deviation for the remaining 39 points are given in table 28. Formulae calculations from the averaged data (as described in the natural material EPMA section) based on 4 oxygen anions, gives a formula of Fe_2SiO_4 for the averaged data (with cation numbers accurate to 1d.p.), matching the fayalite formula expected. Indeed all points individually equate to this same formula, indicating good homogeneity through the sample, with no impurities identified, as suggested from both PXRD and BSE-imaging.

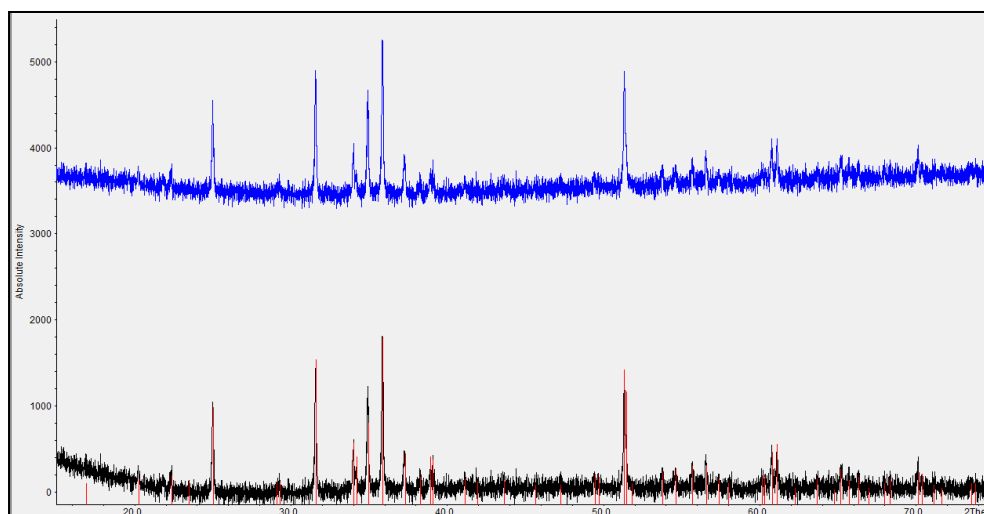


Figure 85: PXR D Pattern of the 2θ range 15-75° of synthetic fayalite FeSi₂O₄ (blue) and synthetic fayalite with background substituted (black); ICDD data for fayalite (red, card no. 34,178)

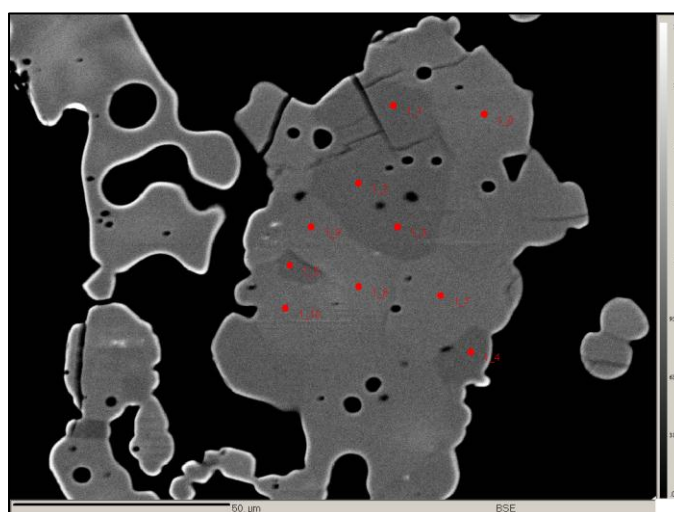


Figure 86: BSE image of point analysis area from synthetic fayalite (Fe₂SiO₄)

	FeO	SiO ₂	MgO	Al ₂ O ₃	CaO	Exp. Total	FeO+SiO ₂
Av.	70.98	29.07	0.01	0.06	0.01	100.13	100.06
Sd.	0.20	0.11	0.01	0.02	0.01	0.25	0.27

Table 28: Averaged EPMA point analysis data for synthetic Fe₂SiO₄

5.5. Synthetic Materials Conclusions

The initial low temperature and pressure hydrothermal syntheses studies showed that, synthesis of the mineral phases relevant to this project was possible and provided a basis for the hydrothermal synthesis studies. They also identified the ability to produce samples with greater structural order by modification of the synthetic route and the need for more extreme reaction conditions to achieve this for the relevant materials.

High temperature and pressure synthetic experiments built on the work achieved through the low temperature and pressure experiments, concentrating on synthesis of Ni-bearing talc and serpentine materials.

The high temperature and pressure hydrothermal synthesis study of the Ni-Mg talc series, has shown the successful formation of a complete solid solution between $\text{Ni}_3\text{Si}_4\text{O}_{10}(\text{OH})_2$ and $\text{Mg}_3\text{Si}_4\text{O}_{10}(\text{OH})_2$. The refined unit cell parameters match closely with reported unit cell parameters⁵⁴ and indicate there are no miscibility gaps. The similarities in the cation sizes of Ni^{2+} and Mg^{2+} produce only subtle changes in the lattice parameters between the end members and no systematic trends are observed. However, Ni-substitution does result in a more poorly crystalline talc structure, which, coupled with the disordered nature of the talc structure make reliable refinement of unit cell parameters using PXRD techniques difficult. TGA-DTA has shown the increased thermal stability of Ni-substituted talc, increasing by c. 60°C from the Mg to Ni end-member, despite the reduction in the crystallinity of the Ni-bearing phases. IR spectra for the synthetic samples match well with previously reported experimental and theoretical studies.^{68,80} Raman spectra also show the same OH-vibrational band characteristics.

High temperature and pressure synthesis of Ni-serpentine, by additional modification of the low temperature and pressure synthesis method, demonstrated the ability to further improve the structural order of the product using elevated temperature and pressure conditions, but also identified the instability of these materials at significant temperatures and pressures. The synthetic materials produced were however still too poorly crystalline to allow detailed characterisation using the methods available.

The synthetic study of olivine group minerals clearly identified problems inherent to the solid-state synthetic route, with stubborn impurities preventing in depth characterisation. However, the synthesised materials did clearly achieve demonstration of the expected effect of crystal lattice alteration as a systematic shift to higher angles of 2θ in the PXRD patterns with increasing Ni-substitution.

6. Synthetic vs. Natural Talc Materials

Subsequent to synthesising the series of standard Ni-Mg talc samples and analysing the IR data, it was realised that there may be potential for the use of IR as a method for analysing the Ni-content in the natural materials.

IR spectra were collected and analysed for several of the natural materials where talc had been identified by PXRD, with direct comparisons made to the spectra from the series of standard synthetic Ni-Mg talc samples. In addition to the use of the talc materials as standards, a standard serpentine material (“White lizardite” from the NHM, London) and a standard quartz material (laboratory grade SiO₂, granular quartz), were also used to identify the presence of these phases, where indicated.

Given that the specimens had already been clearly identified as complex mixtures, attempts were made to separate samples for analysis from the natural specimens on the basis of colour, where this was possible, in an attempt to simplify the spectra. In general this proved to be very difficult and acquiring spectra that identified any difference in the compositions was not possible with many samples. In addition to this, the disordered nature of the phases and the overlapping of significant vibrational bands (particularly in the OH-stretching region), due to the complex nature of the samples, made characterisation using this technique even more difficult.

However, a few notable observations were made. These are detailed here.

6.1. OR467

From specimen OR467, 2 separate samples were analysed using IR, dark green material and light green material (see Fig. 87). PXRD patterns of the specimen identified quartz, talc and serpentine in the sample. In comparison, EPMA analysis of the sample clearly identifies quartz and talc but no serpentine was found. The identified talc data was separated into 2 categories, high Ni-talc (>30% NiO) giving $(\text{Ni}_{0.67}\text{Mg}_{0.33})_3\text{Si}_4\text{O}_{10}(\text{OH})_2$ and low Ni-talc (<30% NiO) giving $(\text{Ni}_{0.45}\text{Mg}_{0.55})_3\text{Si}_4\text{O}_{10}(\text{OH})_2$.

IR Results

The IR spectrum from the sample of OR467 dark material shows a close match to a mixture of high and low nickel talc compositions (Fig. 88). This observation is concurrent with the findings in EPMA. Whilst the match in IR is shown to be closest to a mixture of 25% and 75% substituted Ni-talc, which does not match exactly to the formulae from the EPMA studies, this is still an interesting observation.

In contrast, the IR spectra from the OR467 light material shows very low Ni-talc OH-stretching contribution, more importantly it appears to show some shouldering to the left of the Mg-talc OH-stretching band concurrent with the presence of a serpentine OH-stretching band (Fig. 89). This is important as, whilst serpentine was identified in the PXRD pattern, EPMA results failed to identify a serpentine phase. This may indicate that the light green coloured zone was missed in EPMA analysis or that in this region it is too intimately mixed with the talc phase to be separated by EPMA.



Figure 87: Photograph of OR467 showing: “dark” and “light” zones analysed

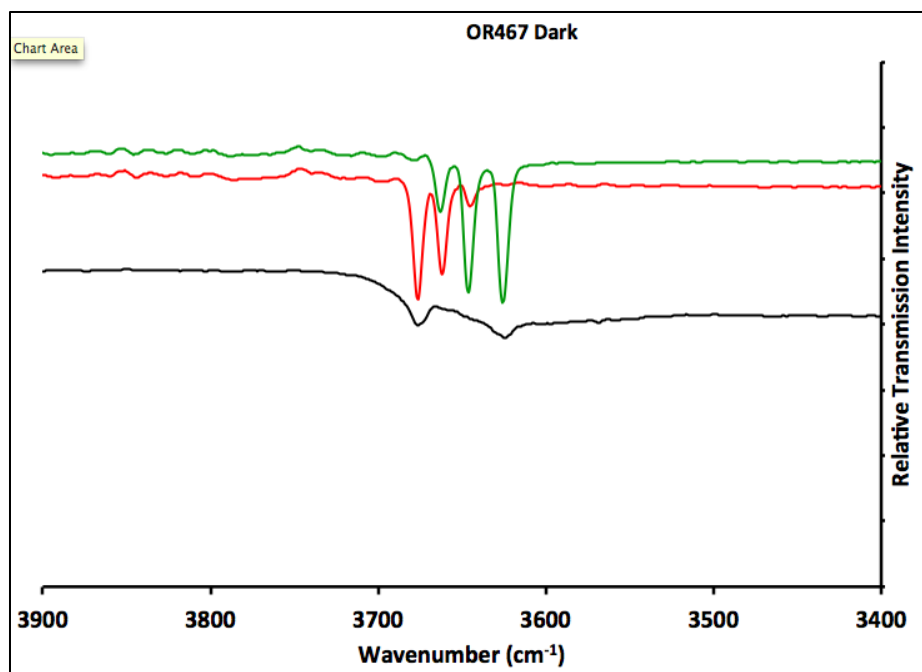


Figure 88: IR spectra of OR467 dark material (black) matched with:
Ni-talc ($\text{Ni}_{0.25}\text{Mg}_{0.75}\text{Si}_4\text{O}_{10}(\text{OH})_2$) (red) and Ni-talc ($\text{Ni}_{0.75}\text{Mg}_{0.25}\text{Si}_4\text{O}_{10}(\text{OH})_2$) (green)

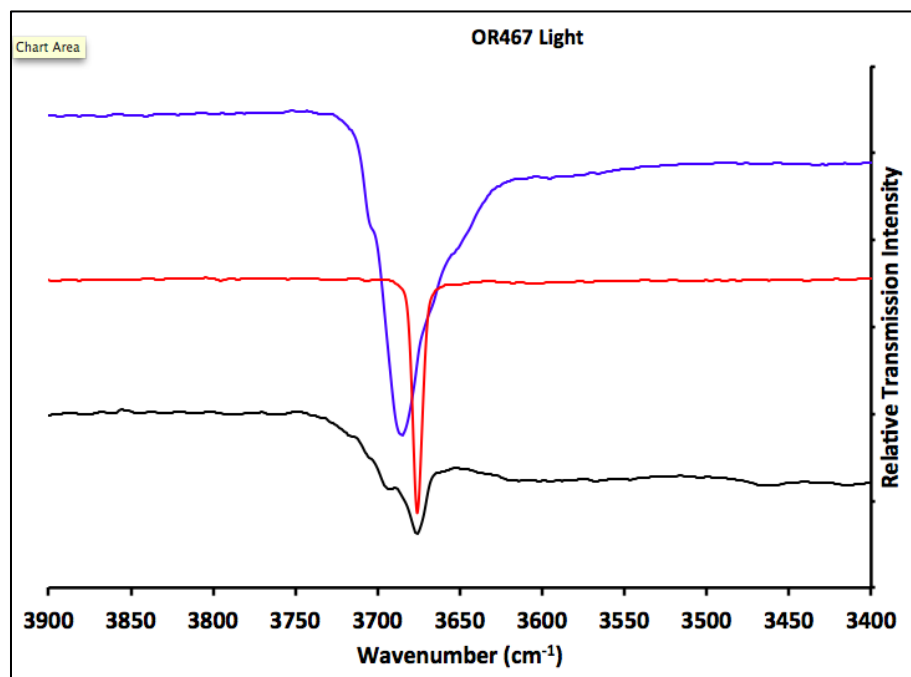


Figure 89: IR spectra of OR467 light material (black) matched with:
Mg-talc (red); Serpentine (blue)

6.2. CM053

From specimen CM053 2 separate samples were analysed using IR, dark green material and light green material (see Fig. 90). Similar to specimen OR467, PXRD patterns of green material from the specimen identified quartz, talc and serpentine EPMA analysis of the sample only identified presence of quartz and talc with no serpentine found.

As with specimen OR467, the identified talc data was separated into 2 categories: high Ni-talc (>33% NiO) $(\text{Mg}_{0.27}, \text{Fe}_{0.01}, \text{Ni}_{0.72})_3\text{Si}_4\text{O}_{10}(\text{OH})_2$ and low Ni-talc (<27% NiO) $(\text{Mg}_{0.69}, \text{Fe}_{0.01}, \text{Ni}_{0.30})_3\text{Si}_4\text{O}_{10}(\text{OH})_2$

IR Results

IR spectra for both samples from the specimen show that the material is a complex and disordered mixture, broad OH-stretching bands across the region prevent any clear compositional information to be determined (Fig. 91). However, contrary to the observations for specimen OR467 the dark material in this specimen appears to show a broad serpentine-type OH-stretching band protruding from the characteristic talc region. The talc OH-stretching regions for both samples are however very similar and both could, again, arguably indicate a mixture of low Ni and high Ni-talc phases present with bands observed at the Mg,Mg,Mg and Ni,Ni,Ni regions showing greater absorbance than the intermediate bands.



Figure 90: Photograph of CM053 showing: “green” zone analysed

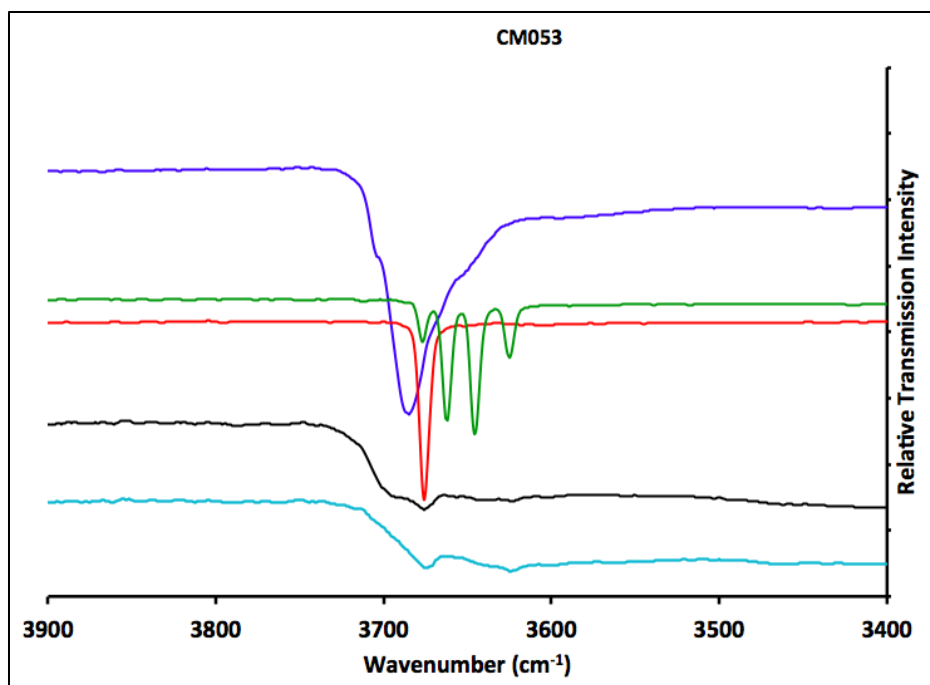


Figure 91: IR spectra of CM053 light material (light blue) and dark material (black) matched with: Mg-talc (red); Serpentine (blue);

Ni-talc ($\text{Ni}_{0.50}\text{Mg}_{0.50}\text{Si}_4\text{O}_{10}(\text{OH})_2$) (green)

6.3. Lipovka

From specimen Lipovka, 2 separate samples were analysed using IR, dark green material and light green material (see Fig. 92). PXRD and EPMA results from this sample both found the presence of quartz, talc and serpentine. Both talc and serpentine were observed in EPMA to have significant Ni content, with the talc close to 60% Ni-substitution.

IR Results

The IR spectra for the 2 separate samples from the specimen are shown to be clearly different. The spectrum for the light coloured material showed no presence of OH-stretching bands and on investigation found a direct match to the IR spectrum for quartz (Fig. 93). Conversely, the dark material shows broad OH-stretching bands around the Ni/Mg talc region, the shape of which is clearly similar to a Ni-talc with a composition

somewhere between $(\text{Ni}_{0.66}\text{Mg}_{0.33})_3\text{Si}_4\text{O}_{10}(\text{OH})_2$ and $(\text{Ni}_{0.50}\text{Mg}_{0.50})_3\text{Si}_4\text{O}_{10}(\text{OH})_2$ (Fig. 94). This matches very closely to the EPMA results. The broadening to the left of the talc OH-stretching region may also be linked to a serpentine phase, as observed in PXRD and EPMA.

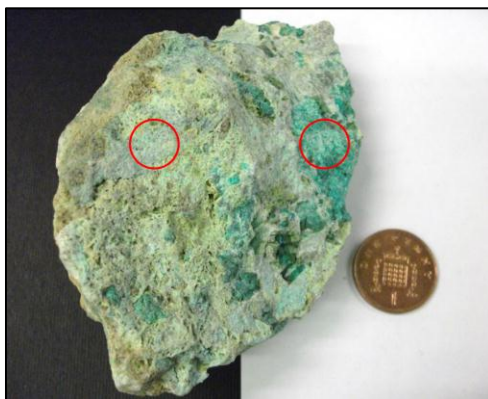


Figure 92: Photograph of Lipovka showing: “dark” and “light” zones analysed

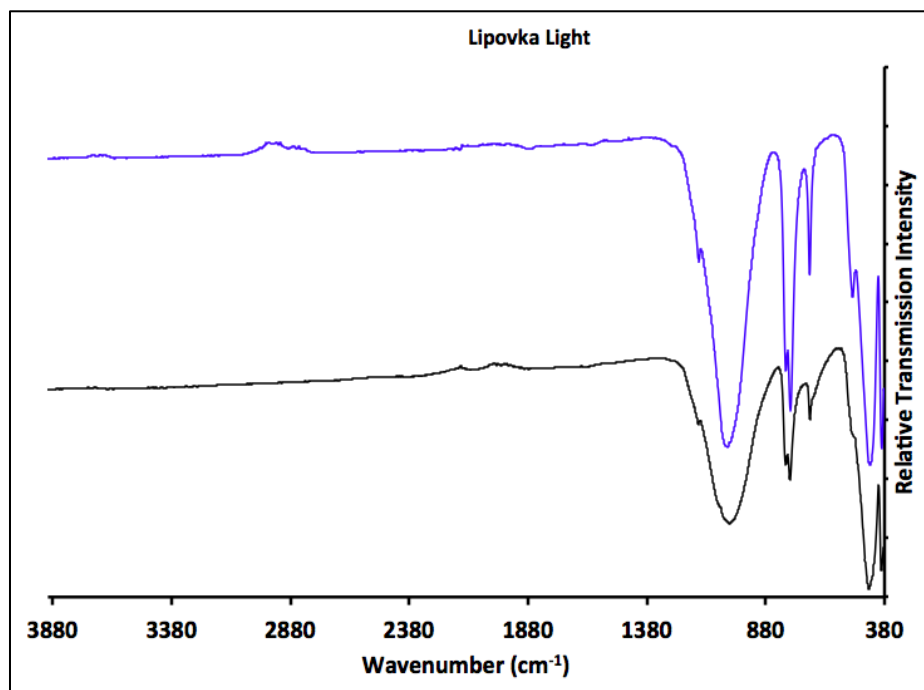


Figure 93: IR spectra of Lipovka light material (black) matched with quartz (blue)

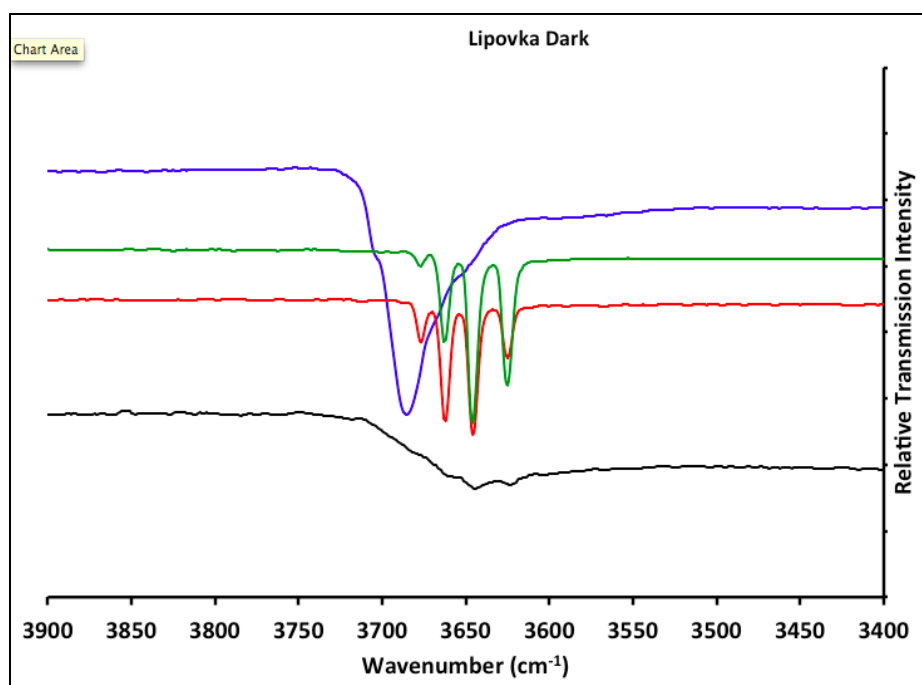


Figure 94: IR spectra of Lipovka light material (black) matched with:
Serpentine (blue); Ni-talc ($\text{Ni}_{0.50}\text{Mg}_{0.50}\text{Si}_4\text{O}_{10}(\text{OH})_2$) (red);
Ni-talc ($\text{Ni}_{0.66}\text{Mg}_{0.33}\text{Si}_4\text{O}_{10}(\text{OH})_2$) (green)

6.4. 09NIC060503A

From specimen 09NIC060503A, 3 separate samples were analysed using IR, a green phase, a dark brown phase and a light brown phase (Fig. 95). PXRD and EPMA studies of 09NIC060503A identified both talc and serpentine and formulae from EPMA found significant Ni-substitution on both phases. Talc was observed as $(\text{Mg}_{0.38}, \text{Fe}_{0.04}, \text{Ni}_{0.58})_3 \text{Si}_4\text{O}_{10}(\text{OH})_2$, whereas a serpentine was identified in two forms, as high Ni $(\text{Mg}_{0.47}, \text{Fe}_{0.03}, \text{Ni}_{0.50})_3 \text{Si}_4\text{O}_{10}(\text{OH})_2$ and low Ni $(\text{Mg}_{0.60}, \text{Fe}_{0.08}, \text{Ni}_{0.32})_3 \text{Si}_2\text{O}_5(\text{OH})_4$.

IR Results

IR spectra of the 3 separate samples from specimen 09NIC060503A are all very similar, despite their clear visible differences. As with all of the natural materials, the OH-

stretching region shows only limited detail, as bands are broad but serpentine contribution and a Ni-talc can both be matched to the region (Fig. 96). The closest match for a Ni-talc is found to be $(\text{Ni}_{0.50}\text{Mg}_{0.50})_3\text{Si}_4\text{O}_{10}(\text{OH})_2$ which is also supported by the EPMA data.

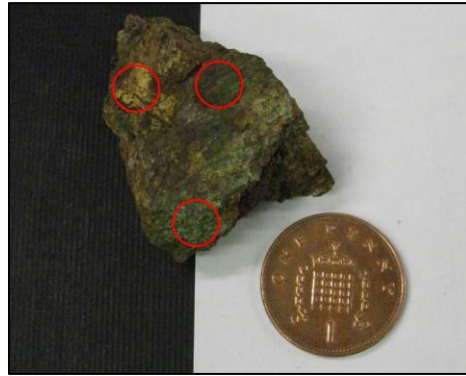


Figure 95: Photograph of 09NIC060503A showing:
“dark”; “light”; and “green” zones analysed

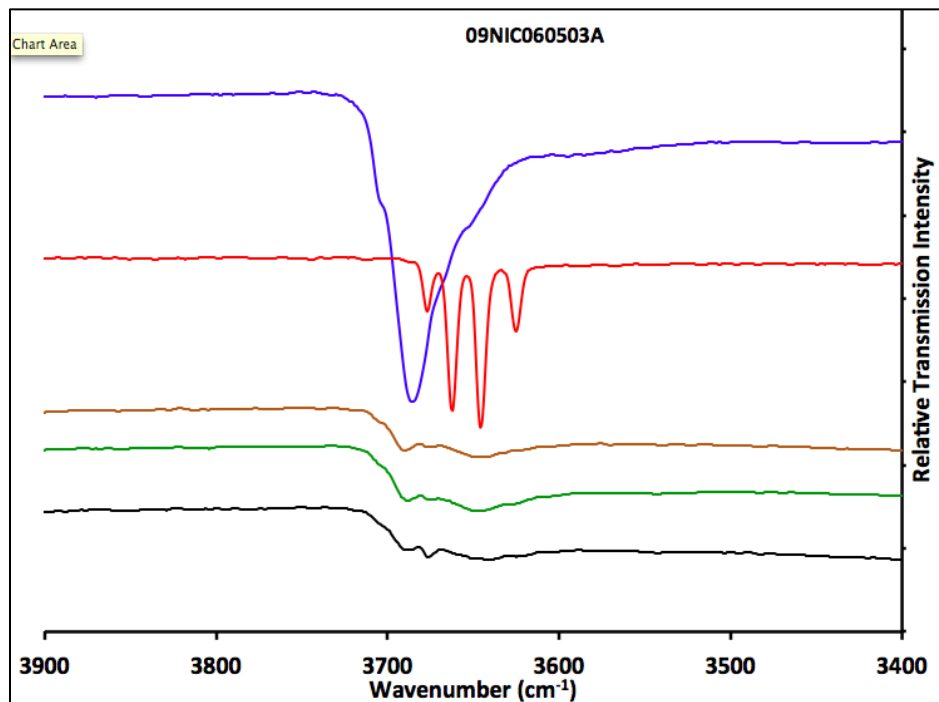
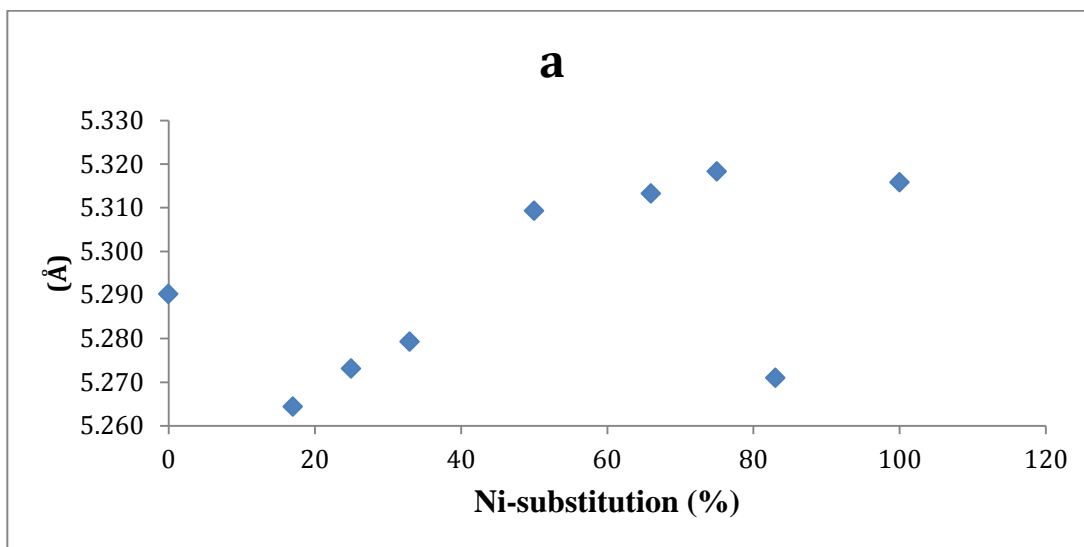


Figure 96: IR spectra of 09NIC060503A: dark (black), green (green), light (brown) matched with: Serpentine (blue); Ni-talc $(\text{Ni}_{0.50}\text{Mg}_{0.50})_3\text{Si}_4\text{O}_{10}(\text{OH})_2$ (red)

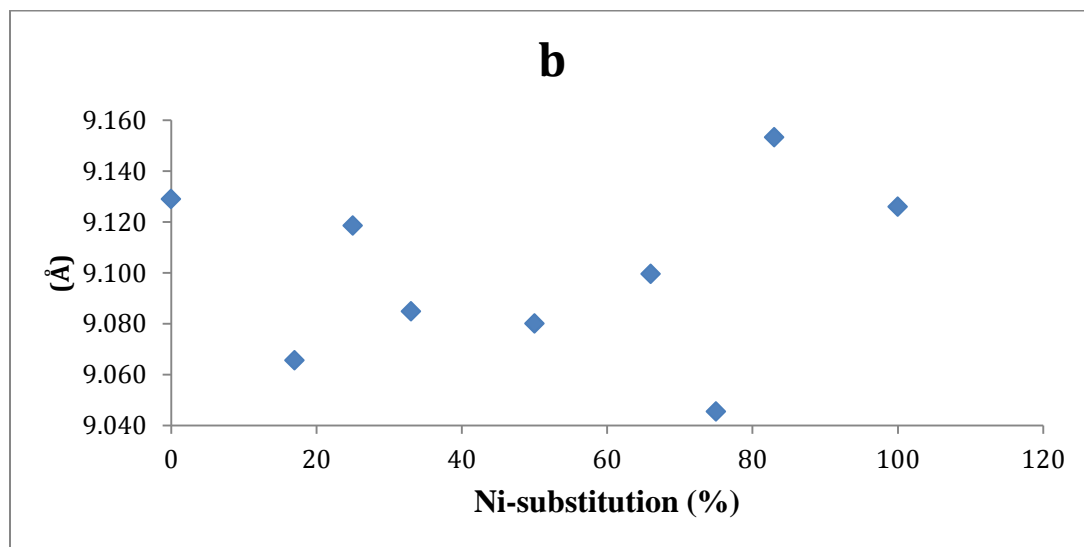
6.5. Conclusions

Whilst using IR as an analysis tool for determining Ni-content in the natural talc materials has been shown to be of limited value, this study has nonetheless identified how IR can be used as a significantly powerful complementary technique in the characterisation of these types of materials. IR is a simple and rapid technique that could potentially be used as a screening method for natural Ni-bearing specimens. However, significantly more work would be required to increase the usefulness of this method, analysis of other relevant synthetic phases and compositional series, such as Ni-Mg serpentines would greatly add to the understanding of the limitations of this approach.

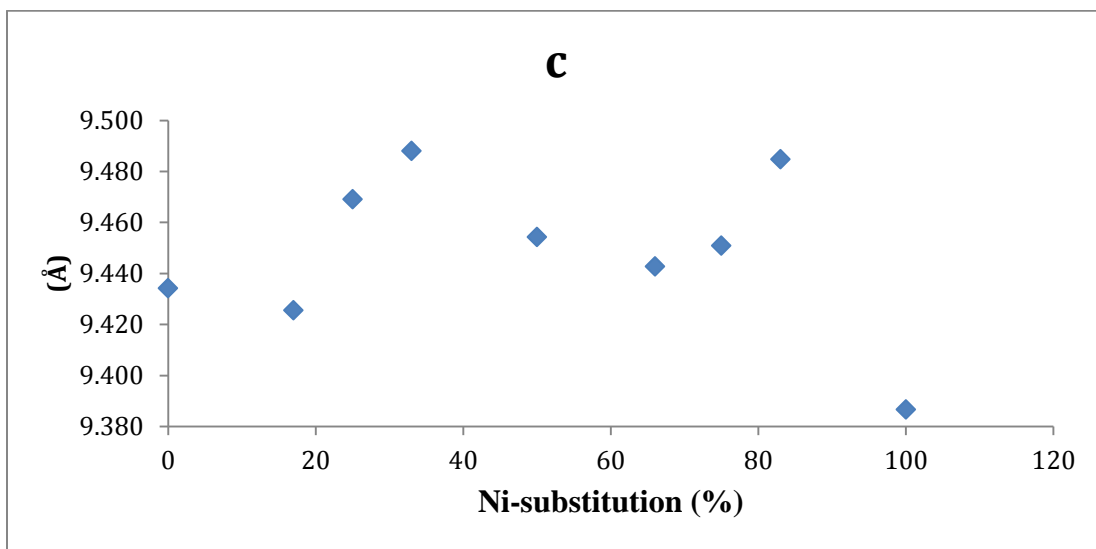
7. Appendices



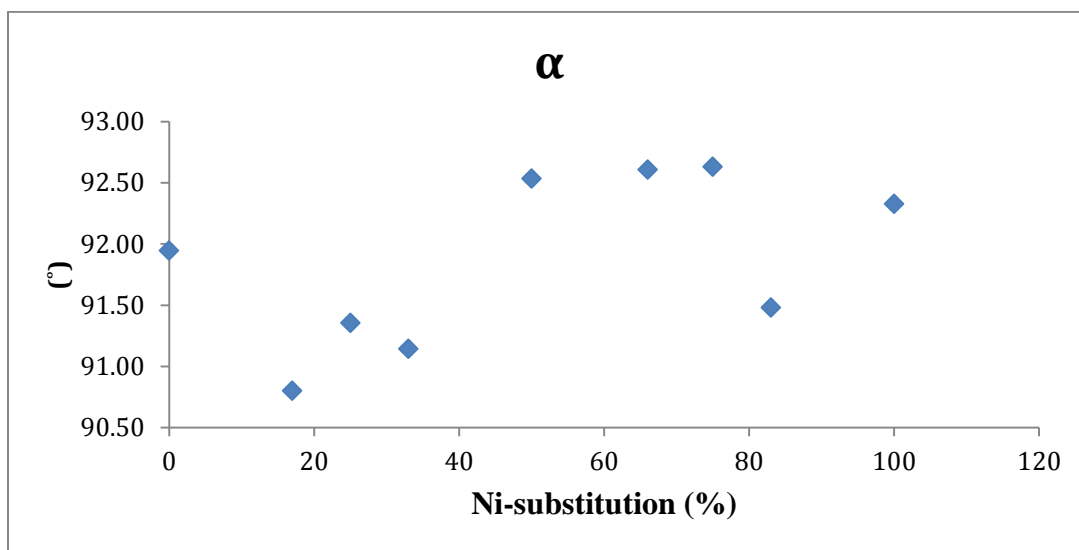
Appendix 1: Refined unit cell data for parameter (a) across the Ni/Mg-talc solid solution



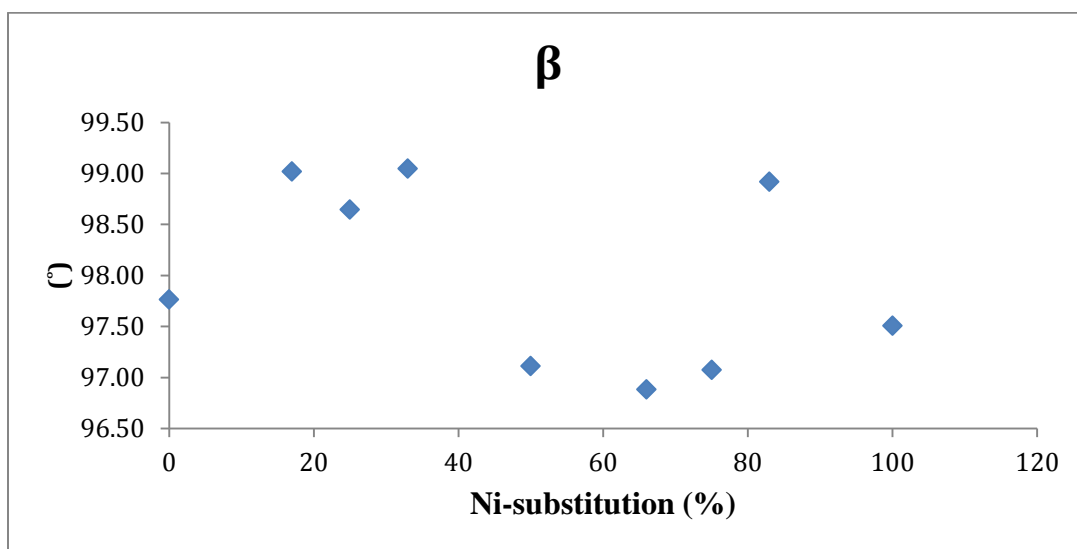
Appendix 2: Refined unit cell data for parameter (b) across the Ni/Mg-talc solid solution



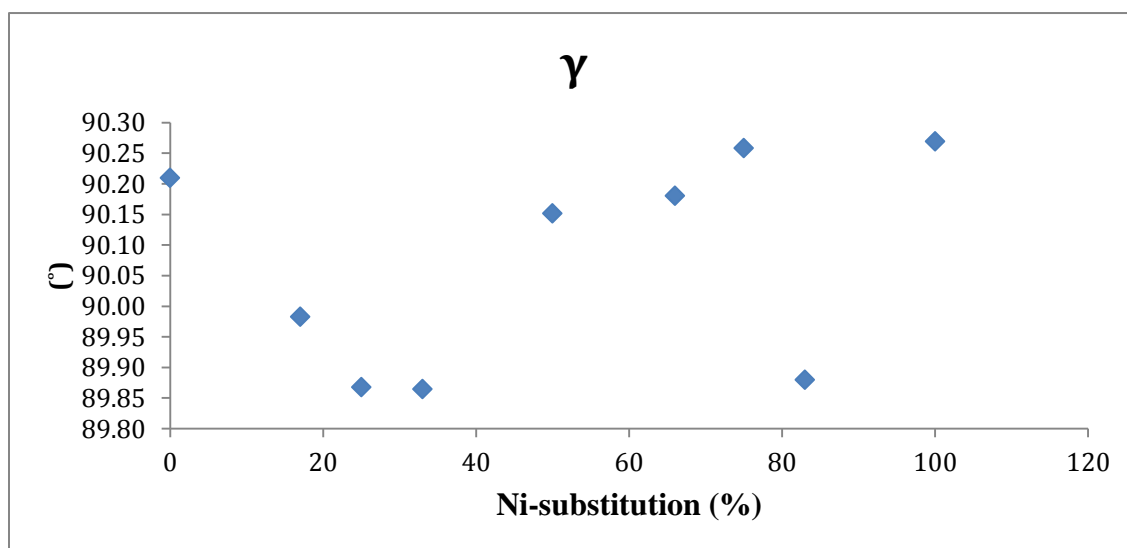
Appendix 3: Refined unit cell data for parameter (c) across the Ni/Mg-talc solid solution.



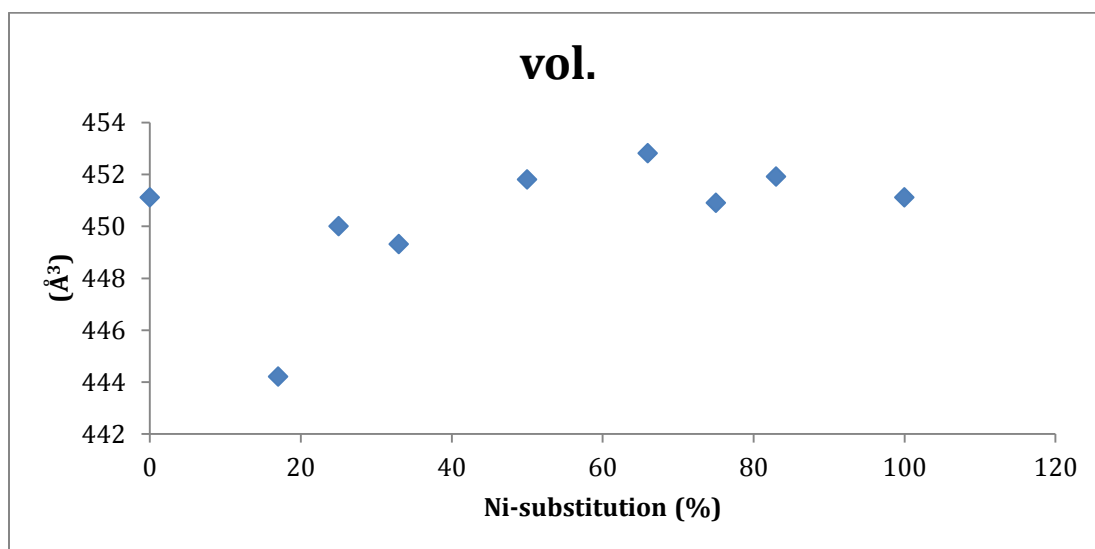
Appendix 4: Refined unit cell data for parameter (α) across the Ni/Mg-talc solid solution.



Appendix 5: Refined unit cell data for parameter (β) across the Ni/Mg-talc solid solution.



Appendix 6: Refined unit cell data for parameter (γ) across the Ni/Mg-talc solid solution.



Appendix 7: Refined unit cell data for cell volume (vol.) across the Ni/Mg-talc solid solution.

8. References

1. N. N. Greenwood and A. Earnshaw, Pergamon Press, 1st edn, (1984)
2. A. Dalvi, W. Bacon and C. Osborne, PDAC 2004 International Convention, Trade Show & Investors Exchange March 7-10, (2004)
3. <http://www.insg.org/whatnickel.aspx> (2010)
4. <http://minerals.usgs.gov/minerals/pubs/commodity/nickel/> (2009)
5. H. Dill, Earth Science Reviews, (2009) doi:10.1016/j.earscirev.2009.10.011
6. J. Beukes, E. Giesekke and W. Elliot, Minerals Engineering, 13, 14-15 (2000), 1573
7. N. Brand, C. Butt and M. Elias, J. Aus. Geol. & Geop. 17 (1998) , 4, 81
8. U.S. Geological Survey, Mineral Commodity Summaries, January (2009)
9. U.S. Geological Survey, 2007 Mineral Yearbook: Nickel, (2007)
10. R. Moskalyk and A. Alfantazi, Minerals Engineering, 15 (2002), 593
11. pg.3, http://Parkercentre.com.au/documents/flowsheet_14.pdf
12. D. Rubisov and V. Papangelakis, Hydrometallurgy, 58 (2000), 13
13. D. Georgiou and V. Papangelakis, Hydrometallurgy, 49 (1998), 23
14. J. Arroyo and D. Neudorf, US Patent 6,680,035, January 20, (2004)
15. R. McDonald and D. Whittington, Hydrometallurgy 91 (2008) 35
16. J. Fourestier, The Canadian Mineralogist, 40, (2002), 1721
17. H. Klein and F. Liebau, J. Solid State Chem., 181 (2008), 2412
18. "Silicates" Encyclopaedia Britannica. (2009) Encyclopaedia Britannica Online.
<http://www.britannica.com/EBchecked/topic/383675/mineral/80399/Silicates#toc=toc80399>
19. M. Wilson, A handbook of determinative methods in clay mineralogy, Blackie, (1987)
20. S. Nussik, Geol. Ser. 3 (1969) 108
21. S. Lakshman and B. Reddy, Proc. Ind. Acad. Sci. 6 (1973) 269
22. G. Faye, Canadian Mineralogist. 12 (1974) 389
23. T. Tejedor, T. Anderson and J. Herbillion, J. Solid State Chem., 50 (1983), 153
24. A. Manceau and G. Calas, Clay Minerals, (1987), 22, 357
25. G. Brindley, Am. Min., 60 (1975), 863
26. J. Bilbao, Rev. Soc. Esp. Min., 10 (2008) 142
27. B. Reddy, R. Frost, M. Dickfos, Spectrochimica Acta, Part A, 71 (2009) 1762
28. G. Faust, Am. Min. 51 (1966), 279
29. G. Faust, Am. Min. 51 (1966), 279

30. W. Pecora, S. Hobbs and K. Murata, *Econ. Geol.* 44 (1949). 13
31. G. Brindley and T. Hang, *Clays and Clay Min.*, 21 (1973), 51
32. W. Deer, R. Howie and J. Zussman, 3, (1962), 170
33. J. Banfield and S. Bailey, *Am. Min.*, 81 (1996), 79
34. W. Deer, R. Howie and J. Zussman, *An introduction to the rock forming minerals*, Longman, (1966)
35. A. Newman, *Chemistry of clays and clay minerals*, Min. Soc. London, (1987)
36. E. Whittaker and J. Zussman, *Min. Mag.* 31 (1956), 107
37. G. Popov and S. Zvyagin, *Ser. fiz.*, 23 (1959), 670
38. J. Rucklidge and J. Zussman, *Acta Cryst.*, 19 (1965) 381
39. M. Mellini, *Am. Min.*, 67 (1982) 587
40. K. Yada, *Acta Cryst.*, 27 (1971), 659
41. G. Kunze, *Zeitschrift fur Kristallographie*, 108 (1956), 82
42. J. Gard, *Min. Soc. London*, (1971)
43. T. Otten, *Am. Min.*, 78 (1993), 75
44. G. Faust, J. Fahey, B. Mason and E. Dwornik, *Science*, 165 (1969), 59
45. Glasser, *Bull. Soc. Franc. Min*, 30 (1907) 17
46. Z. Maksimovic, *Zapiski Vsesoyuznogo Min. Obshchestva*, 102 (1973), 143
47. P. Bayliss, *Min. Mag.*, 44, (1981), 153
48. E. Korytkova, L. Pivovarova, I. Drozdova and V. Gusarov, *Glass Phys. Chem.*, 31 (2005), 797
49. E. Korytkova, A. Maslov and L. Pivovarova, *Inorg. Mater.*, 41 (2005), 743
50. A. McDonald, B. Scott and G. Villemure, *Micro. and Meso. Mat.*, 120 (2009), 263
51. C. Milton, E. Dwornik and R. Finkelman, *Neues Jahrbuch fuer Min., Monatshefte* (1983), 513
52. R. Frost, B. Jagannadha Reddy, and M. Dickfos, *J. Raman Spectroscopy*, 39 (2008), 7, 909
53. J. Gruner, *Zeitschrift fur Kristallographie*, 88 (1934), 412
54. B. Perdikatsis and H. Burzlaff, *Zeitschrift fur Kristallographie*, 156 (1981), 177-186
55. A. Wilamowski and A. Wiewióra, *Acta Mineralogica-Petrographica*, Szeged, 445/2 (2004), 35-39
56. D. Roy and R. Roy, *Am. Min.*, 40 (1955), 147-178
57. S. De Waal, *Am. Min.*, 54 (1969) 31
58. E. Burke, *Can. Min.* 44 (2006) 1557

59. C. Schmidt, *Ann. der Physik (Poggendorff)*, 61, (1844), 388
60. G. Brindley and Z. Maksimovic, *Clay Minerals*, 10 (1974), 271
61. B. Ishida, *Min. J.*, 15 (1990), 93-104
62. M. Sivaiah, S. Petit, J. Barrault, C. Batiot-Dupeyrat and S. Valange, *Catalysis Today*, 157 (2010), 397–403
63. M. Sivaiah, S. Petit, M. Beaufort, D. Eyidi, J. Barrault, C. Batiot-Dupeyrat, S. Valange, *Microporous and Mesoporous Materials*, 140 (2011), 69-80
64. F. Martin, S. Petit, O. Grauby, M. Lavie, *Clay Minerals*, 34 (1999), 365-374
65. F. Perez and J. Burlitch, *Chem. Mater.*, 7 (1995), 2277-283
66. A. Rywak and J. Burlitch, *Physics and Chemistry of Minerals*, 23 (1996), 418-431
67. E. Ferrage, F. Martin, S. Petit, S. Pejo-Soucaille, P. Micoud, G. Fourty, J. Ferret, S. Salvi, P. DeParseval and J. Fortune, *Clay Minerals*, 38 (2003), 141–150
68. R. Wilkins and J. Ito, *Am. Min.*, 52 (1967), 1649-1661
69. R. Forbes, *Am. Min.*, 54 (1969), 1388-1408
70. J. Gruner, *Z. Kristallogr.*, 88 (1934), 412-419
71. C. Hendricks, *Z. Kristallogr.*, 99 (1938), 264-270
72. M. Akizuki and J. Zussman, *Min. Mag.*, 42 (1978), 107-110.
73. J. Rayner and G. Brown, *Clays and Clay Minerals*, 21 (1973), 103-114.
74. B. Zvyagin, K. Mishchenko and S. Soboleva, *Soviet Physics and Crystallography*, 13 (1969), 511-515
75. A. Viani, A. Gaultieri and G. Artioli, *Am. Min.*, 87 (2002), 966
76. T. Kogure, J. Kameda, T. Matsui and R. Miyawaki, *Am. Min.*, 91 (2006), 1363-1370
77. J. Perez-Rodriguez, L. Nadrid Sanchez del Villar and P. Sanchez-Soto, *Clay Minerals*, 23(1988), 399-410
78. V. Farmer and J. Russell, *Spectrochimica Acta*, 20 (1964), 1149-1173
79. V. Stubican and R. Roy, *Am. Min.*, 46 (1961), 32-51
80. E. Scholtzova, D. Tunega, L. Nagy, *J. Mol. Struct. (Theochem)*, 620 (2003), 1–8
81. M. Wesolowski, *Thermochimica Acta*, 78 (1984), 395-421
82. K. Bose and J. Ganguly, *Am. Min.*, 79 (1994), 692-699
83. P. Lee, P. Citrin, P. Eisenberger and B. Kincaid, *Rev. Mod. Phys.* 53 (1981), 769
84. A. Manceau and G. Calas, *Clay Minerals*, 21 (1986), 341
85. A. Decarreau, O. Grauby and S. Petit, *Applied Clay Science*, 7 (1992) 147
86. A. Manceau and G. Calas, 5th meeting of the European clay groups, Prague, (1983), 547
87. F. Muller, G. Besson, A. Manceau and V. Drits, *Phys. Chem. Minerals*, 24 (1997), 159

88. A. Manceau and G. Calas, *Am. Min.*, 70 (1985), 549
89. E. Nickel and H. Nichols. IMA/CNMNC list of mineral names. MINERAL database from <http://www.materialsdata.com>
90. G. Brindley et al., *Am. Min.*, 64 (1979), 615
91. S. Gleeson and R. Herrington, *Econ. Geol.*, 99 (2004), 1197
92. A. Gerard and J. Herbillion, *Clays and Clay Min.*, 31 (1983), 2, 143
93. S. Clark, *Min. Mag*, 36 (1990), 1145
94. S. Dann, *Reactions and Characterisation of Solids*, RSC Cambridge, (2000).
95. O. Tuttle, *Geological Society of America Bulletin*, 60 (1949), 1727
96. W. Luth and O. Tuttle, *Am. Min.*, 48 (1963), 1401
97. C. Williams, *Am. Min.*, 53 (1968), 1765-9.
98. D. Kerrick, *Research techniques for high pressure and high temperature*, G.C. Ulmer (ed.), New York, Springer, (1987), 179.
99. R. Dinnebier and S. Billinge, *Powder diffraction: Theory and practice*, (2008)
100. C. Hammond, *The basics of crystallography and diffraction*, 3rd ed, IUCr, Oxford Science Publications, (2009)
101. Diamond light source website, <http://www.diamond.ac.uk/Home/About/Synchrotrons/Machine.html>
102. B. Stuart, *Infrared Spectroscopy: fundamentals and applications*, (2004)
103. N. Colthup, L. Daly and S. Wiberley, *Introduction to infrared and Raman spectroscopy* 3rd edition, (1990)
104. T. Gilson and P. Hendra, *Laser Raman spectroscopy*, (1970)
105. M. Amer, *Raman spectroscopy*, (2009)
106. E. Charsley, S. Warrington, *Thermal analysis- techniques & applications*, Royal Society of Chemistry, (1992).
107. M. Brown, *Introduction to thermal analysis. Techniques and applications*, Chapman and Hall, London, (1988).
108. G. Höhne, W. Hemminger, H. Flammersheim, *Differential scanning calorimetry*, 2nd edition, Springer, London, (2003).
109. T. Mizutani, Y. Fukushima, A. Okada and O. Kamigaito, *Bull. Chem. Soc. Jpn.*, 63 (1990), 2094
110. R. Trujillano et al., *Micro. and Meso. Mat.*, 117 (2009) 309
111. K. Torii, Y. Onodera, T. Iwasaki, M. Shirai, M. Arai, Y. Nishiyama, *J. Porous Materials*, 4 (1997), 261

112. N. Bowen and O. Tuttle, *Bull. Geol. Soc. Am.*, 60(3), (1949), 439
113. A. Pawley, *Am. Min.*, 83 (1998) 51
114. M. Järvinen, M., *J. Appl. Cryst.*, 26 (1993), 525-531
115. C. Henderson, S. Redfern, R. Smith, K. Knight and J. Charnock, (2001): *Am. Min.*, 86 (2001), 1170–1187.
116. J. Pask and M. Warner, *J. Am. Ceram. Soc.*, 37 (1954), 118-127
117. F. Campbell, R. Roeder, *Am. Min.*, 53 (1968), 257-268 W. Vedder, *Am. Min.*, 49 (1964), 736-768
118. W. Vedder, *Am. Min.*, 49 (1964), 736-768